9-17-2019

Supercritical CO2 Foam Enhanced Oil Recovery: From Mechanistic Model Fit to Lab Experiments to Field-Scale Evaluation

Mohammad Izadi
mizadi3@lsu.edu

SUPERCRITICAL CO_2 FOAM ENHANCED OIL RECOVERY: FROM MECHANISTIC MODEL FIT TO LAB EXPERIMENTS TO FIELD-SCALE EVALUATION

A Dissertation

Submitted to the Graduate Faculty of the
Louisiana State University and
Agricultural and Mechanical College
in partial fulfillment of the
requirements for the degree of
Doctor of Philosophy

in

The Craft & Hawkins Department of Petroleum Engineering

by
Mohammad Izadi
B.S., Petroleum University of Technology, 2006
M.S., University of Louisiana at Lafayette, 2009
December 2019

ACKNOWLEDGMENTS

I am very grateful primarily to Craft and Hawkins Department of Petroleum Engineering at LSU and importantly to Mr. Donald W. Clayton for their financial support without which this research wouldn't have been possible.

I would like to express my appreciation to my advisor Dr. Seung Ihl Kam who has been very patient and encouraging throughout my PhD journey. His insight and expertise into this research, organizational skills and perseverance has always been inspiring to me. His relentless support always pushed me to pass over humps in challenging times. This dissertation is a result of numerous weekly discussions we had for which I would always look forward. Outside of research and classroom, he taught me wonderful life lessons.

I am also thankful to my committee members Dr. Mehdi Zeidouni, Dr. Clinton Willson, and Dr. Jianwei Wang for providing support and valuable suggestions. I would like to acknowledge Computer Modeling Group (CMG) for generous donation of CMG-STAS for this research. Many thanks to Halliburton Scholars Research Experience program, LSU Alumni Association, and Agencia Nacional de Hidrocarburos (ANH), Columbia for indirect support for this research. I would like to thank all faculty members, and my colleagues especially Doris Ortiz, Phuc H. Nguyen, and Hazem Fleifel for their valuable support during this study.

I am forever indebted to my parents who always believed in me, and their endless prayers backed my motivation to climb ladder of education. My deepest gratitude to the love of my life, Rana for her unconditional love and support throughout these years and her long-lasting patience in parenting our son, Aiden when I was not there to assist.

TABLE OF CONTENTS

LIST OF TABLES

LIST OF FIGURES

ABSTRACT

This study investigates how a mechanistic foam modeling approach based on bubble population balance is applied to a series of laboratory experimental data of a supercritical CO_2 foam in reservoir conditions to extract model parameters (topic 1). The model with model parameters determined from the fit is then used to estimate how far fine-textured strong foam can propagate into the reservoir, before turning into coarse-textured weak foam and before being segregated by gravity (topic 2). With the help of mechanistic model, a possible range of gas mobility for supercritical CO_2 foam is calculated and the resulting gas-phase mobility reduction factor (MRF) are applied to the field-scale EOR reservoir simulations (topic 3).

A mechanistic foam model that honors three different foam states and two steady-state strong-foam flow regimes is used to fit coreflood experimental data from Yin (2007). The results show why supercritical CO_2 foams are fundamentally different compared to other gaseous foams. The role of mobilization pressure gradient is shown to be the key to this difference – the pressure gradient required for supercritical CO_2 foam is much lower, and thus the attainment of strong foam in the reservoir is easier.

This study shows how far strong foams injected into the injection well can propagate at different injection foam qualities and velocities, which is one of the most important questions in actual field applications. Two main mechanisms that limit field foam propagation, such as “conversion from strong foam to weak foam” and “gravity segregation”, are examined. The results show that foam propagation distance increases with increasing injection pressure or rate and increases with decreasing foam quality

down to a certain threshold foam quality below which the distance is not sensitive to foam quality any longer.

CMG STARS simulations for a sector with an inverted 5-spot pattern are performed to evaluate how oil recovery changes at different injection foam qualities and velocities. The pre-determined values of gas mobility required for the simulation are guided by the mechanistic model. The use of sweep-efficiency contour plots is shown to be a convenient graphical method to determine the optimum injection foam quality that changes at different injection rates.

CHAPTER 1. OVERVIEW OF THIS STUDY

1.1. Introduction of CO_2 foam EOR

Enhanced oil recovery (EOR) is considered a vital option to increase ultimate hydrocarbon recovery from both conventional and unconventional reservoirs depleted by primary and secondary processes. EOR processes are classified into three major categories; thermal process, gas injection, and chemical process. Gas injection is the most widely used method, together with thermal process, and the gas phase is injected either as miscible or immiscible with reservoir fluids.

CO_2 injection, especially with supercritical CO_2, is very popular among various gas types (eg. N_2, hydrocarbon gas, flue gas, etc.) due to easier attainment of supercritical condition, better miscibility with reservoir fluids, higher density and viscosity, and higher societal need in conjunction with carbon capture and storage. CO_2 sequestration into the petroleum reservoirs is indeed considered one of the most efficient means for the disposal of a large quantity of CO_2, ultimately reducing greenhouse carbon emission. However, irrespective of gas types, gas injection inevitably encounters limitations such as fingering, channeling, and gravity segregation in the field.

Foaming the gas phase either in-situ or pre-generated prior to injection is a proven technology to improve sweep efficiency in the laboratory and field for more than 50 years. Foam is created by injecting gas with surfactant solutions. There are many successful field pilot tests reported in the literature including recent project such as CO_2 foam field test conducted in Salt Creek, WY (Mukherjee et al. 2016), and SAG treatment for conformance control in Lower Mirador formation, Cusiana Field, Columbia (Ocampo et al. 2013; Rossen et al. 2017).

Before applying foam injection in the field, several coreflood experiments are typically conducted to understand foam properties and flow characteristics. Then a modeling study is performed to obtain model parameters and to determine how much foam can reduce gas mobility. Modeling of foam rheology, especially in reservoir scale, is challenging because the model must replicate experimental data collected from small lab scale and must be able to predict how foam propagates in the large field scale. This study investigates multiple aspects of such supercritical CO_2 foams, from a fit of mechanistic foam model to laboratory coreflood data to field-scale evaluation of foam EOR applications.

1.2. Chapter description

The content of each chapter is summarized as follows: chapter 1 gives a brief introduction of the problem solved in this study. Chapter 2 provides detailed descriptions about the mechanistic foam modeling approach used in this study. This chapter shows (i) how to use the model to make a fit to coreflood data extracted from the literature, and then (ii) what makes supercritical CO_2 foams special compared to other gaseous foams by investigating the effect of mobilization pressure gradient. Chapter 3 shows how to use the mechanistic model to estimate foam propagation distance in large-scale applications. This chapter deals with two major events that limit foam propagation - “conversion from strong foam to weak foam (csw)” and “gravity segregation (gs)”. Chapter 4 presents an example of field-scale supercritical CO_2 foam EOR (Lisama field, Colombia) by using CMG STARS simulator. The selection of required gas-phase mobility reduction factors

(MRF) is guided by the mechanistic model. This chapter provides details about how to optimize the injection strategies (injection rate, injection foam quality) in the field. Chapter 5 concludes this study with recommendations.

CHAPTER 2. BUBBLE POPULATION BALANCE MODELING FOR SUPERCRITICAL CO_2 FOAM EOR PROCESSES: FROM PORE-SCALE TO CORE-SCALE AND FIELD-SCALE EVENTS

2.1. Introduction

Although less severe due to higher density and viscosity, dense or supercritical CO_2 EOR processes encounter essentially the same fates such as fingering, gravity segregation, and channeling, just like any other gas injection methods. Foaming the injected CO_2 by using surface-active agents (or, surfactants), the first attempt dated back to Bond and Holbrook (1958), has long been a promising candidate in the field to delay the breakthrough of injected gas and hence improve the overall sweep efficiency. Lee and Kam (2013) reviews several successful foam field projects, cited often in the literature.

Foams in porous media can be created and destroyed in-situ as foam films (or lamellae) travel along the complicated pore structures. The number of liquid films in unit pore volume, referred to as foam texture (n_f), is an outcome of dynamic mechanisms of in-situ lamellae creation and coalescence, which is a key parameter to understand non-Newtonian foam rheology through the changes in gas relative permeability, gas viscosity, trapped gas saturation, and so on.

Three main mechanisms identified for in-situ lamellae creation are leave-behind, snap-off, and lamellae mobilization and division, while there is a major lamella-coalescence mechanism identified, that is, a sudden rupture of foam films above limiting capillary pressure P_c^* (or, below limiting water saturation, S_w^*, equivalently), as fully described by earlier studies (Ransohoff and Radke, 1988; Khatib et al., 1988; Rossen, 1996; Hirasaki et al., 1997).

Once present, foam exhibits a hysteretic behavior represented by three different states as shown in Figure 2.1(a) from Gauglitz et al. (2002) such as weak-foam state, strong-foam state, and intermediate state in between. The coarse-textured foam showing a relatively moderate decrease in gas mobility (or, the lower surface at lower ∇P) is called weak foam, while the fine-textured foam showing a drastic decrease in gas mobility (the upper surface at higher ∇P) is called strong foam. Once the strong-foam state is obtained, foam rheology can be represented by two distinct rheological behaviors in a contour plot of the steady-state pressure gradient as a function of gas (y axis) and liquid (x axis) velocities, as first shown by Osterloh and Jante (1992). Alvarez et al. (2001) confirmed the same behavior in a wide range of experimental conditions putting them into the high-quality and low-quality regimes. The two flow regimes are separated by a threshold foam quality (f_g^*). For example, the f_g^* is shown to be 0.73 in Figure 2.1(b).

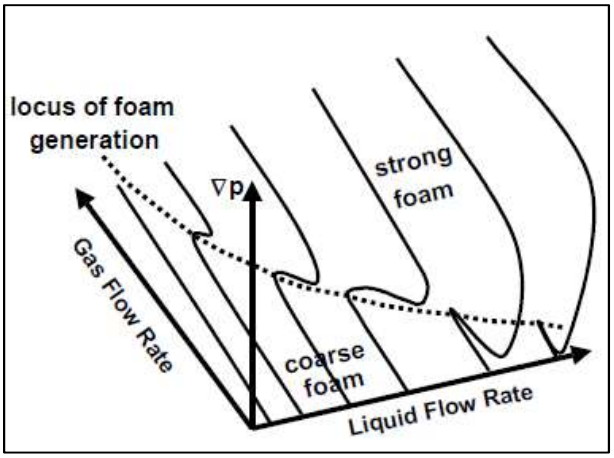

(a)

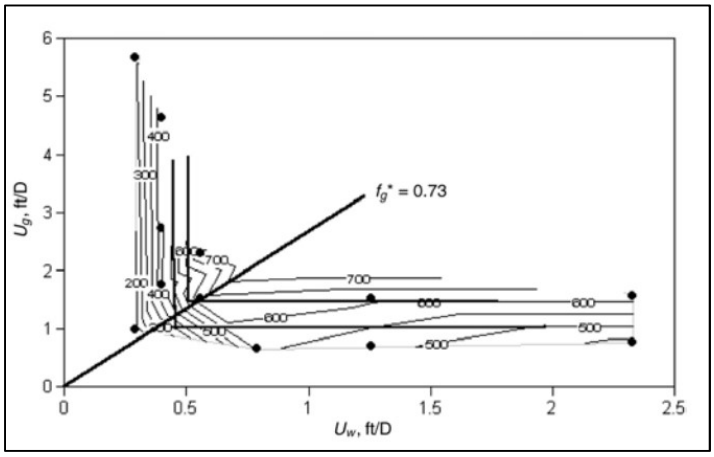

(b)

Figure 2.1. Key features of core-scale events to be honored in this study: (a) three different foam states (weak-foam (or coarse-foam) state, strong-foam state, and intermediate state (between weak-foam and strong-foam states curving back); Gauglitz et al., 2002) and (b) two steady-state strong-foam flow regimes (Alvarez et al., 2001).

There are largely two types of foam modeling techniques available in the literature, namely, local steady-state (or, local equilibrium) modeling and bubble population balance modeling. The population balance model, to be applied in this study, is designed to capture foam texture and its relationship with other properties such as effective gas

viscosity, relative permeability, and trapped gas saturation and so on to capture non-Newtonian foam rheology. This technique is more complicated than the local steady-state modeling that uses a pre-specified mobility reduction factor (MRF) but produces more physically sound results based on robust mathematical framework. Different versions of population-balance models exist in the literature depending upon how to handle foam flow in porous media mathematically (Friedmann et al., 1991; Kovscek and Radke, 1994; Kovscek et al., 1995; Myers and Radke, 2000; Kam and Rossen, 2003; Kam, 2008; Farajzadeh et al., 2015). Recent modeling studies introduce a new type of foam simulation technique, so-called implicit-texture foam model (Farajzadeh et al, 2015; Lotfollahi et al., 2016). Although it does not calculate bubble population by solving population-balance partial differential equations per se, this technique employs model parameters to capture foam fundamentals near limiting capillary pressure and water-/oil-sensitive foam stability, and thus improves simulation capability significantly in large field-scale events adding computational efficiency.

2.2. Motivations and Objectives

An earlier study from Gauglitz et al. (2002), showing foam generation experiments with N_2 foams and supercritical CO_2 foams, presented interesting results as shown by Figure 2.2 (a). That is, the critical pressure gradient (or, the mobilization pressure gradient,∇P_o) for supercritical CO_2 foams is a couple of orders of magnitude lower than that for N_2 foams, decreasing with increasing permeability (k). Because of $\nabla P_o = 4\ (\sigma/R_t)$, smaller ∇P_o is caused by lower interfacial tension (σ) at given pore throat sizes (R_t)). Figure 2.2 (b) shows another example from Aarra et al. (2014), that is, gaseous CO_2

foams (backpressure 30 bar) exhibit higher steady-state pressure drop (ΔP) than supercritical CO_2 foams (backpressures 120 and 280 bar). This is, again, because of a reduction in σ and, therefore, a reduction in ∇P_o. (Note that the pressure drop (ΔP) is measured in individual coreflood experiments, while the mobilization pressure gradient (∇P_o) is a parameter dependent upon rock and fluid properties.)

Reaching a strong-foam state at lower pressure gradient due to lower ∇P_o means easier formation of piston-like displacement, which results in higher oil recovery and more efficient sweep in the field conditions, as demonstrated by Lee and Kam (2014) by using three-phase Method of Characteristics solutions. For example, when the absolute permeability is about 1 μm^2 for Boise sandstone in Figure 2.2, supercritical CO_2 foam forms strong foams at $1x10^4$ Pa/m (or, 0.442 psi/ft), but N_2 foam still does not form strong foams until $1x10^6$ Pa/m (or, 44.2 psi/ft), clearly showing the benefit of supercritical CO_2 foams conceptually.

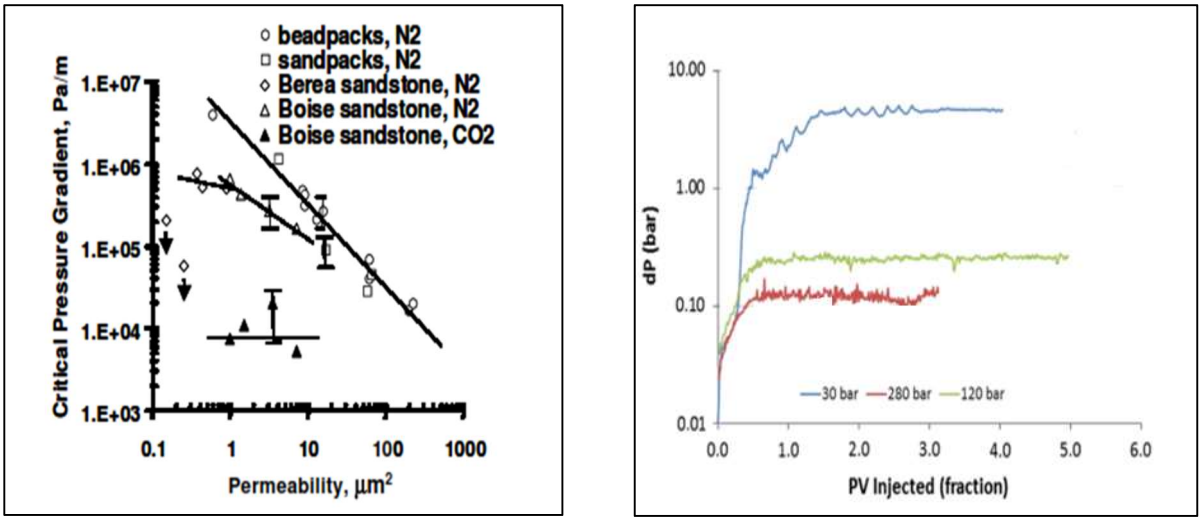

(a) (b)

Figure 2.2. Experimental data showing the difference between supercritical CO_2 foams and other gaseous foams: (a) mobilization pressure gradient required for foam generation for supercritical CO_2 foams and N_2 foams (Gauglitz et al., 2002) and (b) pressure-drop comparison for supercritical CO_2 foams and gaseous CO_2 foams in Berea sandstone (Aarra et al., 2014).

The objective of this study is to investigate (i) how to fit a population-balance foam model (based on pore-scale events) to supercritical CO_2 foam experimental data (core-scale events) and extract model parameters, and (ii) apply the modeling technique to field-scale events to understand the fundamental mechanisms of CO_2 foams propagation into the reservoir. This study must be distinguished from previous studies of Kam and Rossen (2003), Kam (2008), Afsharpoor et al. (2010) and Lee et al. (2016) - the previous studies deal with gaseous foams (eg., N_2 foams) showing three distinct foam states (i.e., foam rheology surface curving back and forth (Figure 2.1(a)), while this study, for the first time, deals with supercritical CO_2 foams (at extremely low ∇P_o) showing a smooth change from weak-foam to strong-foam state (without intermediate state), revealed as one of the major conclusions. Such a characteristic of supercritical CO_2 foams, compared to

gaseous foams, is endowed by much lower (more than a couple of orders of magnitude difference) interfacial tension between emulsion-like supercritical CO_2 and surfactant solutions. Throughout this study, the focus is made to show why supercritical CO_2 foam should be looked at differently, and how much difference it causes when the propagation in the field-scale event is taken into consideration. In this study, it is believed that CO_2 in its supercritical condition to form foams is fundamentally different from other gaseous foams (i.e., gaseous hydrocarbon foams, flue-gas foams, nitrogen foams, carbon-dioxide foam, etc.). It is because it behaves more like emulsions with much higher density and much lower interfacial tension. In field applications, supercritical CO_2 exhibits more complicated phase interactions with reservoir fluids (solubility, swelling effect, acidity and resulting chemistry). The effect of oil is not included in this study yet. It is because the primary goal of this study is to examine foam propagation distance based on unique properties of supercritical state of CO_2 once the steady state is obtained, rather than dynamic interactions between foams and reservoir fluids during the transient state. The finding of this study can be combined with dynamics foam simulations (Kam, 2008) and the interaction with foams and reservoir oils as a next step (Ashoori et al., 2010; Conn et al., 2014), however. The heart of this study touches the issue of how to upscale lab-scale data to field-scale applications during which the nature of flow typically changes from linear to radial or spherical, which has long been questioned in this research area (Kovscek et al., 1997; Li et al., 2006). The field-scale foam propagation shown in this study covers the issue by using pressure-gradient-dependent (and thus velocity-dependent) foam flow characteristics.

2.3. Methodology

Population balance modeling used in this study is considered a mechanistic model, because the model keeps track of a wide range of foam mechanisms independently and puts them together. Falls et al. (1988) and Patzek (1988) are the examples of early days of mechanistic foam modeling effort. They are followed by numerous studies afterwards such as Friedmann et al. (1991), Kovscek and Radke (1994) and Kam and Rossen (2003), among many.

The mechanistic foam model in this study defines lamellae creation function as shown below, by incorporating the concept of mobilization pressure gradient (∇P_o) (Rossen and Gauglitz, 1990) into the equation (Kam, 2008; Afsharpoor et al., 2010):

$$R_g = \frac{C_g}{2}\left\{\mathrm{erf}\left(\frac{\nabla P - \nabla P_o}{\sqrt{2}}\right) - \mathrm{erf}\left(\frac{-\nabla P_o}{\sqrt{2}}\right)\right\} \qquad (2.1)$$

In Equation 2.1, R_g is the rate of lamella creation (i.e., change in bubble population within unit space over time), C_g is the model parameter, ∇P is the pressure gradient, and erf is the error function. Note that ∇P_o is the pressure gradient to mobilize existing foam films to create a population of bubbles subsequently in the downstream of porous media (Kam and Rossen, 2003). The two parameters (C_g and ∇P_o) handle foamability of surfactant solutions (including formulation and concentration) with a specific type of gas (e.g., N_2, CO_2, supercritical CO_2) in a pore network with a certain pore size distribution and wettability. As shown in Figure 2.3, at given ∇P_o, the rate R_g remains low if local ∇P is

lower than ∇P_o. R_g increases rapidly as ∇P approaches ∇P_o, and finally levels off if ∇P becomes higher than ∇P_o.

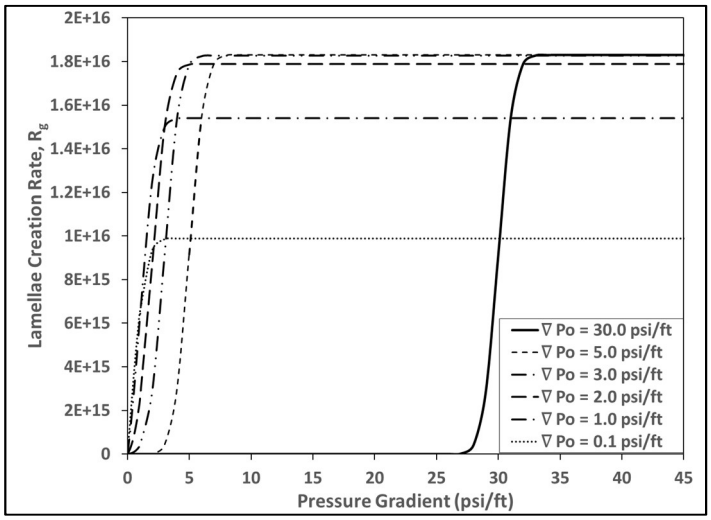

Figure 2.3. The rate of in-situ lamellae creation as a function of pressure gradient at various mobilization pressure gradient (∇P_o) values.

Gauglitz et al. (2002) derived an explicit relationship between ∇P_o and the absolute permeability (k) of bead-packs. They combined the Ransohoff and Radke (1988) capillary number and Darcy law, and then utilized it with the Blake-Kozeny correlation for permeability to solve for the mobilization pressure gradient as

$$\nabla P_o = \frac{8 f_{nw} \sigma}{L} \sqrt{\frac{4\emptyset^3}{150k(1-\emptyset)^2}} \qquad (2.2)$$

where, f_{nw} is the fractional flow of gas (non-wetting phase), σ is gas-liquid interfacial tension, L is the length of individual pore, and $\emptyset$ and k are the porosity and permeability of the sample. Because $L \sim R_t \sim k^{-1/2}$, ∇P_o scales like $\sim k^{-1}$ which is consistent with Figure

2.2 (a) for N_2 foams in unconsolidated porous media (bead-packs and sand-packs in Figure 2.2 (a), for example). In addition, because of lower σ, supercritical CO_2 foam shows lower ∇P_o, compared to the gaseous foams (e.g., N_2 or CO_2 foams).

On the other hand, the lamellae coalescence function is given by

$$R_c = C_c n_f \left(\frac{S_w}{S_w - S_w^*}\right)^n \tag{2.3}$$

where, R_c is the rate of lamella coalescence(i.e., change in bubble population within unit space over time), C_c is the model parameter, n is the coalescence rate exponent, and n_f, S_w and S_w^* represent foam texture, aqueous phase (water) saturation, and limiting water saturation, respectively. The rate R_c stays low when S_w is relatively high and increases rapidly as S_w approaches S_w^*. In the steady-state mechanistic foam modeling, the rate of lamella creation and the rate of lamella coalescence are balanced. Therefore, the steady-state foam texture (n_f), that is, the number of lamellae (or bubble population) within unit space, can be explicitly calculated as follows, by making Equations 2.1 and 2.3 equal:

$$n_f = \frac{C_g}{2C_c}\left(\frac{S_w - S_w^*}{S_w}\right)^n \left\{\mathrm{erf}\left(\frac{\nabla P - \nabla P_o}{\sqrt{2}}\right) - \mathrm{erf}\left(\frac{-\nabla P_o}{\sqrt{2}}\right)\right\} \tag{2.4}$$

Note that for any situations with $S_w < S_w^*$, there is no foam ($n_f = 0$). If calculated n_f is greater than $n_{f\,max}$, it is set to be $n_{f\,max}$ which is a typical behavior of strong foams in the

low-quality regime because diffusion within a pore does not allow bubbles to be smaller than the pore size (Alvarez et al., 2001). Therefore, $n_{f\,max}$ corresponds to the minimum bubble size, that is, roughly the average pore size.

The transport of foam in porous media is expressed by Darcy's equation as follows:

$$u_w = \frac{k k_{rw}(S_w)\nabla P}{\mu_w} \tag{2.5}$$

and

$$u_g = \frac{k k_{rg}^{o}(S_w)\nabla P}{\mu_g^{o}} \quad \text{or} \quad u_g = \frac{k k_{rg}^{f}(S_w)\nabla P}{\mu_g^{f}} \tag{2.6}$$

for water and gas (superscripts "o" and "f" represent states without and with foams), respectively. Foam consists of a dispersed internal gas phase and a continuous external liquid phase stabilized by surfactants. The gas phase then divides into two parts: trapped gas and flowing gas. Because the trapped gas is stationary due to capillary pressure, Darcy's equation for the gas phase is modified with a reduction in gas relative permeability (through the fraction of trapped gas saturation) (Kovscek, 1994). On the contrary, there is no change in Darcy's equation for the liquid phase because it forms the external phase as suggested by experimental studies (Bernard et al. 1965; Holm, 1968; and Friedmann and Jensen, 1986).

The liquid relative permeability is given by

$$k_{rw}(S_w) = A\left(\frac{S_w - S_{wc}}{1 - S_{wc} - S_{gr}}\right)^{m_1} \tag{2.7}$$

where, A and m_1 are the parameters for Corey-type liquid relative permeability, S_{wc} is the connate water saturation, and S_{gr} is the residual gas saturation. The gas relative permeability is given by

$$k_{rg}^{o}(S_w) = B\left(\frac{1 - S_w - S_{gr}}{1 - S_{wc} - S_{gr}}\right)^{m_2} \tag{2.8}$$

in the absence of foams and

$$k_{rg}^{f}(S_w) = B\left(X_f \frac{1 - S_w - S_{gr}}{1 - S_{wc} - S_{gr}}\right)^{m_2} \tag{2.9}$$

in the presence of foams, where B and m_2 are the parameters for Corey-type gas relative permeability, and X_f is the fraction of flowing gas phase. Of course, the sum of flowing gas fraction and trapped gas saturation is one ($X_f + X_t = 1$). The trapped gas fraction is calculated by

$$X_t = X_{t\,max}\left(\frac{\beta n_f}{1 + \beta n_f}\right) \tag{2.10}$$

following Kovscek and Radke (1994). Note that $X_{t\,max}$ is the maximum trapped gas fraction that can be estimated using tracer tests, commonly ranging 0.5 – 0.9 (Kovscek and Radke, 1994; Kovscek et al., 1995; Chen at al., 2010; Lotfollahi et al., 2016), and β is a model parameter relating gas trapping to foam texture.

Following Hirasaki and Lawson (1985), gas viscosity in the presence of foam is

$$\mu_g^f = \mu_g^o + \frac{C_f n_f}{\left(\frac{u_g}{\emptyset S_g X_f}\right)^{\frac{1}{3}}} \tag{2.11}$$

where, μ_g^o is gas viscosity in the absence of foam, S_g is gas saturation, C_f is the model parameter, $\emptyset$ is the porosity of the medium, and X_f is the fraction of flowing gas phase. Once strong-foam state is achieved, the upper surface of foam-rheology surface (i.e., Figure 2.1(a)) can be reasonably captured by the power-law model, for example,

$$\nabla P = u_g^{\sigma_L} \tag{2.12}$$

and

$$\nabla P = u_w^{\sigma_H} \tag{2.13}$$

for the low-quality regime and high-quality regime, respectively. The exponents (σ_L and σ_H) are one if Newtonian, greater than one if shear-thickening, and less than one if shear-thinning.

The ability for foams to reduce gas mobility is expressed by mobility reduction factor (MRF) which is defined by

$$\mathrm{MRF} = \frac{k_{rg}^{o}\mu_g^{f}}{k_{rg}^{f}\mu_g^{o}} \tag{2.14}$$

which allows the fractional flow of water (f_w) in the presence of foams to be written as follows:

$$f_w = \frac{u_w}{u_w + u_g} = \frac{Q_w}{Q_w + Q_g} = \frac{\frac{k_{rw}}{\mu_w}}{\frac{k_{rw}}{\mu_w} + \frac{k_{rg}^{f}}{\mu_g^{f}}} = \frac{\frac{k_{rw}}{\mu_w}}{\frac{k_{rw}}{\mu_w} + \frac{k_{rg}^{o}}{\mu_g^{o}\mathrm{MRF}}} = 1 - f_g \tag{2.15}$$

where Darcy's velocity is defined by flow rate (Q) divided by cross-sectional area (A) (i.e., $u_w = {Q_w}/{A}$, $u_g = {Q_g}/{A}$, and $u_t = u_w + u_g = {Q_w}/{A} + {Q_g}/{A} = {Q_t}/{A}$).

Table 2.1 lists the properties and parameters involved in this model, grouped into the basic rock and fluid properties, basic foam parameters, and mechanistic foam modeling parameters for this study. Note that the first group is what is needed for conventional gas-liquid two-phase flow (no foam), the second group is what can be either directly read from experimental data ($n_{f\,max}$ from the average pore size, σ_H and σ_L from foam coreflood experiments) or estimated from the literature ($X_{t\,max}$ and β), and the third

group is what makes the fit to the three foam states (i.e., S-shaped curve) and the reference pressure contour for strong foams (showing both high-quality and low-quality regimes) possible. The limiting water saturation, S_w^*, is somewhat special in that it first needs to be determined experimentally (just like the ones in the second group), then fine-tuned with other model parameters in the third group. More details on this issue are shown in the Result section below.

Table 2.1. Properties and parameters required for mechanistic foam modeling in this study.

Basic Rock and Fluid Properties	Basic Foam Parameters	Foam Modeling Parameters
Permeability (k) Porosity ($\emptyset$) Brine viscosity (μ_w) Gas viscosity (μ_g) Connate water saturation (S_{wc}) Residual gas saturation (S_{gr}) Corey-type relative permeability parameters (A, B, m_1, m_2)	Maximum foam texture (n_{fmax}) Maximum trapped gas fraction (X_{tmax}) Trapping parameter (β) Low-quality regime power-law exponent (σ_L) High-quality regime power-law exponent (σ_H)	Lamellae mobilization pressure (∇P_o) Lamellae coalescence exponent (n) Limiting water saturation (S_w^*) Coefficient for lamellae creation function ($\frac{C_g}{C_c}$) Coefficient for foam viscosity function (C_f)

Among many in the literature, the experimental study of Yin (2007) for supercritical CO_2 foam in Berea sandstone is selected because it offers much of the data required for model fit in a series of core-scale experiments. A companion study, Liu et al. (2010), provides relevant rock properties including relative permeability data at the same

experimental conditions. Their original data points are shown in Figure 2.4 (filled squares and open/filled circles) modified in the format required for this study. Briefly, Yin (2007) conducted two types of supercritical CO_2 foam coreflood experiments, one by varying liquid velocity (u_w = 0.042 – 1.256 ft/day) at fixed gas velocity (u_g = 1.51 ft/day), and the other by varying foam quality (f_g= 50% - 90%) at fixed total velocity (u_t = 3.778 ft/day). Other experimental conditions are summarized in Table 2.2. Note that the brine viscosity is estimated from McCain (1991) and supercritical CO_2 viscosity from Fenghour and Wakeham (1997). The approach applied in this study does not deal with capillary pressure directly but takes care of its effect implicitly through water saturation (e.g., limiting water saturation, relative permeability a function of saturation). This helps reducing the number of model input parameters.

Table 2.2. Conditions for coreflood experiments.

Experimental Conditions	Berea Core Rock Properties	Gas and Liquid Properties
Pressure: 1540 psig	Core length: 0.5 ft	Brine Viscosity: 0.65 cp (McCain,1991)
Temperature: 110 ^oF	Core diameter: 0.169 ft	
Gas Phase: CO_2	Pore Volume: 0.00241 ft^3	Gas Viscosity: 0.07 cp (Fenghour and Wakeham, 1998)
Aqueous Phase: 3 wt % NaCl brine	Porosity: 22.29 %	
Surfactant: Chaser CD1045™ 0.05 wt% concentration	Liquid Permeability: 450 md	

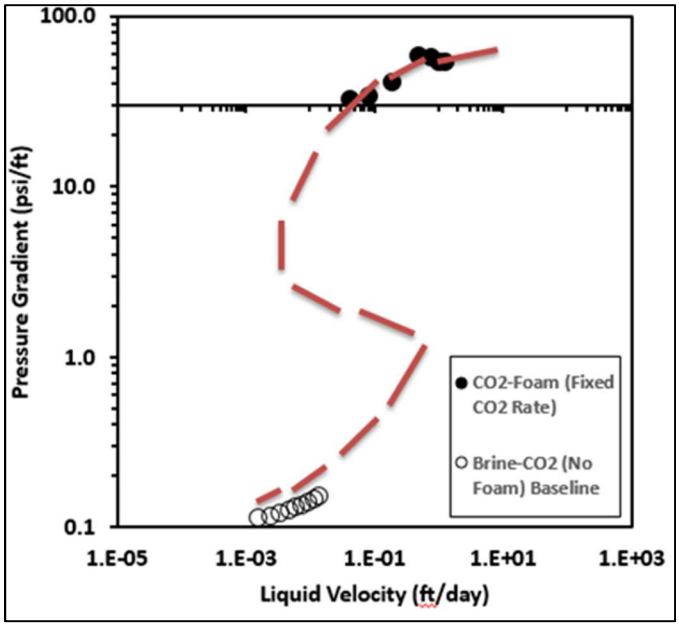

(a)

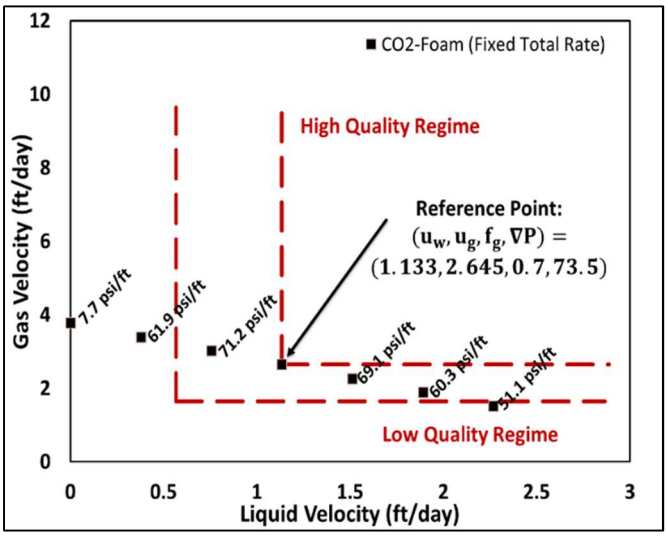

(b)

Figure 2.4. Original coreflood data points from Yin (2007) and Liu et al. (2010) in a format required for this study with expected model fits (dashed lines): (a) onto the S-shaped curve and (b) onto the two foam-flow regime pressure contours.

2.4. Results

This section consists of three parts: Part 1 shows how to determine the basic model parameters (i.e., first and second groups in Table 2.1), Part 2 presents how to make a fit to the S-shaped curve (i.e., hysteresis with three foam states) as well as two flow-regime pressure contours (i.e., high-quality and low-quality regimes) by determining foam model parameters (i.e., third group in Table 2.1), and Part 3 covers how foam propagates in a large system. For clarification, “a successful fit ” in this study means that the model (based on pore-scale events) captures the trend shown by one representative S-shaped curve (showing the path from weak-foam to strong-foam state) and two representative pressure contours (showing both high-quality and low-quality regimes) of strong foam state (shown in core-scale events). For example, Figure 2.4(a) shows coreflood data points, with strong foams as the upper surface and no foams as the lower limit for weak-foam surface, and Figure 2.4(b) shows the pressure responses of strong foams collected experimentally at different gas and liquid velocities (keeping the total velocity the same). The trend traced by dashed lines are what the population balance model aims to match in this study.

2.4.1. Part 1: How to determine basic model parameters

Each of these parameters are determined as follows.

CO_2-Brine Relative Permeability Curve: The Corey-type relative permeability functions are used for supercritical CO_2 and brine two-phase flow. Figure 2.5 shows how 4 parameters (m_1,m_2, A and B; see Equations 2.7 and 2.8) are determined to fit the experimental data from Liu et al. (2010) by performing curve fitting.

Maximum Foam Texture ($n_{f\,max}$): The maximum foam texture ($n_{f\,max}$) can be determined directly from the average pore size, i.e., $n_{f\,max}$ = 1/ (volume of individual pore). Beard and Weyl (1973) provided correlations between porosity, permeability, and grain size of different sandstone rocks, and in relatively homogeneous unconsolidated rocks, the average pore size is approximately 25 - 30% of the grain size. For a 450 md Berea sandstone sample in this study, the correlations provide the average grain size about 0.044 mm and thus the average pore size about $1.12 \times 10^{-14}\ m^3$. Therefore, $n_{f\,max}$ is approximately $8.0 \times 10^{14}\ \frac{1}{m^3}$ which is used as a model parameter (Table 2.3).

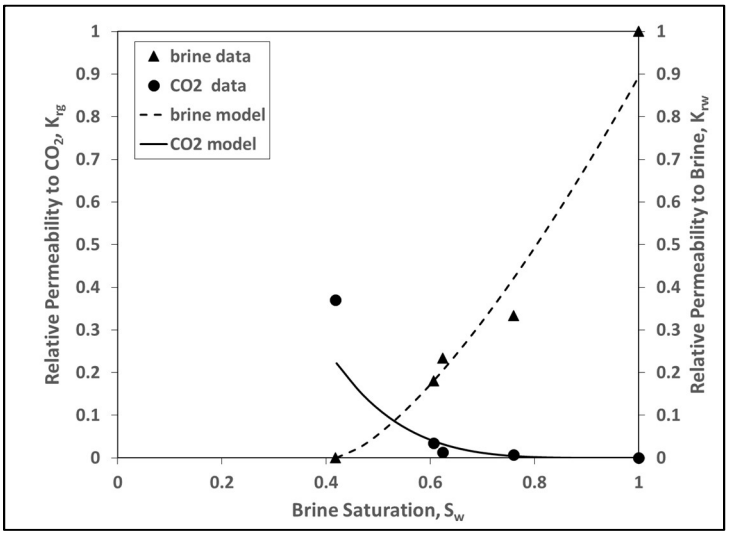

Figure 2.5. Determination of supercritical CO_2-Brine two-phase relative permeability curves by using Corey-type functions.

Mobility Reduction Factor (MRF) and Limiting Water Saturation (S_w^*): The magnitude of MRF (Equation 2.14 and Equation 2.15) can be determined by plotting fractional flow curves (i.e., f_w vs. S_w) at various MRF values and choosing the one that

fits the experimental data appropriately. Figure 2.6 shows an example. The curve with MRF = 1 is for the case of conventional gas-water (i.e., supercritical CO_2 and brine) two-phase flow with no foams. With foams present in the media, the fractional flow curve shifts to the left (cf. Equation 2.15). Overall, the data points from Yin (2007) suggest the MRF in this experiment falls between 100 and 1000. In addition, no matter what MRF values are, the fractional flow curves steeply fall to join no-foam fractional flow curve (MRF=1) as S_w approaches S_w^* . It is because the rate of lamellae coalescence increases dramatically near S_w^* (cf. Equation 2.3). The figure suggests that the range of limiting water saturation is around 0.42 - 0.43, slightly above the connate water saturation (S_{wc} = 0.42).

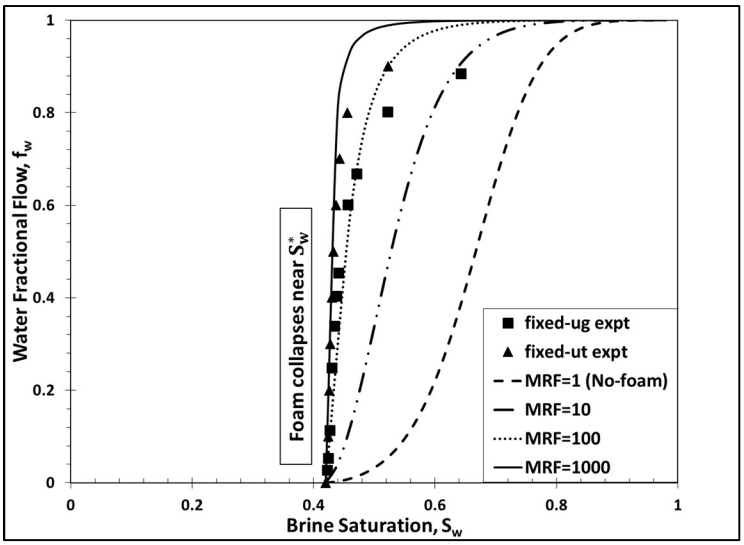

Figure 2.6. Construction of fractional flow curves at various MRF values to capture the range of MRF and S_w^* (experimental data from Yin (2007)).

Shear thinning/thickening parameters: The gap between pressure contour lines in the two flow-regime map in Figure 2.4(b) can be used to determine if foams in the high-quality and low-quality regimes are shear-thinning, shear-thickening, or near-Newtonian. The data points for f_g = 0.7 through f_g = 1.0 in Figure 2.4(b) are used to calculate the power-law exponent in the high-quality regime (σ_H), while the data points for f_g= 0.5 through f_g= 0.7 in Figure 2.4(b) are used to calculate the power-law exponent in the low-quality regime (σ_L). The original data at foam quality less than 50% (f_g < 0.5) is neglected because they are too wet to call foam. Figure 2.7 illustrates how to determine σ_H (σ_H= 0.2984) and σ_L (σ_L= 0.5744) plotting the pressure gradient as a function of gas and liquid velocities, respectively.

Mobilization Pressure Gradient: When Figure 2.2(a) from Gauglitz et al. (2002) is used for the permeability of sandstone used in this study (200-500 md), ∇P_o ranges from 7 to 30 psi/ft (or, about 158,000-678,000 Pa/m) for N_2 foams and 0.4 to 6 psi/ft (or, about 9,000-135,000 Pa/m) for supercritical CO_2 foams.

Lamellae Coalescence Exponent: The lamellae coalescence exponent (n) in Equation 2.3 describes the rate of kinetics of lamella coalescence mechanism, i.e., how quickly lamella coalescence occurs when S_w approaches (decreases) to S_w^*. There are no experimental studies reported in the literature to measure n value within the porous media, to our knowledge. Most of the previous studies use n value of either 1 (Friedmann et al., 1991; Kovscek and Bertin, 2002; Kam, 2008) or 2 (Kovscek et al. (1995)) as a

reasonable approximation. These previous studies show that n does not affect the steady-state model fit significantly except for foams in very high f_g (or, S_w very close to S_w^*) but does impact the stability and convergence of dynamic foam simulation.

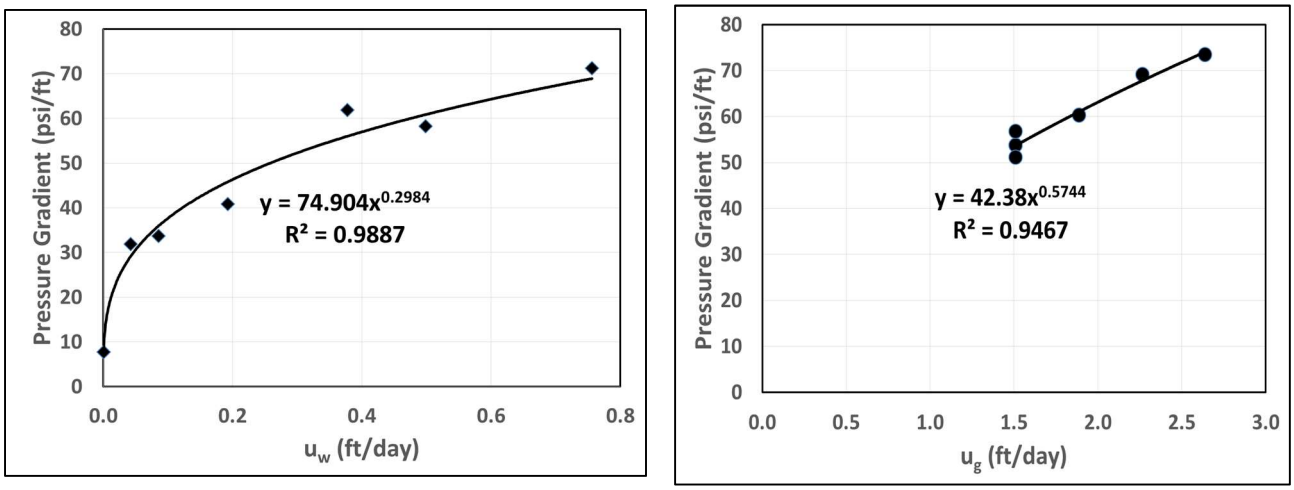

(a) (b)

Figure 2.7. Determination of power-law exponents: (a) for the high-quality regime (σ_H) from ∇P vs. u_w plot and (b) for the low-quality regime (σ_L) from ∇P vs. u_g plot.

Maximum Trapped Gas Fraction and Trapping Parameter: The trapped gas fraction, X_t, is calculated by using an equation similar to Langmuir isotherm (Equation 2.10) that has the maximum trapped gas fraction($X_{t\,max}$) and trapping parameter (β) .There are some studies that measured $X_{t\,max}$ experimentally by using tracer tests or numerically calculated from pressure response, while there are no experimental studies that reported β values- once again it is because of difficulties measuring the dynamics of lamella movement within the porous media. Kovscek and Radke (1994) reported the value of 0.9 for $X_{t\,max}$ and 10^{-9} m^3 for β in their model fit to experimental data. Kam (2008),

Afsharpoor et al. (2010), and Lee et al. (2016) used 0.8 and 10^{-11} m^3 for $X_{t\,max}$ and β respectively. Chen et al. (2010) had the maximum trapped gas fraction of 0.78 for the N_2 foam in Berea sandstone. Lotfollahi et al. (2016) estimated values of $X_{t\,max}$ and β for the CO_2 foam in South Cowden Unit Cores 0.5 and 10^{-9} m^3 respectively. This study assumes $X_{t\,max}$ to be 0.7 and β to be $5 \times 10^{-14}\ m^3$.

Table 2.3. Basic model parameters and their values.

Parameter Name	Parameter Value	Parameter Name	Parameter Value
Corey-type coefficient for water relative permeability (A)	0.893	Mobilization pressure gradient $(\nabla P_o, \frac{psi}{ft})$	$0.4 \leq \nabla P_o \leq 6.0$
Corey-type exponent for water relative permeability (m_1)	1.41	Maximum trapped gas fraction (X_{tmax})	0.7
Corey-type coefficient for gas relative permeability (B)	0.222	High quality regime Power-law exponent (σ_H)	0.2984
Corey-type exponent for gas relative permeability (m_2)	4.45	Low quality regime Power-law exponent (σ_L)	0.5744
Connate water saturation (S_{wc})	0.42	Limiting water saturation (S_w^*)	$0.42 < S_w^* \leq 0.43$
Residual gas saturation (S_{gr})	0.0	Lamellae coalescence exponent (n)	1.0
Maximum foam texture $(n_{f\,max}, \frac{1}{m^3})$	8.0 x 10^{14}	Trapping parameter (β, m^3)	5.0 x 10^{-14}

2.4.2. Part 2: How to determine mechanistic model parameters

With the basic parameter values as discussed and summarized in Table 2.3, there are five more model parameters required (∇P_o, S_w^*, n, $\frac{C_g}{C_c}$, and C_f (see the third column of Table 2.1)) in order to fit the experimentally measured S-shaped curve and two flow-regime contours. Note that ∇P_o and S_w^* values are not determined yet (the ranges are estimated in Part 1, 0.4-6 psi/ft and 0.42-0.43 respectively, however). Also note that $\frac{C_g}{C_c}$, as a single parameter, plays a role in steady-state modeling, although they split into two different parameters playing different roles in dynamic simulations (Kam, 2008). This study selects ∇P_o of 5 psi/ft as a base case first and investigate how the fit changes at different ∇P_ovalues.

Figure 2.8 shows a model fit to both S-shaped curve and two flow-regime pressure contours. In the two flow regime contours, the point of (u_w, u_g) = (1.133 ft/day, 2.645 ft/day), giving f_g^*= 70% and ∇P = 73.5 psi/ft, is selected as the reference point (i.e., the boundary between the high-quality regime and low-quality regime). With given values of n and ∇P_o, a selection of S_w^* allows two other parameters ($\frac{C_g}{C_c}$ and C_f) to be determined automatically. Three sets of plots, Figures 2.8(a) through 2.8(c), are created at S_w^* = 0.421, 0.422, and 0.426 respectively, and those corresponding sets of five parameters are tabulated in Table 2.4. Although all three pairs of figures look equally nice, a couple of differences are observed: (i) the match to the upper surface of the S-shaped curve deviates further and further as S_w^* increases; (ii) the turning point from the weak-foam to intermediate state occurs at lower liquid velocity as S_w^* increases; and (iii) the pressure contours in the high-

quality regime tend to be more vertical with a sharper transition between the two flow regimes (the pressure contours in the low-quality regime tends to remain almost the same, however). With further lab-measured information (for example, the onset of foam generation (i.e., the turning point from weak-foam to intermediate state), pressure data for weak-foam state, or additional steady-state pressure-gradient data in the two flow-regime map (especially in the upper left corner of the plot)), one can further narrow down the set of input parameters. It must be re-emphasized that the changes shown in Figures 2.8(a) through 2.8(c) happen within the range of S_w^*= 0.421 through 0.426 (about 1.5%). Such a precision is often very difficult to obtain even in the sophisticated coreflood tests, but causes a considerable difference in terms of model fit. This again proves the validity of the approach in this study – determine the range of S_w^* from lab tests and then pinpoint exactly what value to be used in numerical simulations from mechanistic foam model. As described earlier, ∇P_o ranges from 0.4 to 6.0 psi/ft for supercritical CO_2 foams for the permeability range of 200 to 500 md. In addition to the base-case ∇P_o value of 5 psi/ft, the calculations are extended to ∇P_o= 1 and 30 psi/ft for sensitivity study, as shown in Figures 2.9 and 2.10 respectively, still at the same three S_w^* values of 0.421, 0.422, and 0.426. Both ∇P_o values capture the trend reasonably well, showing the same symptoms presented in the base case (i.e., the upper surface of the S-shaped curve shifting to the right, the transition from the weak-foam to intermediate state happens at lower liquid velocity, and the contours in the high-quality regime more vertical as S_w^* increases). It is interesting to find that ∇P_o = 1 psi/ft provides almost no intermediate state, while ∇P_o = 30 psi/ft provides much more elongated weak-foam state as well as intermediate state. This explains why placing supercritical CO_2 foams further into the reservoir is much easier than

gaseous foams – with a lower ∇P_o as an input parameter, foams can be created and mobilized at lower pressure-gradient conditions, allowing the placement further into the reservoir. The input parameters for Figures 2.9 and 2.10 are shown in Tables 2.5 and 2.6, respectively.

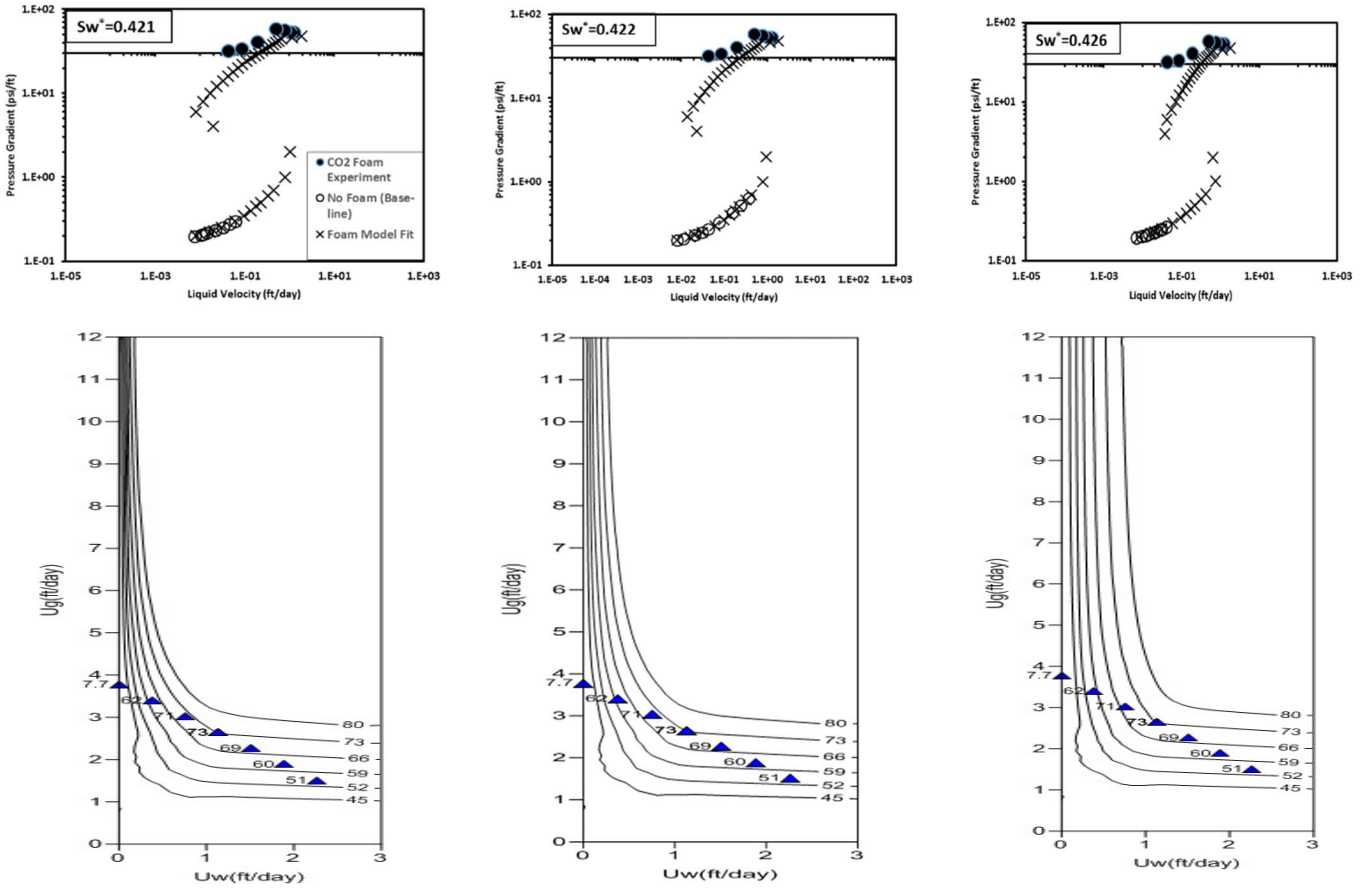

(a) (b) (c)

Figure 2.8. Model fit to three foam states as well as two foam-flow regime pressure contours at ∇P_o = 5 psi/ft at three different sets of parameters represented by (a) S_w^* = 0.421, (b) S_w^* = 0.422, and (c) S_w^* = 0.426 (See Table 2.4 for more details).

Table 2.4. Summary of base-case model parameters (∇P_o = 5 psi/ft) to fit three foam states (S-shaped curve) and two flow regimes (see Figure 2.8).

Foam Model Parameters	@ $S_w^* = 0.421$	@ $S_w^* = 0.422$	@ $S_w^* = 0.426$
∇P_o, (psi/ft)	5.0	5.0	5.0
n, (dimensionless)	1.0	1.0	1.0
$\frac{C_g}{C_c}$, ($s^2/(kg.m^2)$)	3.30743 x 10^{16}	3.65796 x 10^{16}	6.34985 x 10^{16}
C_f, ($m^{7/3}.kg/s^{4/3}$)	2.07342 x 10^{-21}	2.07342 x 10^{-21}	2.07342 x 10^{-21}

Table 2.5. Summary of base-case model parameters (∇P_o= 1 psi/ft) to fit three foam states and two flow regimes (see Figure 2.9).

Foam Model Parameters	@ $S_w^* = 0.421$	@ $S_w^* = 0.422$	@ $S_w^* = 0.426$
∇P_o, (psi/ft)	1.0	1.0	1.0
n, (dimensionless)	1.0	1.0	1.0
$\frac{C_g}{C_c}$, ($s^2/(kg.m^2)$)	3.93113 x 10^{16}	4.34776 x 10^{16}	7.54726 x 10^{16}
C_f, ($m^{7/3}.kg/s^{4/3}$)	2.07342 x 10^{-21}	2.07342 x 10^{-21}	2.07342 x 10^{-21}

Table 2.6. Summary of base-case model parameters (∇P_o = 30 psi/ft) to fit three foam states and two flow regimes (see Figure 2.10).

Foam Model Parameters	@ $S_w^* = 0.421$	@ $S_w^* = 0.422$	@ $S_w^* = 0.426$
∇P_o, (psi/ft)	30.0	30.0	30.0
n, (dimensionless)	1.0	1.0	1.0
$\frac{C_g}{C_c}$, ($s^2/(kg.m^2)$)	3.30743 x 10^{16}	3.65796 x 10^{16}	6.34985 x 10^{16}
C_f, ($m^{7/3}.kg/s^{4/3}$)	2.07342 x 10^{-21}	2.07342 x 10^{-21}	2.07342 x 10^{-21}

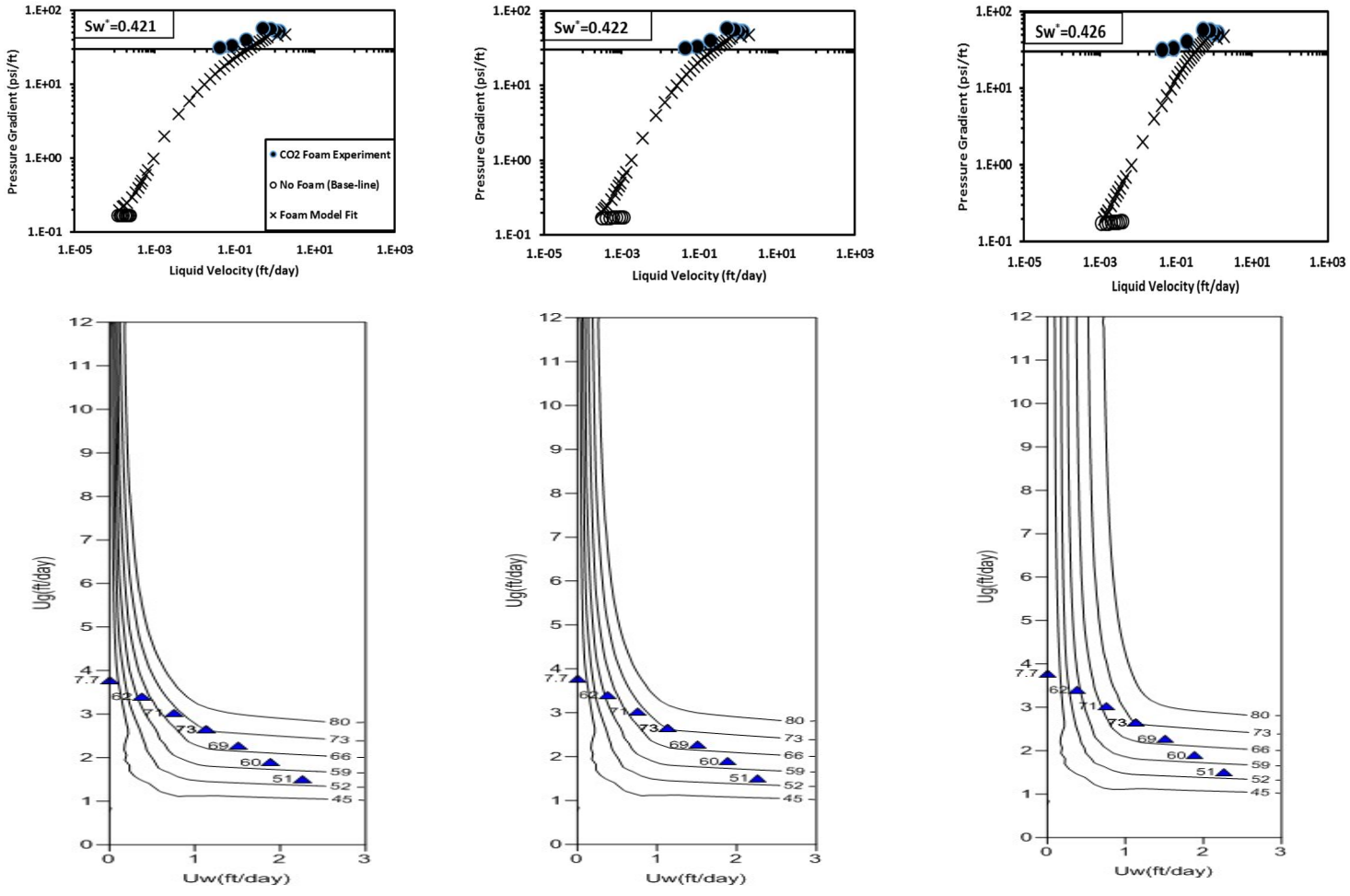

(a) (b) (c)

Figure 2.9. Model fit to three foam states as well as two foam-flow regime pressure contours at ∇P_o = 1 psi/ft at three different sets of parameters represented by (a) S_w^* = 0.421, (b) S_w^* = 0.422, and (c) S_w^* = 0.426 (See Table 2.5 for more details).

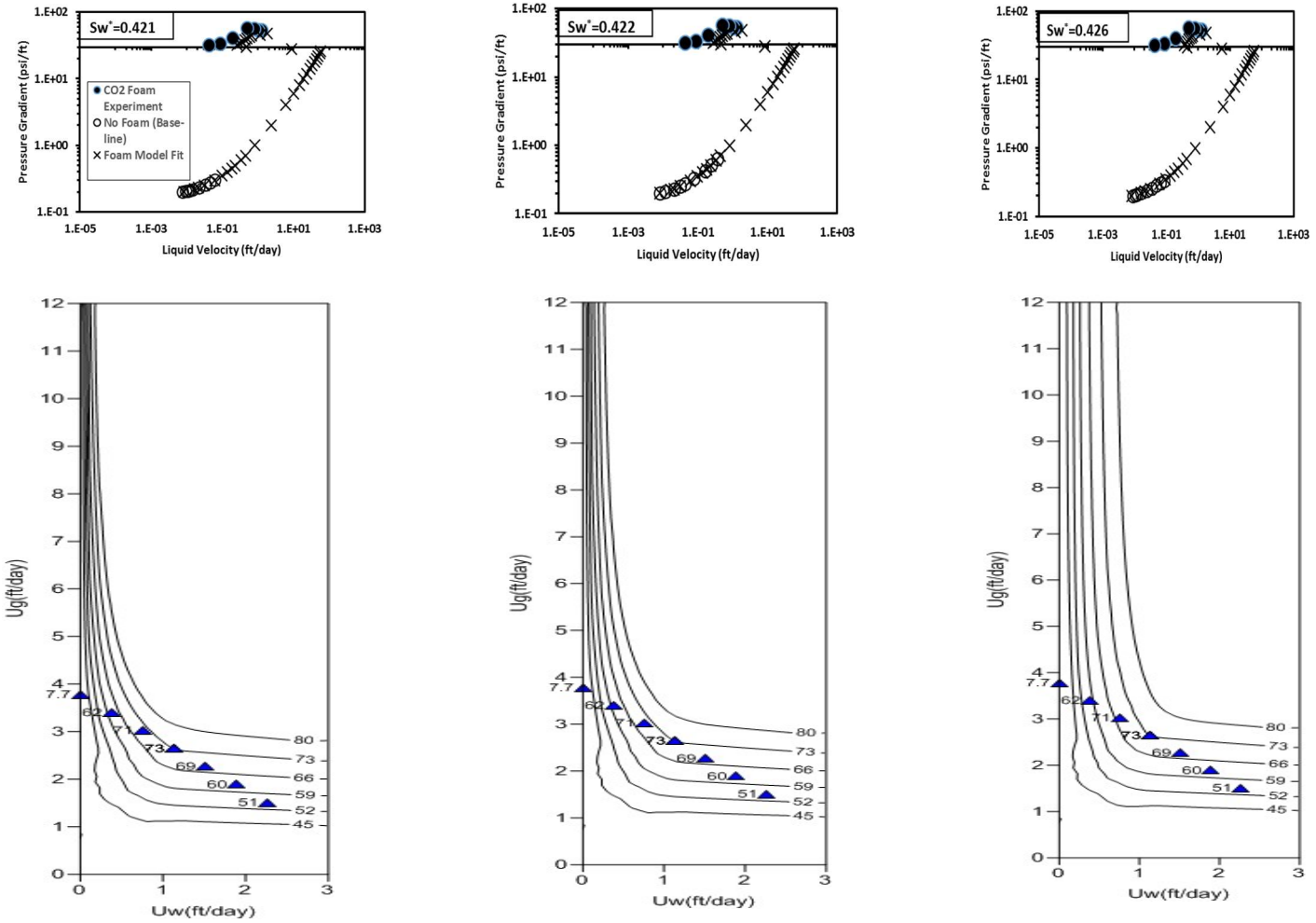

Figure 2.10. Model fit to three foam states as well as two foam-flow regime pressure contours at ∇P_o = 30 psi/ft at three different sets of parameters represented by (a) S_w^* = 0.421, (b) S_w^* = 0.422, and (c) S_w^* = 0.426 (See Table 2.6 for more details).

The sensitivity of model fit to other model parameters is also conducted, but not included, due to the limited space. Briefly summarizing, for example, larger n (foam coalescence exponent; Equation 2.3), let's say, n = 2 rather than 1, does not make any noticeable changes except where foam rheology is governed by S_w^* (or, strong foams in the high-quality regime). Because bubble instability, as S_w approaches S_w^*, occurs more rapidly with larger n, the top of the S-shaped curve tends to be flattened out and the contours in the high-quality regime become more vertical. Another example is the trapped gas fraction (X_{tmax}) and related kinetic parameter (β) (Equation (2.10)), where the former is estimated from similar experiments in the literature while the latter has never been measured from the lab (but only estimated in some previous modeling studies). Lower X_{tmax} tends to cause the the transition from the weak-foam to intermediate state at lower pressure gradient (meaning a shift of S-shaped curve to the lower-left), because foam approaches the finer-texture condition more easily. On the contrary, lower β tends to delay reaching the strong foam state and thus stretches out the transition from the intermediate to strong foam state vertically. In fact, a better fit to the S-shaped curve can be made, but with a sacrifice in two-flow regime contours. The interplay between X_{tmax} and β to data fit is more complicated, however.

2.4.3. Part 3: How to determine foam propagation in the field scale

The model fit to core-scale experimental data can be used to understand how far from the wellbore foam propagates in field-scale applications (note that the propagation distance coincides with the radial region in which MRF values are relatively high, representing the top surface of the S-shaped curve). As an example, this study assumes

a hypothetical cylindrical reservoir (wellbore radius = 0.42 ft and height = 275 ft, from a supercritical CO_2 foam pilot test of the Weber Sand Unit of Rangely field, Colorado (1990)) with total injection rate (Q_t) of 17,970 ft3/day (3,200 bbl/day or 0.01797 MMscf/day, equivalently). Both gas and liquid can be viewed incompressible in this test, which is believed to be a reasonable assumption at high reservoir pressure and supercritical CO_2 phase. Two injection conditions are considered such as injection foam quality of 90% (i.e., $Q_w = 320$ bbl/day and $Q_g = 0.016173$ MMscf/day) and 60% (i.e., $Q_w = 1280$ bbl/day and $Q_g = 0.010782$ MMscf/day). They represent strong foams in the high-quality regime and low-quality regime, respectively, as shown in Figures 2.11 and 2.12, at three different ∇P_o values (see Tables 2.4, 2.5, and 2.6 for input parameters).

A few interesting observations are made. First, the plots show that the MRF (y axis) folds back and forth for ∇P_o = 5 and 30 psi/ft, presenting multi-valued solutions to the radial distance, while MRF changes rather smoothly for ∇P_o = 1 psi/ft, presenting a single-valued solution. This behavior is consistent with Figures 2.8 through 2.10. Second, in both high-quality-regime and low-quality-regime foams, foams with lower ∇P_o propagate much further into the reservoir. Such results demonstrate the advantage of supercritical CO_2 foams over other gaseous foams (for example, Figure 2.11 shows only “4 and 25 ft for ∇P_o = 30 and 5 psi/ft respectively” vs. as much as “136 ft (MRF = 100) and 418 ft (MRF = 10) for ∇P_o = 1 psi/ft”. Similarly, Figure 2.12 shows only “5 and 35 ft for ∇P_o = 30 and 5 psi/ft, respectively” vs. “362 ft (MRF = 100) and 1077 ft (MRF = 10) for ∇P_o = 1 psi/ft”. Third, the propagation distance for low-quality-regime foams is more than that for high-quality-regime foams. It is because the former has more stable foams (away from S_w^*)

with fine foam texture ($n_f = n_{f\,max}$), while the latter has less stable foams (near S_w^*) with coarse foam texture ($n_f << n_{f\,max}$). Last, the MRF values for the low-quality-regime foams are higher compared to those for the high-quality-regime foams. Note that the change in MRF in Figures 2.11 and 2.12 in fact reflects the change in apparent foam viscosity (cf. Equations 2.11 and 2.14) that accommodates foam stability at different capillary pressure environments as well as resulting non-Newtonian foam rheology and bubble population balance.

It must be emphasized that the propagation radial distance (x axis in Figures 2.11 and 2.12) is inversely proportional to reservoir thickness. Therefore, if the thickness were 10 times less (27.5 ft rather than 275 ft), the propagation distance in Figures 2.11 and 2.12 would be 10 times more at the same injection rate. How far foam travels in a large field-scale system during EOR processes depends on foam rheology, mobility as well as segregation by gravity in a multi-dimensional space. The next chapter investigates such issues relying on the population-balance model presented in this chapter.

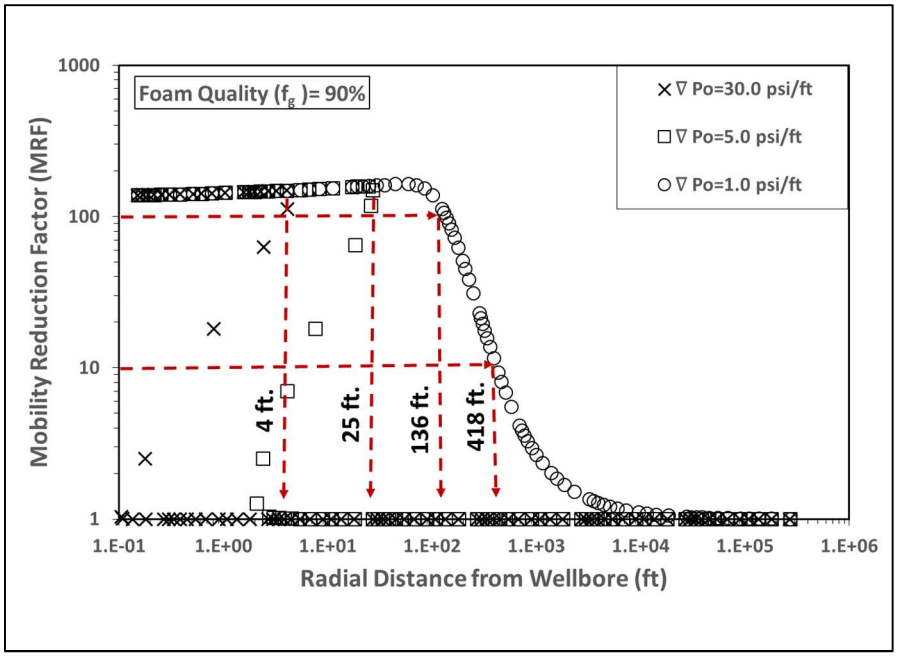

Figure 2.11. Foam propagation in a 275-ft thick cylindrical reservoir at three different values of mobilization pressure gradient (1.0, 5.0, and 30.0 psi/ft) by using high-quality-regime foams (foam quality = 90%) (See Tables 2.4, 2.5, and 2.6 for input parameters).

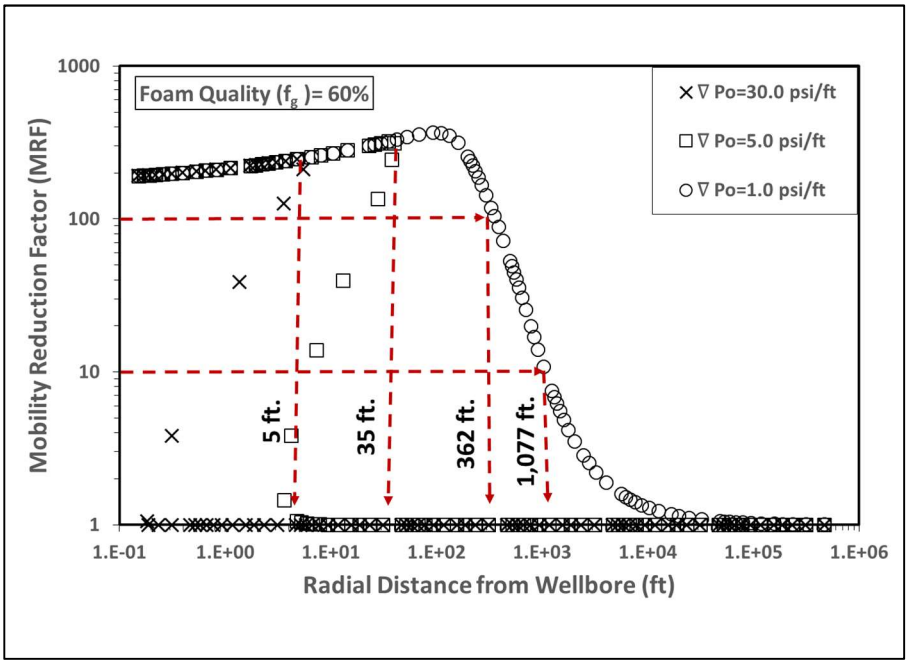

Figure 2.12. Foam propagation in a 275-ft thick cylindrical reservoir at three different values of mobilization pressure gradient (1.0, 5.0, and 30.0 psi/ft) by using low-quality-regime foams (foam quality = 60%) (See Tables 2.4, 2.5, and 2.6 for input parameters).

2.5. Discussions

The model fit to experimental data of three foam states and two strong-foam flow regimes (Figures 2.8, 2.9, and 2.10) helps determine many of model parameters but, in its current form, this study cannot pinpoint the sets of input parameters further unfortunately (for example, Figures 2.8(a) vs. 2.8(b) vs. 2.8(c)). It is because the experimental data available to this study have the properties of strong foams, just like the way foams are injected in the field tests; the prediction of foam propagation using bubble population model requires properties of weak-foam and intermediate states as well, however, in addition to strong-foam state. Such a gap suggests that design and implementation of field-scale EOR treatments have both of numerical modeling/simulation and lab experiment components aligned together cohesively.

The following chapter compares this population-balance model with implicit-texture foam model, when supercritical CO_2 foams are injected into a cylindrical reservoir in EOR processes. When the reduction in gas-phase mobility is determined from the mechanistic model (cf. Figures 2.11 and 2.12) and the resulting distance-averaged MRF values are carefully selected, the two modeling techniques predict comparable foam propagation distances. The study demonstrates how the two modeling techniques – one computationally more intensive but based on detailed mechanistic mechanisms, while the other more user-friendly and simpler but still capturing key mechanisms - help each other to improve the quality of reservoir simulations.

This study demonstrates another interesting point on why supercritical CO_2 foams are better than gaseous foams to improve oil recovery in the field. Typical justifications behind the use of supercritical CO_2 foams include a favorable miscibility condition with oleic components, a swelling behavior when in contact with reservoir oil, and high-density and high-viscosity property of a supercritical phase of CO_2. The results from this study show another important reason, that is, supercritical CO_2 foams can propagate more easily, being placed deeper into the reservoir much further than gaseous foams (even a few orders of magnitude more), because of much lower mobilization pressure gradient (∇P_o), and thus improve sweep efficiency greatly.

There are many physical and chemical properties that obviously affect foam rheology in lab experiments but do not show up explicitly in the model used in this study. The model, however, is equipped with capabilities dealing with those properties indirectly. For example, a better foamer (e.g. by changing surfactant formulation and concentration endowing foams improved stability) can be represented by higher yield stress of lamellae, higher foam viscosity, higher f_g^*, and higher trapped gas saturation. More oil-wet media can be represented by properties similar to a poorer foamer (i.e., opposite to the previous example) as well as changes in relative permeability curves. A change in interfacial tension can be incorporated by foam stability and lamella creation and coalescence mechanisms (through mobilization pressure and limiting water saturation).

It must be commented that the experimental results for continuous foam rheology surface as shown in Figures 2.1(a) and 2.1(b), exhibiting the data points for both “three different foam states” and “two strong foam regimes”, are very rare in the literature. In

fact, even though there is sufficient experimental evidence in pieces, the only complete data set available in the literature is for N_2 gaseous foams (Gauglitz et al., 2002; Kam and Rossen, 2003). As a result, the fact that the model fit in this study is made for supercritical CO_2 foams without data points in the intermediate state (cf. Figures 2.4(a) and 2.4(b)) adds some uncertainty to this study, and this in turn emphasizes the importance of experimental studies for modeling purpose. See Yu et al. (2018) for more discussions on this aspect.

2.6. Conclusions

This chapter investigates the mechanisms of supercritical CO_2 foam propagation by using a mechanistic foam model. The procedure to fit to the coreflood experimental data is presented in detail, together with the uniqueness of the input parameters and implication of the model in large field-scale applications. The major findings can be summarized as follows:

- This study investigates the mechanisms of supercritical CO_2 foam propagation by using a bubble-population-balance foam model based on pore-scale events. How to fit the model to lab coreflood data, which is core-scale events, is presented in a step-by-step manner, including three foam states and two foam-flow regimes for supercritical CO_2 foams. This is the first attempt of mechanistic foam modeling, in its kind, focusing on supercritical CO_2 foams with much lower mobilization pressure gradient (∇P_o) than other gaseous foams, which has not been studies earlier.

- The results also provide a theoretical reasoning why supercritical CO_2 foam can propagate further into the reservoir, as much as a few orders of magnitude, than other gaseous foams, and how much quantitatively. It is primarily because of lower mobilization pressure gradient (∇P_o) of supercritical CO_2 foams, which leads to smooth and monotonic changes from weak-foam to strong-foam state directly with no intermediate state in between. As a result, it seems very realistic that supercritical CO_2 foams with the mobilization pressure gradient less than 1 psi/ft can propagate a few hundreds or thousands of feet easily.

- With model parameters determined, the mechanistic model is applied to field-scale CO_2 foam EOR events, showing key concepts of foam propagation in large-scale applications. The results based on foam fundamentals and theoretical grounds demonstrate why the propagation distance is greater when wetter foams are used than drier foams. It is because of improved foam stability in the low-quality regime than in the high-quality regime.

CHAPTER 3. INVESTIGATING SUPERCRITICAL CO2 FOAM PROPAGATION DISTANCE: CONVERSION FROM STRONG FOAM TO WEAK FOAM VS. GRAVITY SEGREGATION

3.1. Introduction

3.1.1. EOR using gas and water injection

Gas injection is one of the most widely used methods in enhanced oil recovery (EOR) processes, because of its economic advantages. The gas phase (commonly CO_2, N_2, produced natural gas, flue gas, or a combination of these) is injected into the reservoir either as miscible or immiscible with reservoir oil. Since these gas phases generally have lower viscosity and density compared to the reservoir fluids, an early breakthrough of the injected gas into the production well typically occurs resulting in poor sweep efficiency. The main underlying mechanism behind it is the instability at the interface between the displacing and displaced phases caused by poor mobility ratio (leading to fingering or channeling) and density contrast (leading to gravity segregation).

Extensive research efforts have been made to predict the volume fraction of a reservoir that can be swept by gas injection at different reservoir and fluid conditions. For example, many laboratory studies in early days (Dyes et al. 1954; Offeringa and Van Der Poel 1954; Blackwell et al. 1959) found out that the low-viscosity and low-density gas tends to channel through and bypass oil in sands with no dip angles. Therefore, in horizontal sands, gas flooding is less efficient as the oil viscosity increases, and the desired oil recovery can be achieved only by injecting a large volume of gas. For dipping sands, there is a competition between gravity segregation and channeling (Lacey et al. 1958). There exists a critical rate (Hill and Inst 1952; Dietz 1953) below which gravity

segregation prevails and no channeling occurs, and above which channeling plays a more significant role.

Caudle and Dyes (1957) first suggested the simultaneous injection of water and gas as a method to improve sweep efficiency over gas injection. It was based on the fact that water, if flowing together with gas, decreases gas relative permeability. They attempted to determine the optimal gas-water injection ratio, by using relative permeability curves and fluid viscosities, resulting in the conditions at which gas and water flow at the same velocity.

It is sometimes more convenient in the field tests to inject water alternatively with gas, rather than water and gas co-injection, and this process is called water alternating gas (WAG). Christensen et al. (2001) provide a thorough review of WAG field experiences. The initial design of a WAG process is usually constructed by reservoir simulation studies and then the design is optimized, as the field process matures, with recommended gas slug size (i.e., volume of gas to be injected) and WAG ratio (Attanucci et al. 1993). Blackwell et al. (1959) investigated the effect of gravity on WAG process to find that the mobility of gas-water region becomes less of an issue as gas and water segregate more rapidly.

Stone (1982) first investigated the gravity segregation of gas from liquid for water and gas co-injections in a homogenous reservoir once water fractional flow (f_w) or gas fractional flow (f_g) is given (note $f_w + f_g = 1$). He developed an analytical equation by

applying the Buckley-Leverett (1942) theory to predict the size of the region around the injection well where vertical conformance was good before complete segregation. Jenkins (1984) extended Stone's equations to obtain a closed-form solution to the equations for estimation of incremental recovery beyond waterflooding for homogenous reservoirs. Combining these two together, so-called Stone and Jenkins model is shown to be also valid in the presence of surfactants (Rossen and Shen 2007), even though it was originally designed for gas-water co-injection. Figure 3.1 shows three constant regions at the steady state which represent a gas override region (i.e., only gas flowing ($f_g = 1$ and $f_w = 0$) at residual water saturation (S_{wr})), a water underride region (i.e., only water flowing ($f_g = 0$ and $f_w = 1$) at residual gas saturation (S_{gr})), and a mixed region in between (i.e., both gas and water flowing at constant water saturation (S_w)). Note that the prediction of "travelling distance before complete segregation by gravity (R_{gs})" is key to successful field implementation during gas-liquid co-injection EOR processes.

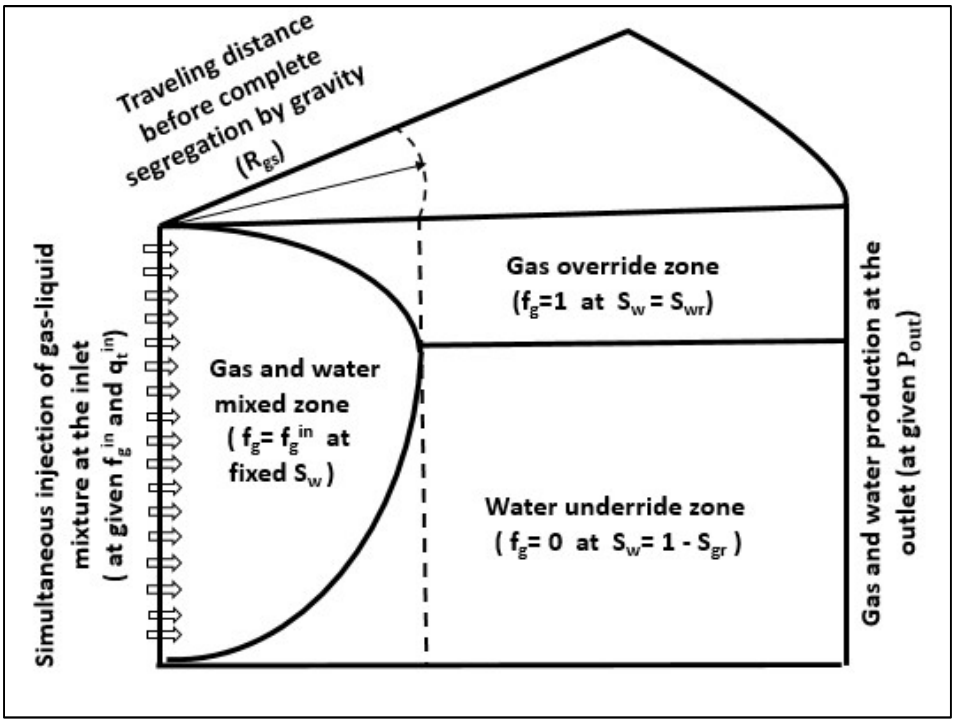

Figure 3.1. Three constant-state regions observed at the steady-state gas-liquid co-injection in 2D space predicted by earlier studies (Stone (1982), Jenkins (1984), and Rossen and Shen (2007)) (gas and liquid phases are assumed to be incompressible).

3.1.2. Gravity segregation during foam EOR process

Foaming gas with surfactant solutions has been suggested to mitigate gravity segregation and improve the mobility ratio within the mixed region (Shi and Rossen 1998). From a series of two-dimensional laboratory experiments, Holt and Vassenden (1997) found reasonably good agreement between the Stone and Jenkins model and their experimental results for the complete gravity segregation distance (i.e., R_{gs} in Figure 3.1) in gas and water co-injection tests. They observed, however, that when foam is injected, the segregation into gas and liquid is difficult to measure in small-scale experiments because of kinetics involved in foam decay. Rossen and van Duijn (2004) showed that

the Stone and Jenkins model is rigorously correct to use for foam if several assumptions are met. Those assumptions include (a) homogenous reservoir, although anisotropic, (b) cylindrical reservoir with open outer boundary, (c) injection well penetrates full reservoir height, (d) steady-state conditions reached during the injection, (e) incompressible phases, (f) no dispersion, and (g) Newtonian rheology for all phases. Analytical modeling (Stone 1982; Jenkins 1984), simulation studies (Shi and Rossen 1998) and experimental results (Holt and Vassenden 1997) indicate that gravity override in foam depends on dimensionless gravity number that is the ratio of gravity force to viscous force.

Shi and Rossen (1998) performed several numerical simulations with homogeneous and anisotropic rectangular and radial reservoirs using UTCOMP (University of Texas Compositional Flood Simulation). They found that the Stone and Jenkins model matches remarkably well with simulation results over a wide range of reservoir properties, geometries, flow rates, foam qualities (or, gas fractions (f_g), equivalently), foam strengths, foam collapse mechanisms, and coarseness of simulation grids. The results also confirmed that a successful gas injection EOR to overcome gravity segregation, with and without foams, requires horizontal pressure gradient outweigh vertical pressure gradient. Performing N_2 foam numerical simulation using CMG-STARS, Rossen and Shen (2007) observed that at fixed injection rate, the length of injection interval does not affect the distance for gravity segregation. They proposed a first guess in required injection pressure by providing an explicit relationship between the injection well pressure and distance to the point of segregation.

3.1.3. Conversion of strong foam to weak foam

In addition to gravity segregation, there is another mechanism that limits foam propagation in field applications, that is, the conversion of strong foam into weak foam, as demonstrated in Figure 3.2. There is a threshold distance ($\mathrm{R_{csw}}$) beyond which fine-textured strong foam created near the well (often caused by the turbulence in the well) turns into coarsely-textured weak foam, as foam moves away from the injection well. Such a concept of three different states of foam when the pressure gradient ($\nabla \mathrm{P}$) is controlled was first suggested by the experimental study of Gauglitz et al. (2002) and incorporated into the mechanistic foam modeling later (Kam and Rossen 2003; Lee et al. 2016).

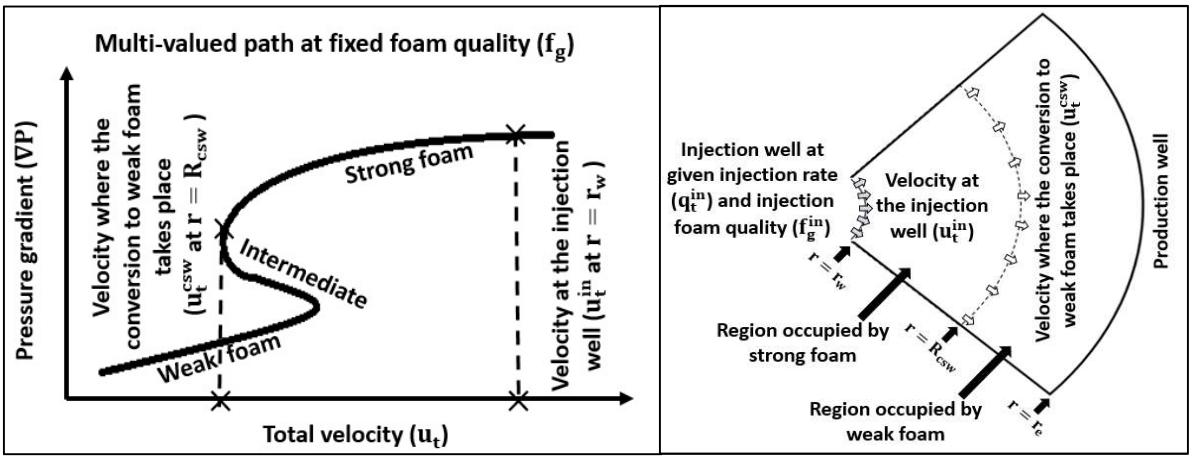

Figure 3.2. Three different foam states and its implication in field-scale applications (Gauglitz et al. (2002), Kam and Rossen (2003), and Lee et al. (2016)).

Figure 3.2 shows more details about what happens when strong foam is injected into a cylindrical reservoir at the total injection flow rate $\mathrm{q_t} = \mathrm{q_t^{in}}$ that corresponds to the

total injection velocity $u_t = u_t^{in}$. Note that q_t remains the same at any radial distance (r) between the wellbore radius (r_w) and the radius to the external boundary (r_e), if gas and liquid are incompressible, while u_t decreases with r (i.e., $u_t = \frac{q_t}{2\pi rH}$ at any r, for a cylindrical reservoir with the uniform thickness of H). It is the pressure gradient (∇P) that governs which state of foam is to be formed at given radial distance, because foam texture (n_f) increases with the pressure gradient (∇P) monotonically (Kam and Rossen 2003). For example, starting from the injection well ($r = r_w$), the reservoir is occupied by strong foam up to the distance where the conversion from strong foam to weak foam takes place ($r = R_{csw}$), and then by weak foam for the radial distance beyond ($r > R_{csw}$). Once strong foam is formed, the rheology follows the two flow regimes of strong-foam state as discovered by Osterloh and Jante (1992) and Alvarez et al. (2001). Foam rheology in the high-quality regime of strong-foam state is governed by bubble stability near the limiting capillary pressure (P_c^*) (or limiting water saturation (S_w^*)). On the contrary, foam rheology in the low-quality regime of strong-foam state is governed by the transport of bubbles at or near the maximum foam texture ($n_f = n_{fmax}$). Bubble population balance modeling, which this study is based on, is a modeling technique that deals with physical phenomena of bubble creation and coalescence, gas trapping, non-Newtonian rheology, and fluid transports in porous medium. It has been widely used in mechanistic foam modeling in the literature (Kovscek et al. 1995; Friedmann et al. 1991; Kam and Rossen 2003; Lee et al. 2016). Nearly all experimental foam studies have been conducted in linear system assuming the velocity remains constant as foam propagates into the system. In field scale, however, as foam moves away from the wellbore, the velocity decreases because of its radial

geometry. Due to the difficulty of conducting radial foam flow experiments in the lab, a mechanistic foam model is essential to translate foam rheology from linear to radial system.

3.2. Motivations and Objectives

The objective of this chapter is to predict how far supercritical CO_2 foam can propagate based on two different mechanisms, (i) the conversion of strong foam to weak foam (R_{csw}) and (ii) gravity segregation (R_{gs}), in a wide range of injection conditions. This study can be distinguished from other previous studies on similar topics as follows.

- First, how strong foam would propagate into the reservoir (before turning into weak foam) where the velocity monotonically decreases with radial distance has not been investigated before, especially when supercritical CO_2 foam with very low mobilization pressure gradient (∇P_o) is applied;
- Second, gravity segregation simulations with commercial software have been performed by many previous studies, but none of them employed gas-phase mobility reduction factors actually calibrated from mechanistic foam model (based on true foam physics and whose model parameters determined from actual model fit to lab data);
- Third, none of the previous studies in the literature have put the above two mechanisms together to demonstrate which of the two becomes more influential under what circumstances; and

- Finally, this study makes a unique contribution by presenting contour maps to show how far foam can travel, before converting to weak foam or gravity segregation, as a function of injection foam quality (f_g^{in}) and total injection rate (q_t^{in}), (or injection pressure (P_{in}), equivalently). This is especially important to fill the current gap present for the field implementation of supercritical CO_2 foams.

Note that a mechanistic model from Izadi and Kam (2018) (previous chapter) is used to provide mobility reduction factors (MRF) as an input parameter for gravity segregation simulations by CMG STARS. This study deals with a relatively ideal reservoir (i.e., large homogeneous cylindrical reservoir) in the absence of oil, as a first step, prior to the application in the real situations.

3.3. Methodology

3.3.1. Population balance modeling

A mechanistic modeling approach based on bubble population balance makes it possible to keep track of the population of bubbles (i.e., foam films or lamellae, equivalently), as foam propagates further into the reservoir. The mechanistic modeling approach captures not only the number of bubbles in unit volume of space (i.e., foam texture (n_f)) but also the relationship between foam texture and other variables such as effective gas viscosity (μ_g^f), changes in gas relative permeability (k_{rg}^f), trapped and flowing gas saturations (S_{gt},S_{gf}), non-Newtonian flow behavior and so on. Because this chapter investigates supercritical CO_2 foam placement in a homogeneous reservoir, a population

balance model based on the mobilization and division mechanism is applied. More details of such a model are available in the literature (Kam and Rossen 2003; Kam 2008; Lee at al. 2016; Ortiz Maestre, 2017), and all relevant equations are tabulated in Table 3.1 following the study of Izadi and Kam (2018). Note that the minimum mobilization pressure gradient (∇P_o) is defined as

$$\nabla P_o = 4\left(\sigma/R_t\right), \tag{3.1}$$

for a foam film to be mobilized out of pore throat with its radius R_t, if the interfacial tension between gas and liquid is given by σ. The minimum mobilization pressure gradient (∇P_o) for supercritical CO_2 foam can range less than 1.0 psi/ft easily (i.e., 0.05 – 5 psi/ft) with effective foamers, while it ranges around 10 – 30 psi/ft at a typical reservoir permeability (50 – 500 md) (Gauglitz et al., 2002; Georgiadis et al., 2010). The coefficient in Equation 3.1 is 4, rather than 2 (typically shown in Laplace equation), because a foam film consists of two gas-liquid interfaces with almost identical curvatures.

Table 3.1. A summary of bubble population balance model used in this study (see Izadi and Kam (2018) for more information).

Definition	Equation	Definition	Equation
Lamella creation rate	$R_g = \frac{C_g}{2}\left\{\mathrm{erf}\left(\frac{\nabla P - \nabla P_o}{\sqrt{2}}\right) - \mathrm{erf}\left(\frac{-\nabla P_o}{\sqrt{2}}\right)\right\}$	Gas relative permeability (no foam)	$k_{rg}^{o}(S_w) = B\left(\frac{1 - S_w - S_{gr}}{1 - S_{wc} - S_{gr}}\right)^{m_2}$
Lamella coalescence rate	$R_c = C_c n_f \left(\frac{S_w}{S_w - S_w^*}\right)^n$	Gas relative permeability with foam	$k_{rg}^{f}(S_w) = B\left(X_f \frac{1 - S_w - S_{gr}}{1 - S_{wc} - S_{gr}}\right)^{m_2}$
Foam texture	$n_f = \frac{C_g}{2C_c}\left(\frac{S_w - S_w^*}{S_w}\right)^n \left\{\mathrm{erf}\left(\frac{\nabla P - \nabla P_o}{\sqrt{2}}\right) - \mathrm{erf}\left(\frac{-\nabla P_o}{\sqrt{2}}\right)\right\}$	Trapped gas fraction	$X_t = X_{t\,max}\left(\frac{\beta n_f}{1 + \beta n_f}\right)$
Gas transport	$u_g = \frac{k k_{rg}^{o}(S_w)\nabla P}{\mu_g}$, $u_g = \frac{k k_{rg}^{f}(S_w)\nabla P}{\mu_g^f}$	Flowing and trapped gas saturation	$S_{gf} = S_g(1 - X_t)$ $S_{gt} = S_g X_t$ $S_g = S_{gf} + S_{gt}$

(table cont'd.)

Definition	Equation	Definition	Equation
Liquid transport	$u_w = \frac{k k_{rw}(S_w) \nabla P}{\mu_w}$	Gas viscosity with foam	$\mu_g^f = \mu_g^o + C_f n_f \left(\frac{u_g}{\emptyset S_g X_f} \right)^{-\frac{1}{3}}$
Liquid relative permeability	$k_{rw}(S_w) = A \left(\frac{S_w - S_{wc}}{1 - S_{wc} - S_{gr}} \right)^{m_1}$	Mobility reduction factor	$MRF = \frac{k_{rg}^o \mu_g^f}{k_{rg}^f \mu_g^o}$

3.3.2. Conversion from strong-foam to weak-foam states

Details on the model fit to CO_2 foam coreflood experiments are shown in Izadi and Kam (2018) (previous chapter). An example of foam model parameters from the study to match three different foam states (weak-foam, intermediate, and strong-foam states) and two flow regimes of strong foam state (high-quality regime and low-quality regime) is presented in Table 3.2. These input parameters are used as a basis for the prediction of foam propagation distance before strong foam turns into weak foam (R_{csw}) in this chapter, which is demonstrated in Figure 3.2 above.

Table 3.2. Mechanistic model parameters for supercritical CO_2 foam at different mobilization pressure values (∇P_o) fitting three different foam states and two flow regimes of strong foam state (see Table 3.1 for equations).

Foam Model Parameters	∇P_o (Pa/m; psi/ft) = 22620.6;1.0	∇P_o (Pa/m; psi/ft) = 113103; 5.0	∇P_o (Pa/m; psi/ft) = 678618; 30.0
n (dimensionless)	1.0	1.0	1.0
$\frac{C_g}{C_c}$ (1/m^3)	4.35 x 10^{16}	3.66 x 10^{16}	3.66 x 10^{16}
C_f (m$^{7/3}$.kg/s$^{4/3}$)	2.07 x 10^{-21}	2.07 x 10^{-21}	2.07 x 10^{-21}

(In all cases, S_w^* = 0.422; X_{tmax}= 0.7 and β =5x10^{-14}; f_g^* = 70 % at u_g = 9.331x10^{-6} m/s and u_w = 4.0 x 10^{-6} m/s. see Izadi and Kam (2018) for other petrophysical and fluid properties.)

In the case of gas-liquid co-injection EOR (at fixed f_g condition), the pre-specified total injection rate (q_t) corresponds to the total superficial velocity (u_t) that changes as a function of radial distance (Note that gas and liquid compressibility can be reasonably assumed negligible at the field pressure condition). For a homogeneous reservoir with constant thickness (H), the total velocity (u_t) at any given radial distance (r) is given by

$$u_t = \frac{q_t^{in}}{2\pi r H} \quad \text{for } r_w \le r \le r_e \tag{3.2}$$

As described earlier, the region with $u_t > u_t^{csw}$ (or $r < R_{csw}$) is occupied by strong foam, while the region beyond with $u_t < u_t^{csw}$ (or $r > R_{csw}$) is occupied by weak foam as depicted in Figure 3.2. Note that u_t decreases monotonically with r, even though the total rate (q_t) remains the same (i.e.,$q_t = q_t^{inj}$) at any r. Therefore $r = r_w$ corresponds to the highest u_t, and $r = r_e$ corresponds to the lowest u_t. The mechanistic foam model allows velocity-dependent foam rheology to be calculated at three different foam states.

3.3.3. Gravity segregation of foam into gas and liquid

The models presented by Stone (1982) and Jenkins (1984) can be combined together and formulated for foam flow by introducing mobility reduction factor (MRF) for gas mobility. Then, the distance for foam to travel before gravity segregation (R_{gs}) becomes

$$R_{gs} = \sqrt{\frac{q_t}{\pi k_z(\rho_w - \rho_g)g\left(\frac{k_{rg}}{\mu_g} \times \frac{1}{MRF} + \frac{k_{rw}}{\mu_w}\right)}} \tag{3.3}$$

or,

$$R_{gs} = \sqrt{\frac{q_t}{\pi k_z(\rho_w - \rho_g)g\left[B\left(\frac{1 - S_w - S_{gr}}{1 - S_{wc} - S_{gr}}\right)^{m_2} \times \frac{1}{MRF \times \mu_g} + A\left(\frac{S_w - S_{wc}}{1 - S_{wc} - S_{gr}}\right)^{m_1} \times \frac{1}{\mu_w}\right]}} \tag{3.4}$$

in full equation. Note that q_t is total injection rate, $\mathrm{k_z}$ vertical absolute permeability, ρ_w and ρ_g water and gas densities, g gravitational acceleration, S_w average water saturation in the mixed foam region, S_{wc} and S_{gr} connate water saturation and residual gas saturation respectively, MRF is mobility reduction factor, μ_w and μ_g water and gas viscosities, A and $\mathrm{m_1}$ coefficient and exponent for Corey-type water relative permeability, and B and $\mathrm{m_2}$ coefficient and exponent for Corey-type gas relative permeability. If rock and fluid properties are available at given total injection rate, calculation of R_{gs} requires two main input parameters such as S_w and MRF in the mixed region where foam is present (see in Figure 3.1). These two parameters are constant values in the original studies of Stone's and Jenkins's for gas-water co-injection, while they are variables for foam applications as shown by the mechanistic foam model. Because multi-dimensional foam simulation in CMG-STARS also assumes constant $S_w$and MRF values, the space-averaged S_w and MRF values calculated from mechanistic foam model are used as input parameters for CMG-STARS simulations. More details on this follow below. How CMG-STARS performs foam simulation can be found in the manual (CMG 2016).

3.4. Results

For field-scale supercritical CO_2 foam propagation prediction, this study uses a hypothetical cylindrical reservoir with an injection well at the center, penetrating the entire reservoir thickness. Reservoir and operational conditions are selected similar to the Rangely Weber Sand Unit, CO (Jonas et al. 1990) where supercritical CO_2 and surfactant solutions are co-injected during field EOR tests (as shown in Table 3.3). This particular field is chosen because it is relatively homogeneous with a good reservoir thickness (H = 275 ft). Table 3.4 shows a brief summary of operational conditions in foam field EOR applications available in the literature.

Table 3.3. Rock and fluid properties of a cylindrical reservoir of interest to be tested in this study.

Reservoir Parameter	Parameter Value
Absolute permeability (md; m^2)	450; 450 $x10^{-15}$
Porosity (%)	22
Reservoir thickness (ft; m)	275; 83.8
Reservoir temperature (^oF; ^oC)	110; 43.3
Reservoir pressure (psia; Pa)	1555; $1.07x10^7$
Brine density (lb/ft^3; kg/m^3)	62.6;1002.76
Gas density (lb/ft^3; kg/m^3)	36.5;584.67
Brine viscosity (cp;Pa s)	0.65; 0.00065
Gas viscosity (cp;Pa s)	0.07;0.00007
Brine relative permeability	$0.893[(S_w - 0.42)/0.58]^{1.41}$
Gas relative permeability	$0.222[(1.0-S_w)/0.58]^{4.45}$
Total injection rate (ft^3/day;m^3/s)	17970;0.00589

Table 3.4. Examples of foam field EOR tests in the literature with operation conditions.

Field	Foam Type	Injection Pressure (psia; Pa)	Foam Quality (%)	Pattern Spacing (acre; m^2)	Injection Intervals (ft; m)
Siggins, IL	N_2	430; 2.97×10^6	99	2.5; 10117	44;13.4
Wilmington, CA	N_2,CO_2	1300; 8.96×10^6	90	-	70;21.3
Rock Creek, VA	CO_2	1000; 6.90×10^6	80	19.65; 79520	24.6;7.5
Rangely, CO	CO_2	3942; 2.72×10^7	78	20; 80937	275;83.8
North Ward Estes, TX	CO_2	1600-1800; $1.1\text{-}1.24 \times 10^7$	-	20; 80937	60;18.3
EVGSAU, NM	CO_2	-	80	38, 80; 153781,323749	20-50; 6.1,15.2
East Mallet, TX	CO_2	-	60 - 80	20, 40; 80937,161874	-
McElmo Creek, UT	CO_2	-	-	160;647497	-
Salt Creek, WY	CO_2	1600; 1.1×10^7 (THP)*	80 - 85	15.3;61916	70-80; 21.3,24.4
Delhi, LA	CO_2	1800; 1.24×10^7 (THP)*	70 - 94	40;161874	100;30.5

* THP: tubing head pressure

3.4.1. Propagation distance based on conversion from strong-foam to weak-foam state ($\mathbf{R_{csw}}$)

How far the fine-textured strong foam injected at the center propagates into the reservoir before it converts into weak foam is evaluated at three different values of mobilization pressure gradient (∇P_o=1.0, 5.0, and 30.0 psi/ft).

The first step is to make a fit to experimental data showing three foam states and two flow regimes of strong-foam state (not shown; see Izadi and Kam (2018) for more). Figure 3.3 shows the results of pressure gradient (∇P) as a function of total velocity (u_t) at ∇P_o=1.0, 5.0, and 30.0 psi/ft at $f_g^{in} = 70\%$. For ∇P_o= 5.0, and 30.0 psi/ft, the S-shaped curve folding back and forth showing three foam states are shown clearly (eg. ∇P < 25.0 psi/ft for weak foam state, 25.0 psi/ft < ∇P < 30.0 psi/ft for intermediate state, and ∇P > 30.0 psi/ft for strong foam state for ∇P_o= 30.0 psi/ft). The fact that the curve does not fold back and forth at low ∇P_o looks interesting. In such a case, there is a smooth transition from weak-foam to strong-foam state without intermediate state as shown in the case of ∇P_o= 1.0 psi/ft. By using the results in Figure 3.3 and reservoir properties in Table 3.3 for a hypothetical cylindrical reservoir, Figures 3.4 through 3.6 show how MRF and S_w values are distributed as a function of radial distance (r) for ∇P_o=30.0, 5.0, and 1.0 psi/ft, respectively. These figures show the steady-state results when foam is injected into the cylindrical reservoir at q_t^{in} = 17,970 ft3/day at a pre-specified f_g^{in}, ranging from 60% (i.e., wet foam) to 99 % (i.e., dry foam). Note that q_t is identical at any r (i.e.,$q_t = q_t^{inj}$) due to incompressible gas and liquid phases, and thus f_g is assumed to be identical at any radial

and vertical locations (i.e. $f_g = f_g^{in}$). The threshold foam quality separating the high-quality regime from the low-quality regime (f_g^*) is slightly greater than 70%.

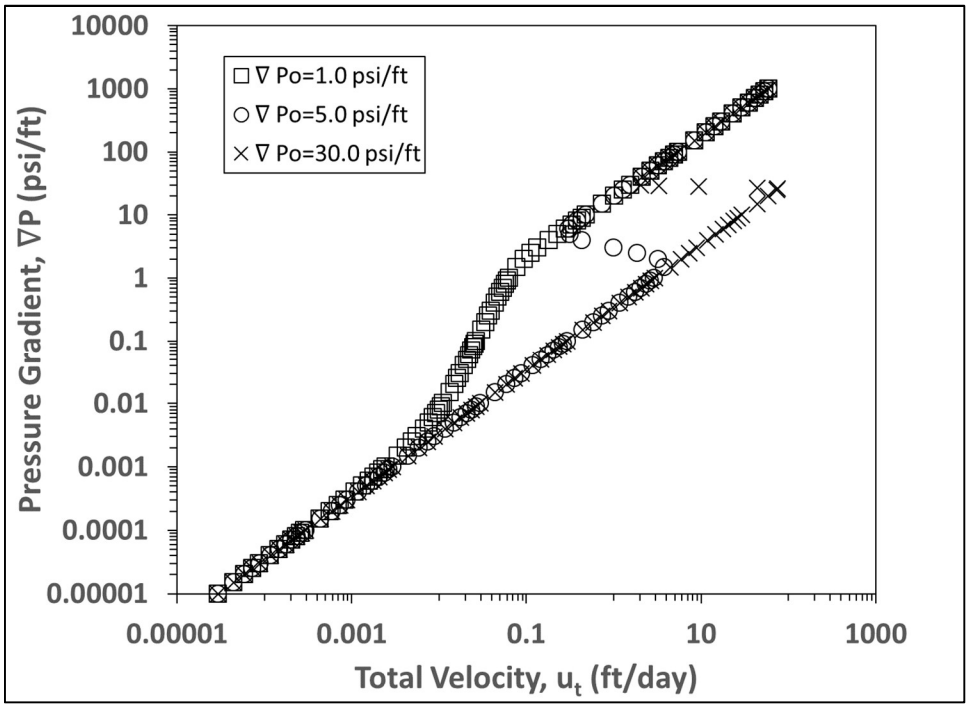

Figure 3.3. Foam flow characteristics showing three foam states (strong-foam, weak-foam, and intermediate state) at the mobilization pressure gradient (∇P_o) of 1.0, 5.0, and 30.0 psi/ft (injection foam quality (f_g^{in}) = 70%).

Figures 3.4(a) and 3.4(b) show the steady-state response of mobility reduction factor (MRF) and water saturation (S_w) as a function of radial distance (r) when ∇P_o= 30.0 psi/ft. The results show folding curves that are consistent with three foam states. Strong foam that is injected at the center of the cylindrical reservoir propagates further out up to the

point where the curves fold back, beyond which the strong foam turns into weak foam. This point, as described in Figure 3.2, is called R_{csw}. For example, for $f_g = 60$ %, MRF remains high (between 200 and 300) and S_w remains low (between 43 and 44 %), which is a typical response for strong foam, until $r = R_{csw}$ (about 5.5 ft). For $r > R_{csw}$, MRF remains low and S_w remains high, which is a typical response for weak foam. The portion of the curves folding back (representing the intermediate state) and the weak-foam portion of the curves for $r < R_{csw}$ do not appear explicitly, because they are hidden solutions (Gauglitz et al. 2002). Similar aspects are shown in Figures. 3.5(a) and 3.5(b) when ∇P_o= 5.0 psi/ft with R_{csw} about 39.7 ft.

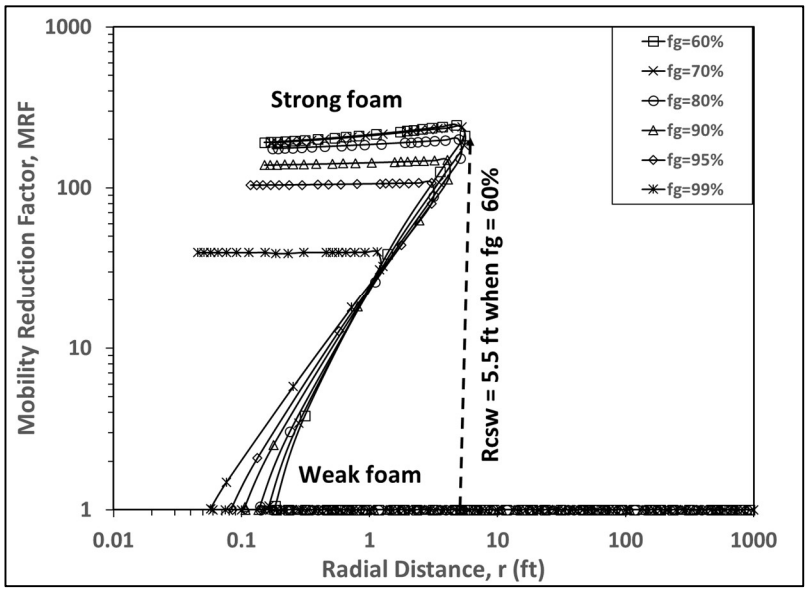

(a)

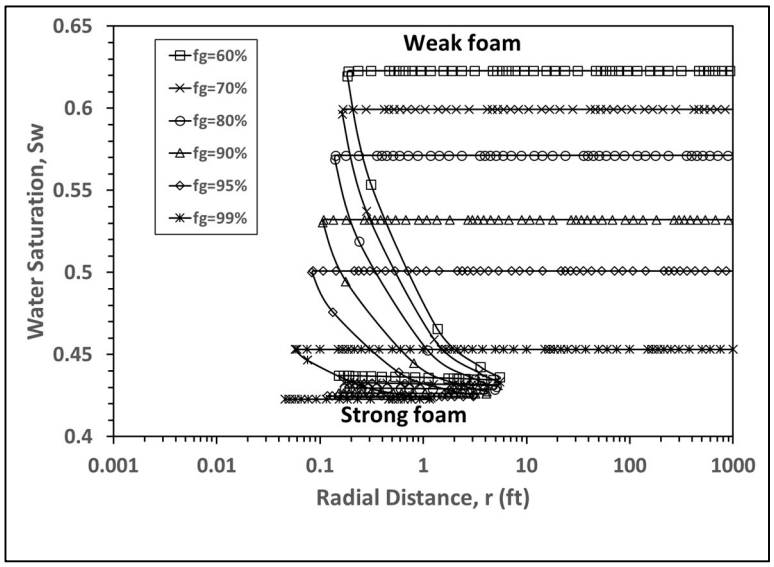

(b)

Figure 3.4. Results showing foam propagation distance for strong foam to convert into weak foam (R_{csw}) (q_t^{in} = 17,970 ft3/day in a range of f_g^{in}) at the mobilization pressure gradient (∇P_o) of 30.0 psi/ft: (a) MRF vs. radial distance and (b) S_w vs. radial distance.

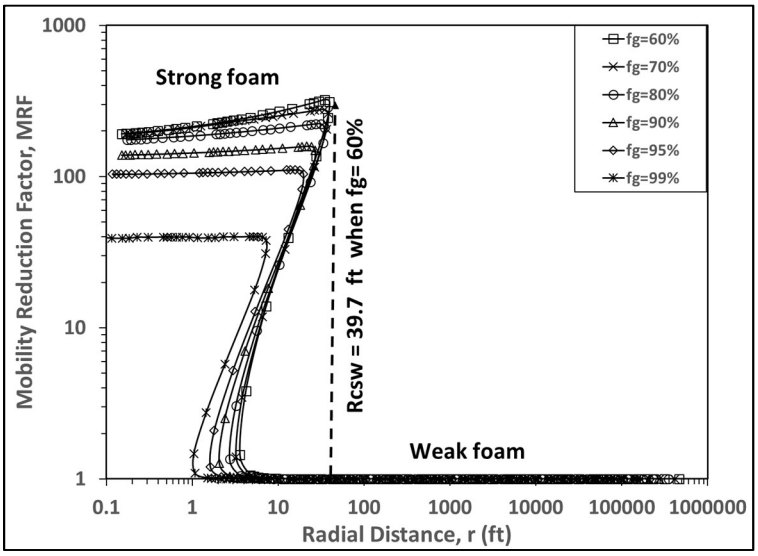

(a)

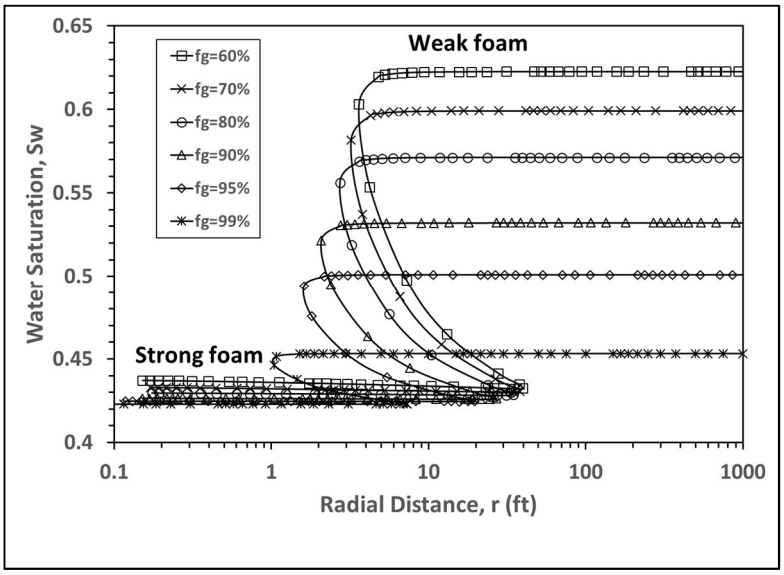

(b)

Figure 3.5. Results showing foam propagation distance for strong foam to convert into weak foam (R_{csw}) (q_t^{in} = 17,970 ft3/day in a range of f_g^{in}) at the mobilization pressure gradient (∇P_o) of 5.0 psi/ft: (a) MRF vs. radial distance and (b) S_w vs. radial distance.

A couple of interesting observations can be made in Figures 3.4 and 3.5 that investigate a range of f_g at q_t^{in} = 17,970 ft^3/day and H = 275 ft. First, the cases of ∇P_o= 30.0 and 5 psi/ft allow foam propagation distance of only about 5.5 and 39.7 ft, respectively, which seems to be unacceptable in most EOR field applications. Second, thinking of the fact that q_t^{in} is proportional to "H x R_{csw}", this could be translated into 55 and 397 ft (or, R_{csw} 10 times higher) if the reservoir thickness were 27.5 ft (or, H 10 times lower), which then becomes quite acceptable. Last, for strong foams in the low-quality regime (f_g = 60 and 70%) at $r < R_{csw}$, MRF values are comparable and R_{csw} values are almost the same. On the contrary, for strong foams in the high-quality regime (f_g = 80, 90, 95 and 99%) at $r < R_{csw}$, both MRF and R_{csw} values decrease sensitively as foam becomes drier. This demonstrates the importance of injection foam quality: (i) propagation of dry foam becomes increasingly more difficult with increasing foam quality and (ii) even when relatively wet foam is required for propagation of stable foams, there is not much benefit of going below f_g^*. The former is because of foam instability at high foam quality, and the latter is because of foam texture near its maximum if the condition falls in the low-quality regime. Figures 3.6(a) and 3.6(b) show the steady-state response of mobility reduction factor (MRF) and water saturation (S_w) as a function of radial distance (r) when ∇P_o= 1.0 psi/ft. The results do not show the intermediate state in this case; rather, in both MRF and S_w plots, the transition from the strong foam to weak foam takes place progressively with radial distance.

One complication with low ∇P_o is that there is no clear cut for R_{csw} because the curve does not fold back. Thus, R_{csw} is evaluated in two different ways in such a case: (i) R_{csw} determined based on the maximum MRF and (ii) R_{csw} determined based on a pre-specified MRF value that is still meaningful in the field applications (MRF = 10 seems to serve as a reasonable target as chosen by this study). Of course, the former (cut-off based on maximum MRF) provides much more conservative R_{csw} values than the latter (cut-off based on MRF=10). Note that the former (cut-off based on maximum MRF) is in some sense consistent with the earlier examples with folding-back curves (Figures 3.4 and 3.5), but the latter (cut-off based on MRF=10) seems more reasonable way to account for the benefits of lower ∇P_o (One may choose MRF value other than 10 such as 20 or 50, but the major findings remain the same).

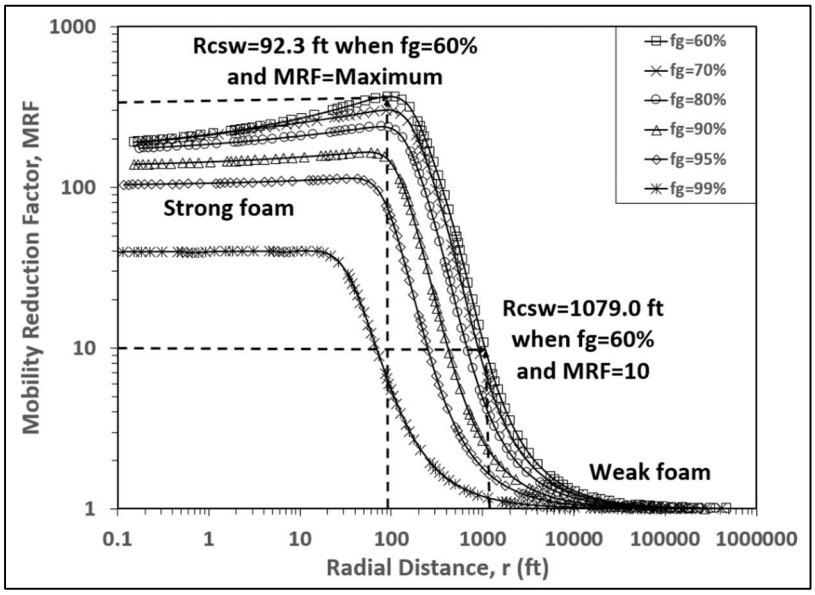

(a)

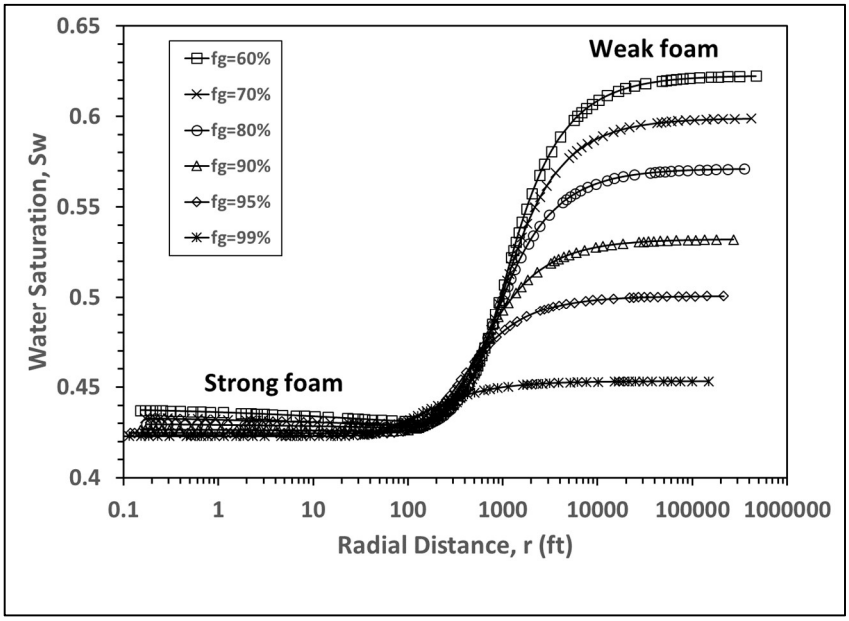

(b)

Figure 3.6. Results showing foam propagation distance for strong foam to convert into weak foam (R_{csw}) (q_t^{in}= 17,970 ft3/day in a range of f_g^{in}) at the mobilization pressure gradient (∇P_o) of 1.0 psi/ft: (a) MRF vs. radial distance and (b) S_w vs. radial distance.

An example is shown in Figure 3.6(a) where two horizontal lines determine two different cut-off points, and therefore two different R_{csw} values. For f_g = 60%, the cut-off based on maximum MRF gives R_{csw} = 92.3 ft, while the cut-off based on MRF=10 gives R_{csw} = 1079.0 ft. This proves the benefit of injecting CO_2 with low ∇P_o values – that way, supercritical CO_2 foam can travel a quite significant distance before turning into weak foam. Except f_g = 99%, all other foam qualities ranging from 60 to 90% allow stable foam to propagate as much as hundreds or thousands of feet easily, if MRF=10 is used as a cut-off line. Once the results similar to Figures 3.4 through 3.6 are constructed, the use of contour plot offers a convenient means to predict how far strong foam propagates before turning into weak foam (R_{csw}) as a function of total injection rate and injection foam quality. Such a contour plot, shown in Figures 3.7 through 3.10, is especially helpful to guide field implementation of foam EOR processes (These contours are constructed based on the calculated values at the positions specified by blue open circles (Figures 3.7 through 3.10)). Note that R_{csw} values in these plots are for the reservoir thickness (H) of 275 ft – for other reservoir thickness, the new propagation distance then becomes (H x R_{csw})/h, h being the new thickness of interest, at given q_t^{in} and f_g^{in}.

Figures 3.7 and 3.8 show the contours of propagation distance (R_{csw}) at ∇P_o= 30.0 and 5.0 psi/ft, respectively. The contour plots show the values of R_{csw} in [ft] at different combinations of q_t^{in} and f_g^{in} (H = 275 ft). The results show that one can make strong foam propagate more, by using higher q_t^{in} if f_g^{in} is fixed, or lower f_g^{in} if q_t^{in} is fixed. The sensitivity of R_{csw} to f_g^{in} at given q_t^{in} becomes more significant as foam becomes drier in general,

while such a tendency is negligible when foam is wet enough, especially $f_g^{in} < f_g^*$ (i.e., foams in the low-quality regime (f_g^*=70%)). Figures 3.9 and 3.10 show the contours of propagation distance (R_{csw}) at ∇P_o= 1.0 psi/ft, using the cut-off based on maximum MRF and MRF = 10, respectively. The same trend as shown in Figures 3.7 and 3.8 is observed. As discussed earlier, the use of CO_2 foams with lower ∇P_o (see Equation 3.1) seems much more advantageous when it comes to foam placement deep in the reservoir.

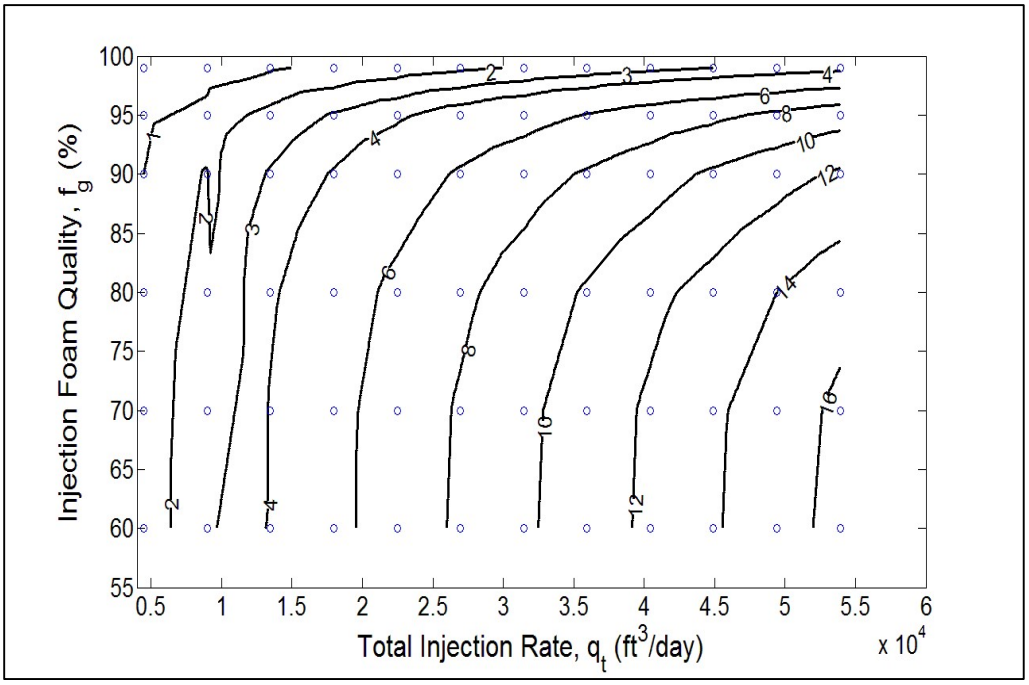

Figure 3.7. Contour plot of strong-foam propagation distance (ft) before turning into weak foam (R_{csw}) based on bubble population balance model at the mobilization pressure gradient (∇P_o) of 30.0 psi/ft (reservoir thickness (H) = 275 ft).

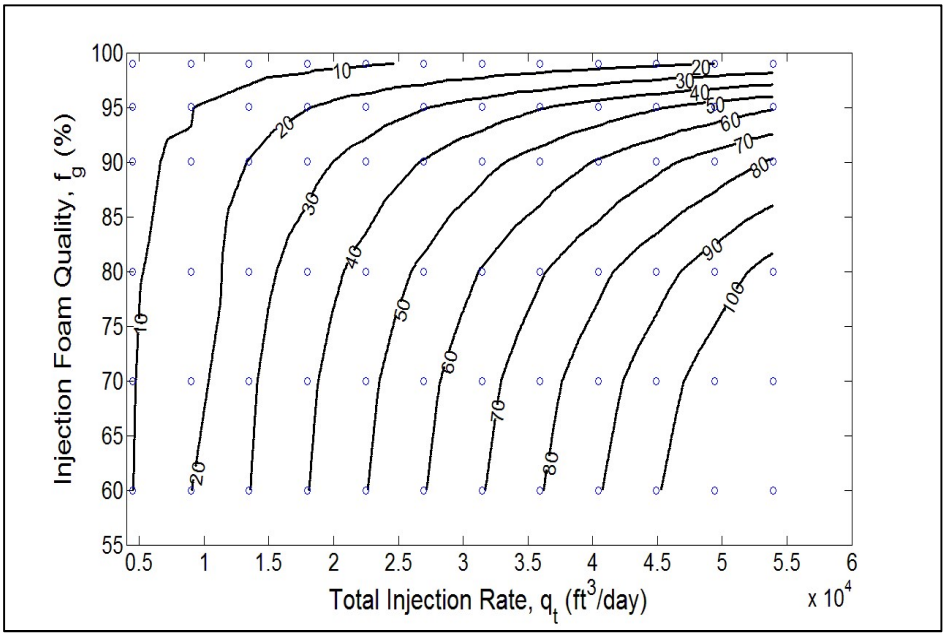

Figure 3.8. Contour plot of strong-foam propagation distance (ft) before turning into weak foam (R_{csw}) based on bubble population balance model at the mobilization pressure gradient (∇P_o) of 5.0 psi/ft (reservoir thickness (H) = 275 ft).

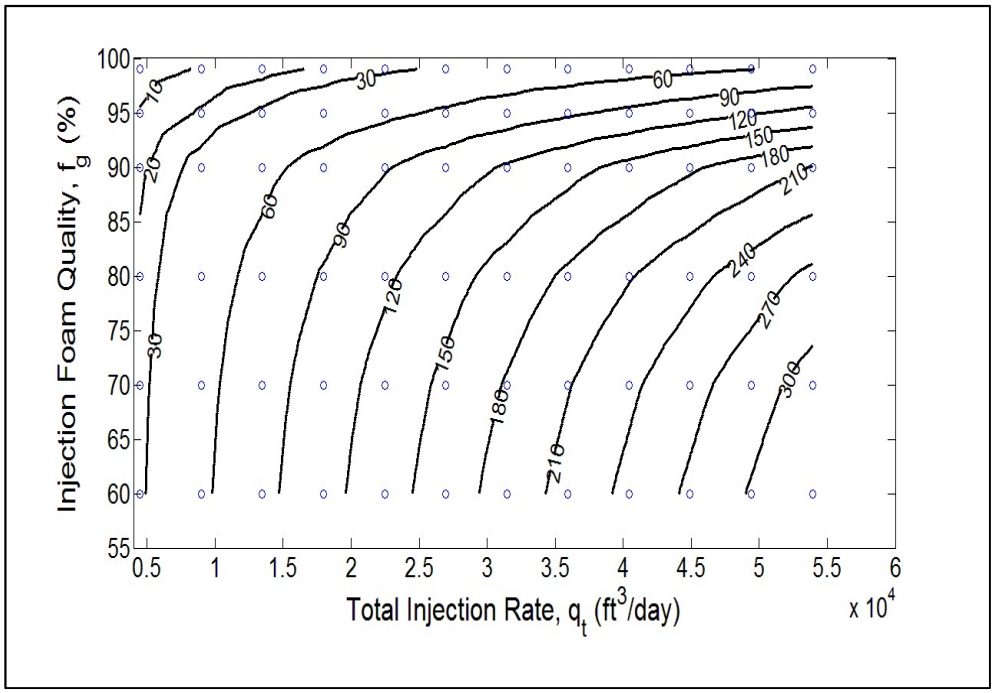

Figure 3.9. Contour plot of strong-foam propagation distance (ft) before turning into weak foam (R_{csw}) based on bubble population balance model at the mobilization pressure gradient (∇P_o) of 1.0 psi/ft (reservoir thickness (H) = 275 ft): cut-off based on maximum MRF.

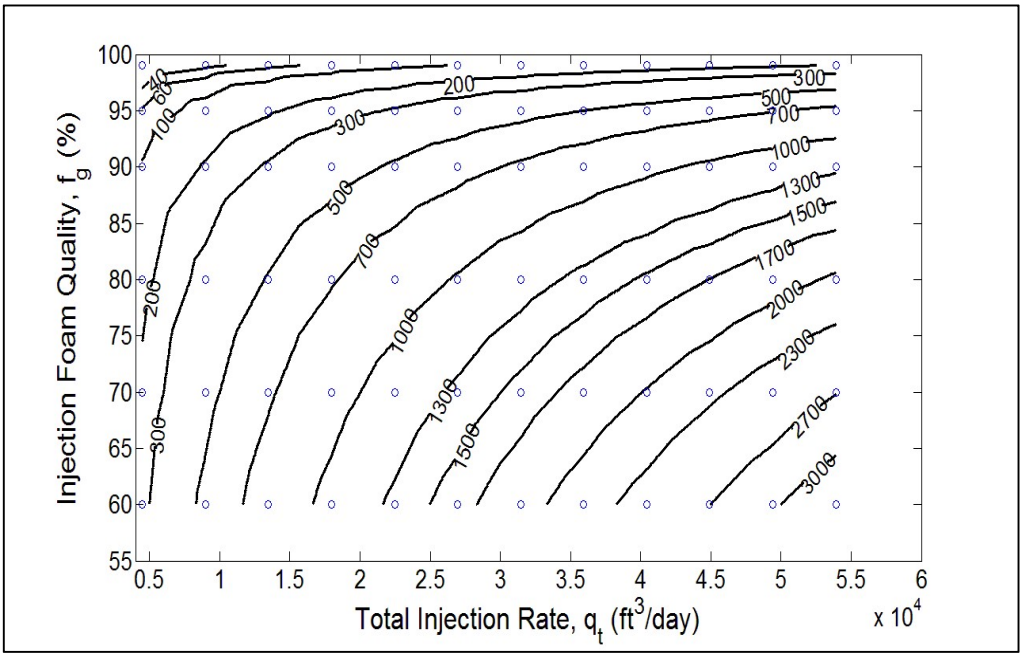

Figure 3.10. Contour plot of strong-foam propagation distance (ft) before turning into weak foam (R_{csw}) based on bubble population balance model at the mobilization pressure gradient (∇P_o) of 1.0 psi/ft (reservoir thickness (H) = 275 ft): cut-off based on MRF = 10.

3.4.2. Propagation distance based on gravity segregation (R_{gs})

In addition to the conversion to weak foam, foam propagation is also limited by gravity segregation. This section deals with how to determine the distance before foam segregates into gas and liquid (R_{gs}) in two different methods: Stone and Jenkins model and CMG-STARS simulation. The former is a simplified approach assuming fixed values of reservoir and fluid properties, and the latter is more realistic, but complicated, approach accounting for those properties as a function of pressure, temperature, and radial and vertical locations. To evaluate R_{gs}, the same cylindrical reservoir is selected as shown in the previous section (Table 3.3). Because both methods assume a fixed and constant value of MRF in the mixed region (even though it is not true physically as shown in Figures

3.4 through 3.6), the results from the mechanistic foam modelling in the previous section are used as input parameters. More specifically, for the mixed region properties, the Stone and Jenkins model uses the maximum MRF value (see Figures 3.4(a) through 3.6(a)) and its corresponding S_w value (see Figures 3.4(b) through 3.6(b)) to determine R_{gs}. This means, for example, MRF = 240 for ∇P_o= 30.0 psi/ft, MRF = 278 for ∇P_o= 5.0 psi/ft, and MRF = 303 for ∇P_o= 1.0 psi/ft, when f_g^{in} = 70%, while MRF = 149 for ∇P_o= 30.0 psi/ft, MRF = 158 for ∇P_o= 5.0 psi/ft, and MRF = 165 for ∇P_o= 1.0 psi/ft, when f_g^{in} = 90% (q_t^{in} remains the same at 17,970 ft3/day). In CMG-STARS simulations, R_{gs} is determined by using these MRF values but letting S_w values be calculated by the simulator. These S_w values calculated by the simulator are essentially the same as those S_w values used for input in the Stone and Jenkins model in Figures 3.4(b) through 3.6(b).

Figures 3.11 through 3.13 show the results of CMG-STARS simulations to evaluate the cases of ∇P_o = 30.0, 5.0, and 1.0 psi/ft, respectively, at f_g^{in} = 70 and 90% (q_t^{in} = 17,970 ft3/day). In all cases, the reservoir has wellbore radius (r_w) of 0.42 ft, radial distance to the reservoir boundary (r_e) of 1000.0 ft, and reservoir thickness of 275.0 ft. Gas and surfactant solutions, which create strong foam inside the well, are co-injected at the total injection rate (q_t^{in}) of 17,970 ft3/day into the reservoir initially saturated with water. The two injection foam qualities (f_g^{in}), 70% and 90%, are chosen to represent wet-foam and dry-foam scenarios (or, foams in the low-quality regime and in the high-quality regime) respectively. These results are based on 4,000 days of foam injection, which is shown to be (near) steady-state results after some trial-and-error simulations. Additional input

parameters specific to CMG-STARS for this simulation task are shown in Table 3.5 (See CMG (2016) for more details on these parameters).

Table 3.4. Additional foam simulation parameters required by CMG-STARS for gravity-segregation simulation (See CMG (2016) for more details).

Parameter	Value	Parameter	Value
FMSURF	1.4389 X 10^{-5}	EPOIL	0
FMCAP	0	EPGCP	0
FMOIL	0	SFDRY*	0.425-0.441
FLOIL	0	SFBET	600
FMGCP	0	SFSURF	0
FMMOB*	174	EFSURF	0
EPSURF	4	SFCAP	0
EPCAP	0	EFCAP	0

* Values from mechanistic modelling in the previous section (Figures 3.4 through 3.6)

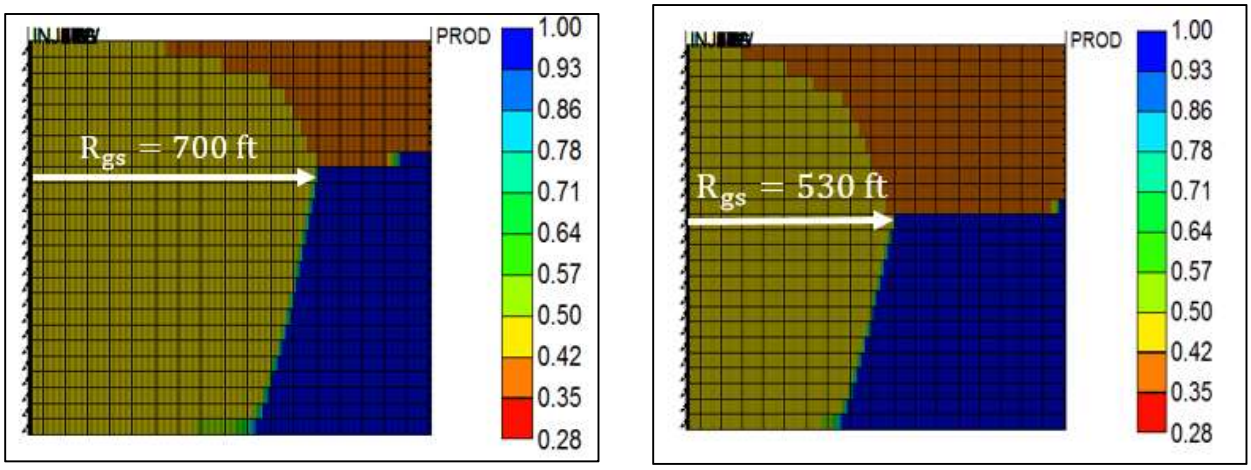

(a) (b)

Figure 3.11. Simulation results showing foam propagation distance before gravity segregation (R_{gs}) when the mobilization pressure gradient (∇P_o) is 30.0 psi/ft: (a) f_g^{in} = 70% at MRF=240 and (b) f_g^{in} = 90% at MRF=149 (Stone and Jenkins model predicts R_{gs} = 801 and 701 ft respectively).

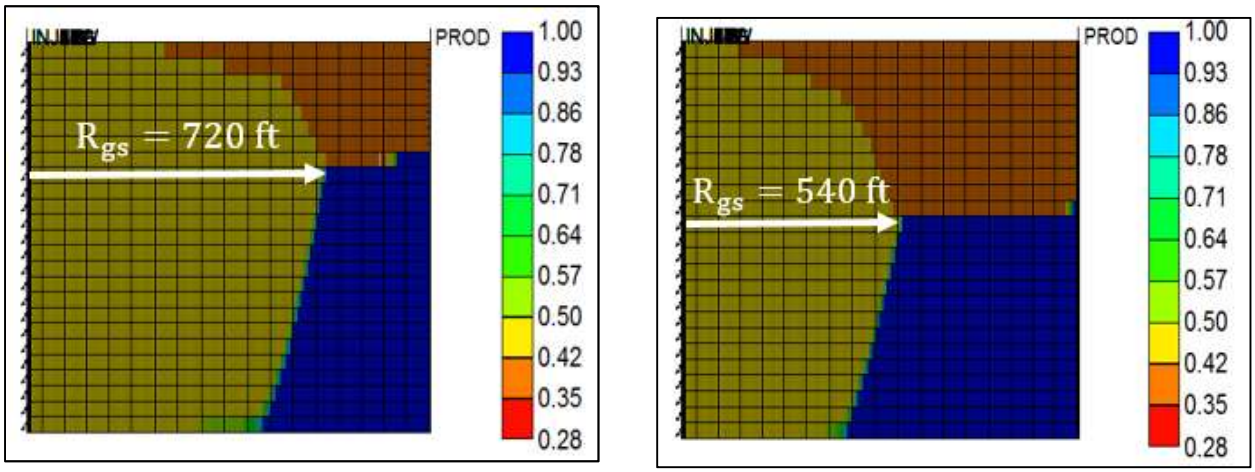

(a) (b)

Figure 3.12. Simulation results showing foam propagation distance before gravity segregation (R_{gs}) when the mobilization pressure gradient (∇P_o) is 5.0 psi/ft: (a) f_g^{in} = 70% at MRF=278 and (b) f_g^{in} = 90% at MRF=158 (Stone and Jenkins model predicts R_{gs} = 858 and 720 ft, respectively).

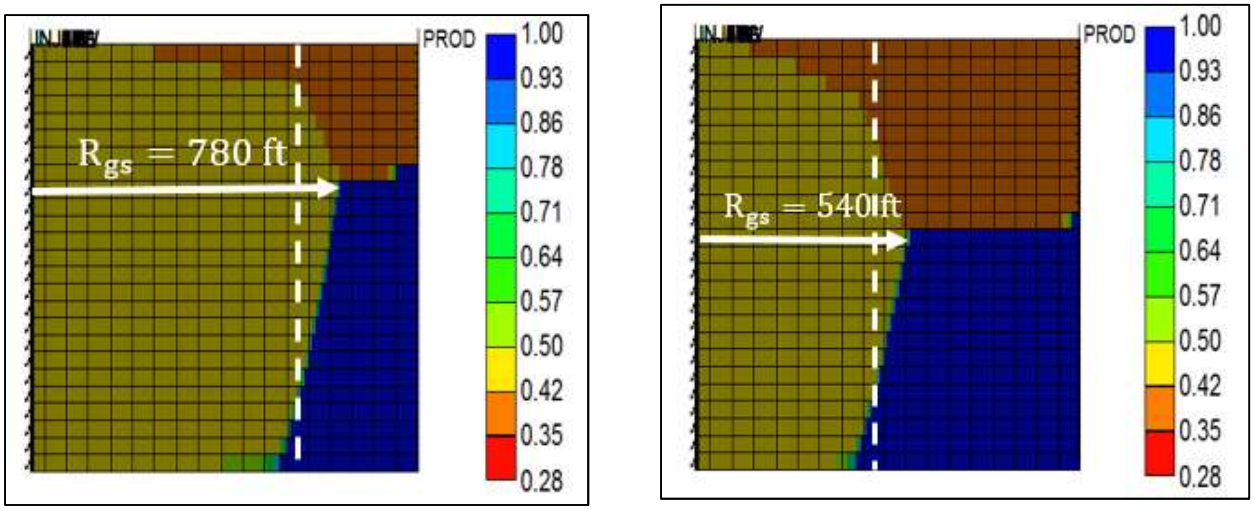

(a) (b)

Figure 3.13. Simulation results showing foam propagation distance before gravity segregation (R_{gs}) when the mobilization pressure gradient (∇P_o) is 1.0 psi/ft (cut-off based on maximum MRF): (a) f_g^{in} = 70% at MRF=303 and (b) f_g^{in} = 90% at MRF=165 (Stone and Jenkins model predicts R_{gs} = 884 and 734 ft, respectively).

Figure 3.11 shows simulation results in terms of the steady-state water saturation for ∇P_o = 30.0 psi/ft. When the injection foam qualities (f_g^{in}) are 70% (Figure 3.11(a)) and 90% (Figure 3.11(b)), the corresponding MRF values are about 240 and 149 (see Figure 3.4(a)), with R_{gs} from simulations leading to 700 and 530 ft, respectively. Drawing horizontal lines from the injection well to the contact point of the three regions, the water saturations in the mixed region are 0.430 and 0.426 in Figure 3.11(a) and 3.11(b), respectively. For the same case, the Stone and Jenkins model predicts R_{gs} values of 801 and 701 ft for f_g^{in} = 70% and 90%, respectively. Although there is some difference, the results are comparable showing the same trend. It is believed that the difference is caused by multiple aspects including changes in fluid properties (density, viscosity, compressibility, etc.) as well as simulation artifacts at the injection and production wells (fluid redistribution at the inlet face, capillary end effect, etc.), and as a result the simulation slightly underpredicts R_{gs} compared to the Stone and Jenkins model. Figure 3.12 shows similar simulation results for ∇P_o = 5.0 psi/ft. For the injection foam qualities (f_g^{in}) of 70% (Figure 3.12(a)) and 90% (Figure 3.12(b)), the corresponding MRF values are 278 and 158 (see Figure 3.5(a)), the S_w values are 0.430 and 0.426, and the R_{gs} values are 720 and 540 ft, respectively. The Stone and Jenkin's model predicts R_{gs} of 858 and 720 ft. Once again, the trend is well captured, and the simulation predicts somewhat lower R_{gs} values compared to the Stone and Jenkin's model.

Figure 3.13 shows the steady-state simulation results for ∇P_o = 1.0 psi/ft with the cut-off based on maximum MRF. For the injection foam qualities (f_g^{in}) of 70% (Figure

3.13(a)) and 90% (Figure 3.13(b)), the corresponding MRF values are 303 and 165 (see Figure 3.6(a)), the S_w values are 0.429 and 0.426, and the R_{gs} values are 780 and 540 ft, respectively. The Stone and Jenkin's model predicts R_{gs} of 884 and 734 ft. The results are consistent with other cases. Figure 3.14 shows simulation results for ∇P_o = 1.0 psi/ft with the cut-off based on MRF=10. This situation is somewhat tricky, because the mechanistic modeling results in Figure 3.6(a) show that the MRF values are mostly much greater than 10 for the region occupied by strong foams. Even so, it is believed to provide a useful insight when compared with Figure 3.13. For the injection foam qualities (f_g^{in}) of 70% (Figure 3.14(a)) and 90% (Figure 3.14(b)) both with MRF = 10, the simulation shows the S_w values of 0.494 and 0.456, and the R_{gs} values of 185 and 175 ft, respectively. The Stone and Jenkin's model predicts R_{gs} of 211 and 204 ft. These R_{gs} values in Figure 3.14 are less than those in Figure 3.13, because the use of smaller MRF (i.e., MRF = 10 in Figure 3.14) provides lower pressure gradient (∇P), resulting in lower R_{gs}.

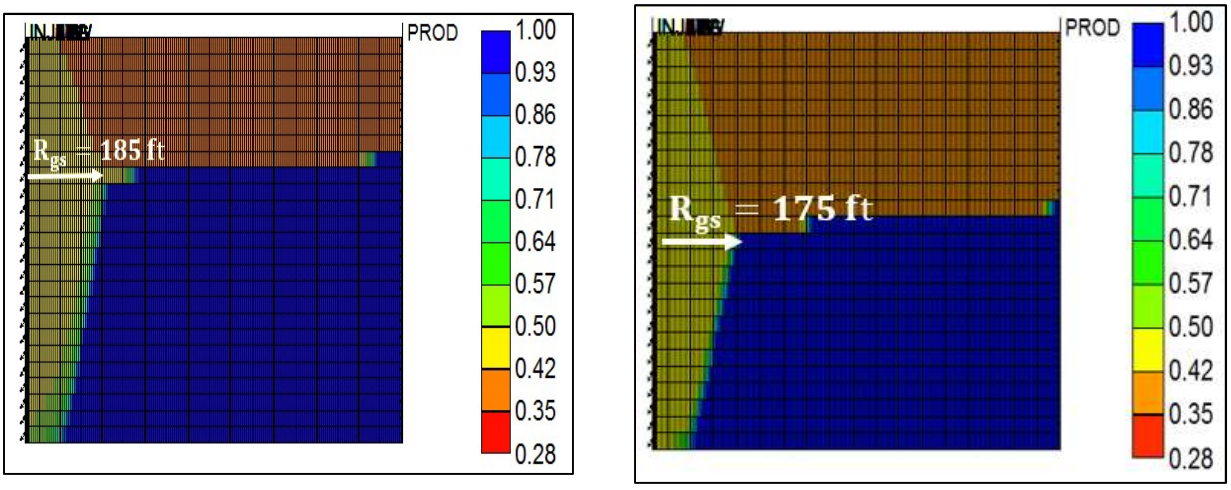

(a) (b)

Figure 3.14. Simulation results showing foam propagation distance before gravity segregation (R_{gs}) when the mobilization pressure gradient (∇P_o) is 1.0 psi/ft (cut-off based on MRF=10): (a) f_g^{in} = 70% at MRF=10 and (b) f_g^{in} = 90% at MRF=10 (Stone and Jenkins model predicts R_{gs} = 211 and 204 ft, respectively).

In order to verify the assumption of constant water saturation in the three constant regions in the Stone and Jenkins model, scanning the saturation map in vertical and horizontal directions works as a convenient means. As shown in each of Figures 3.13(a) and 3.13(b), one horizontal line through the contact point of three regions (not shown, but the same as the horizontal arrows shown) and the other vertical line somewhat before the contact point, where r < R_{gs}, are selected as an example. Figure 3.15 shows the change in water saturation along the vertical and horizontal scanning lines (shown in Figure 3.13) from the simulations. It clearly shows three different constant state regions – the gas override region where S_w is near S_{wc}, the water underride region where S_w is near $1 - S_{gr}$, and the mixed region in between with foams at its steady-state S_w that matches with MRF values from mechanistic model.

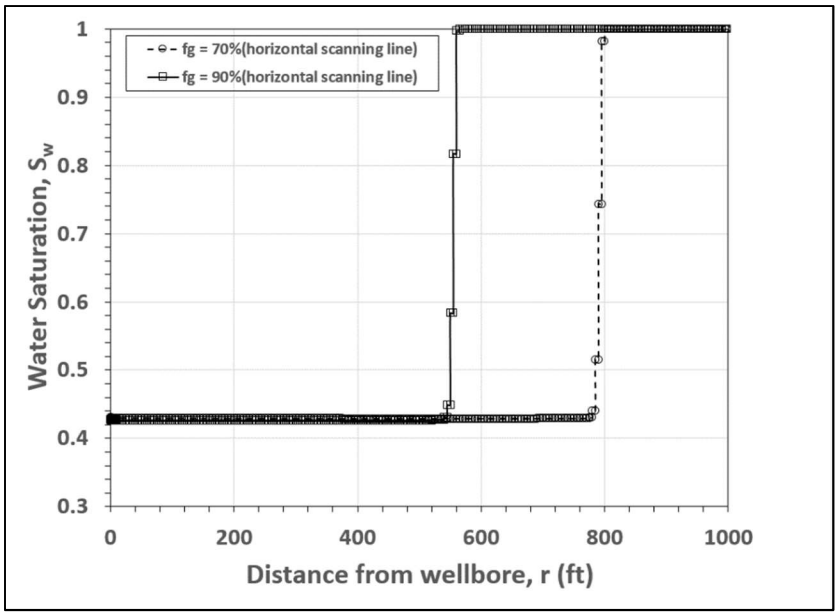

(a)

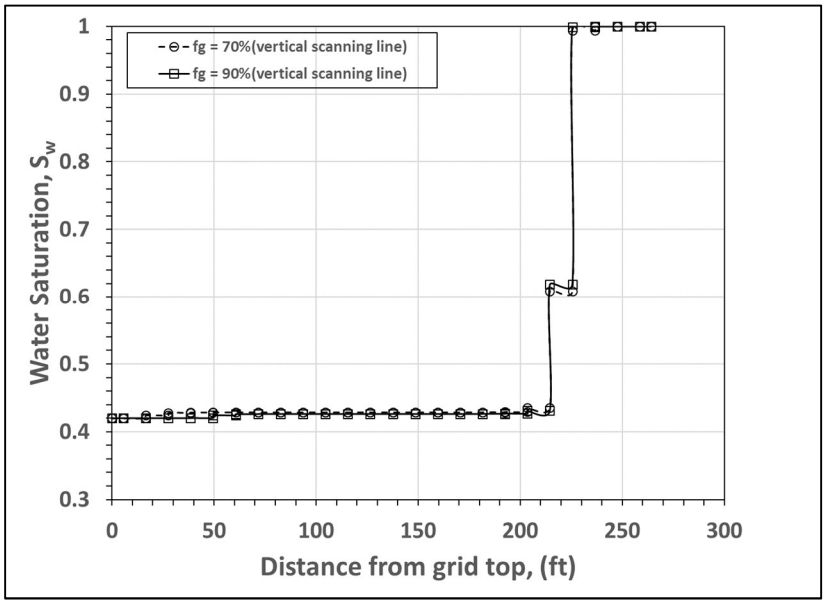

(b)

Figure 3.15. Steady-state water saturation profiles along the scanning lines (horizontal (a), vertical (b)) in Figure 3.13 from gravity-segregation simulations showing three constant regions as approximated by Stone and Jenkins model (1982,1984).

Figure 3.16 shows the pressure profiles for the same scanning lines as shown in Figure 3.13. The pressure decreases sharply along the horizontal scanning line up to r = R_{gs} because of high MRF value in the presence of foams, followed by mild change to the outlet because of single-phase flow of water. The pressure profile along the vertical direction follows hydrostatic pressure gradient concept (higher hydrostatic pressure gradient in the underride region, and lower hydrostatic pressure gradient in the override and mixed foam regions). Figure 3.17 shows how the bottomhole injection pressure changes for those examples shown in Figures. 3.15 and 3.16, until it reaches 4,000 days of foam injection that is believed to be at, or close to, the steady state after some trial-and-error simulations. In both cases, the Injection pressure rapidly increases with time in the beginning as strong foam enters, and then levels off gradually as the system approaches the steady state. The cases with higher MRF have higher injection pressures. Note that the outlet back pressure is 1555.0 psia. Similar to R_{csw} contours in Figures 3.7 through 3.10, the results from the Stone and Jenkins model for R_{gs} can be plotted as a function q_t^{in} and f_g^{in} as well. Figures 3.18 through 3.21 show how far foam propagates before gravity segregation (R_{gs}) when the MRF values are borrowed from the mechanistic foam model for ∇P_o = 30.0, 5.0, and 1.0 (cut-off based on maximum MRF and cut-off based on MRF = 10) psi/ft (Figures 3.7 through 3.10), respectively. It is interesting to find that R_{gs} is also very sensitive to f_g^{in}, i.e., it is becoming increasingly difficult to make drier foams propagate deep into the reservoir, while such a sensitivity is much less for relatively wet foams. Similar to R_{csw} contours, R_{gs} contours also show longer propagation distance at high injection rate (or higher injection pressure, equivalently).

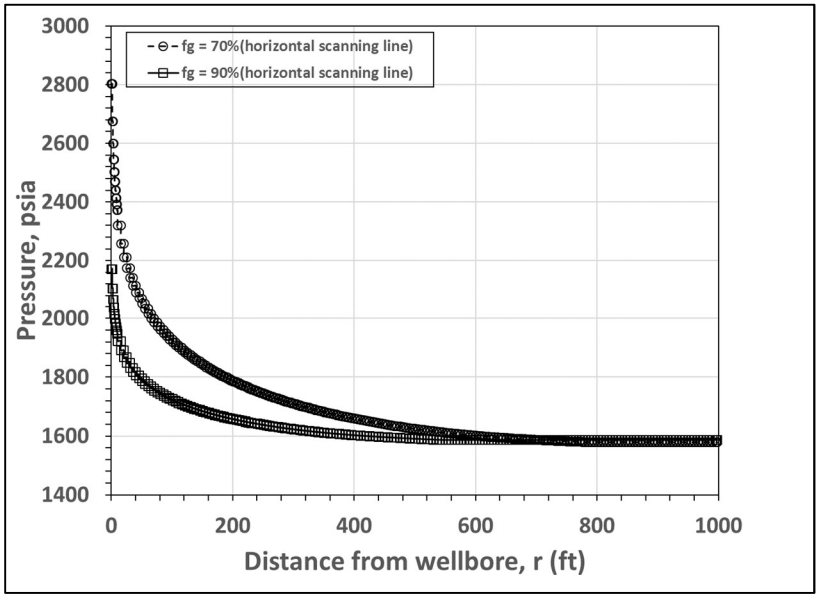

(a)

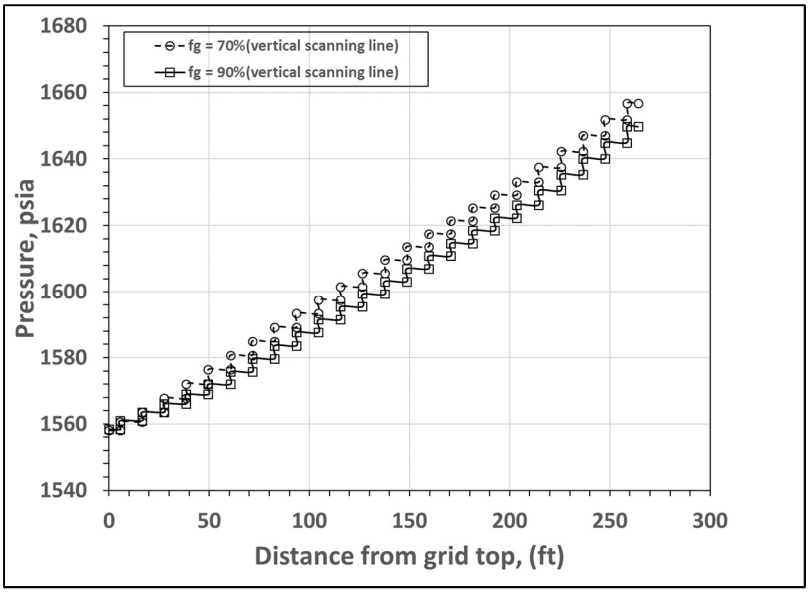

(b)

Figure 3.16. Steady-state pressure profiles along the scanning lines (horizontal (a), vertical (b)) in Figure 3.13 from gravity-segregation simulations showing three constant regions as approximated by Stone and Jenkins model (1982,1984).

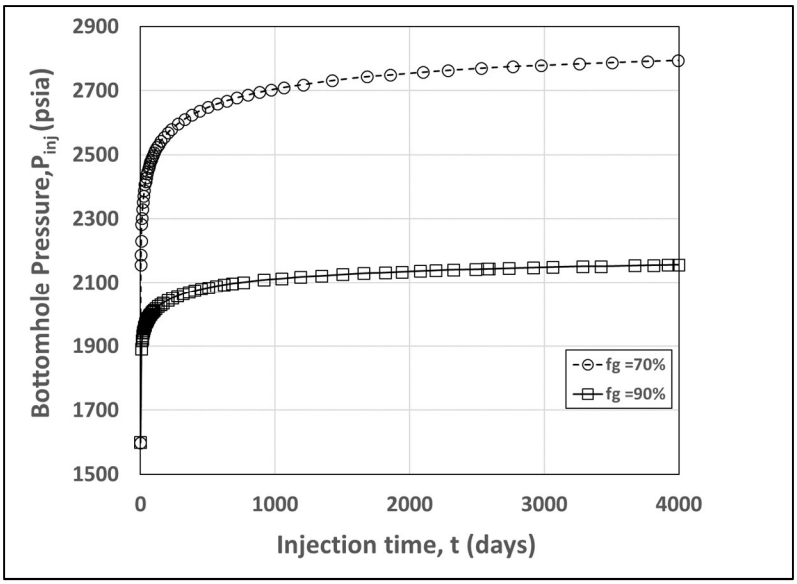

Figure 3.17. Change in bottomhole injection pressure with time simulated by CMG-STARS to reach (close to) the steady state at 4000 days of foam injection.

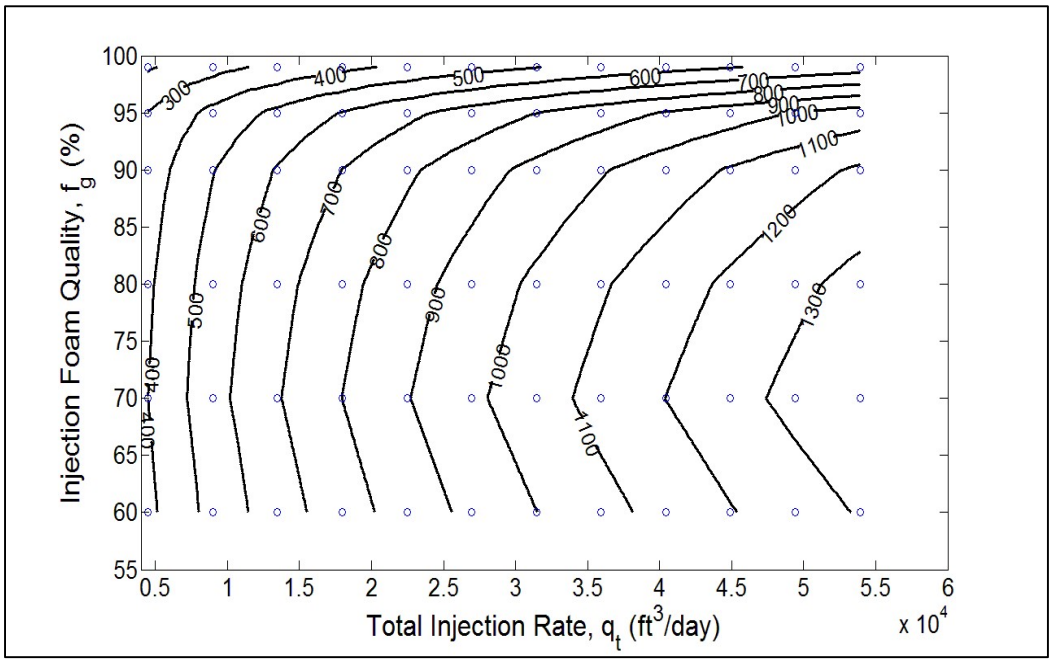

Figure 3.18. Contour plot of foam propagation distance (ft) before gravity segregation (R_{gs}) based on Stone and Jenkins model (MRF taken from mechanistic foam model at the mobilization pressure gradient (∇P_o) of 30.0 psi/ft).

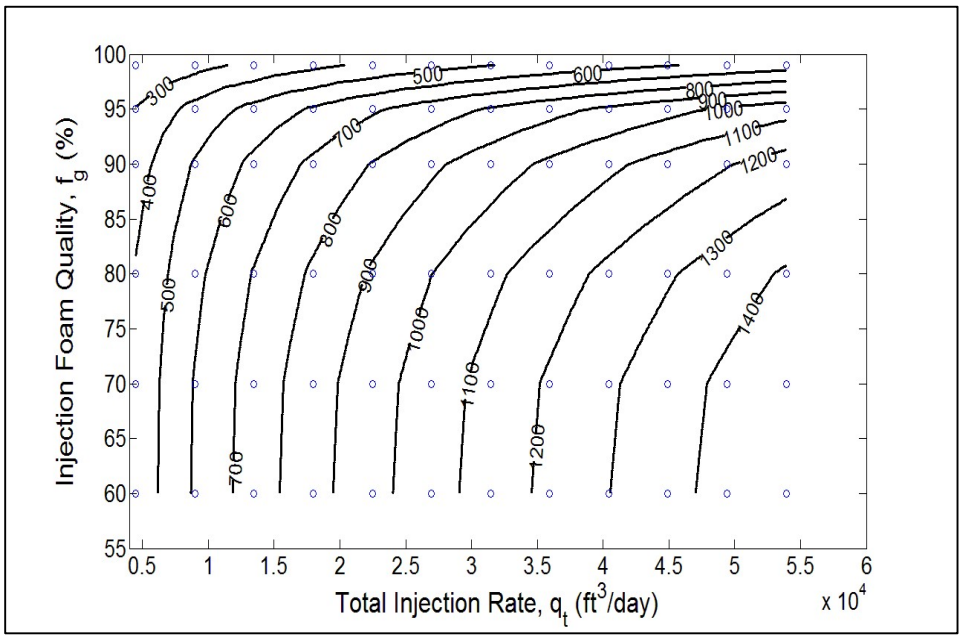

Figure 3.19. Contour plot of foam propagation distance (ft) before gravity segregation (R_{gs}) based on Stone and Jenkins model (MRF taken from mechanistic foam model at the mobilization pressure gradient (∇P_o) of 5.0 psi/ft).

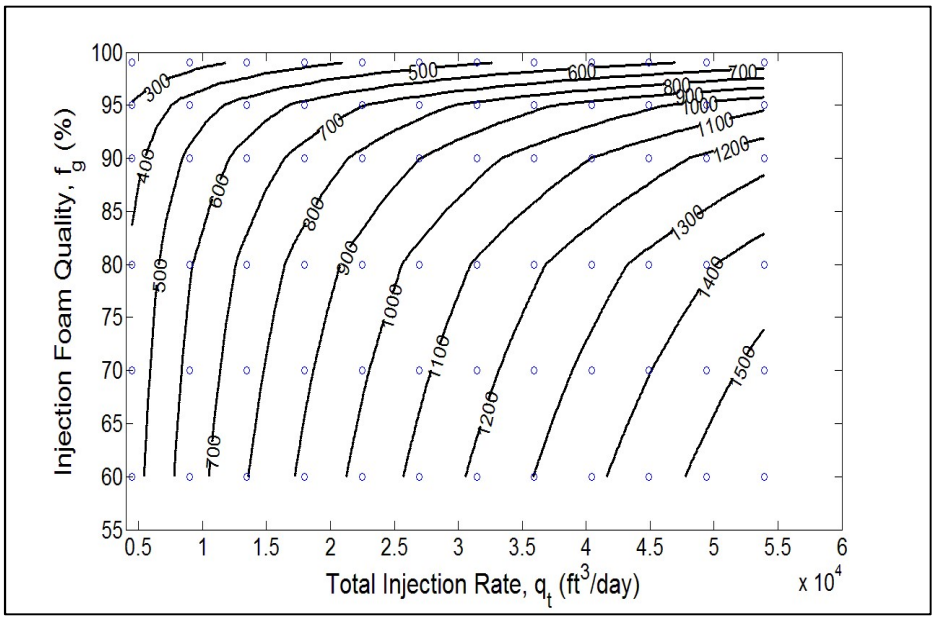

Figure 3.20. Contour plot of foam propagation distance (ft) before gravity segregation (R_{gs}) based on Stone and Jenkins model (MRF taken from mechanistic foam model at the mobilization pressure gradient (∇P_o) of 1.0 psi/ft (cut-off based on maximum MRF)).

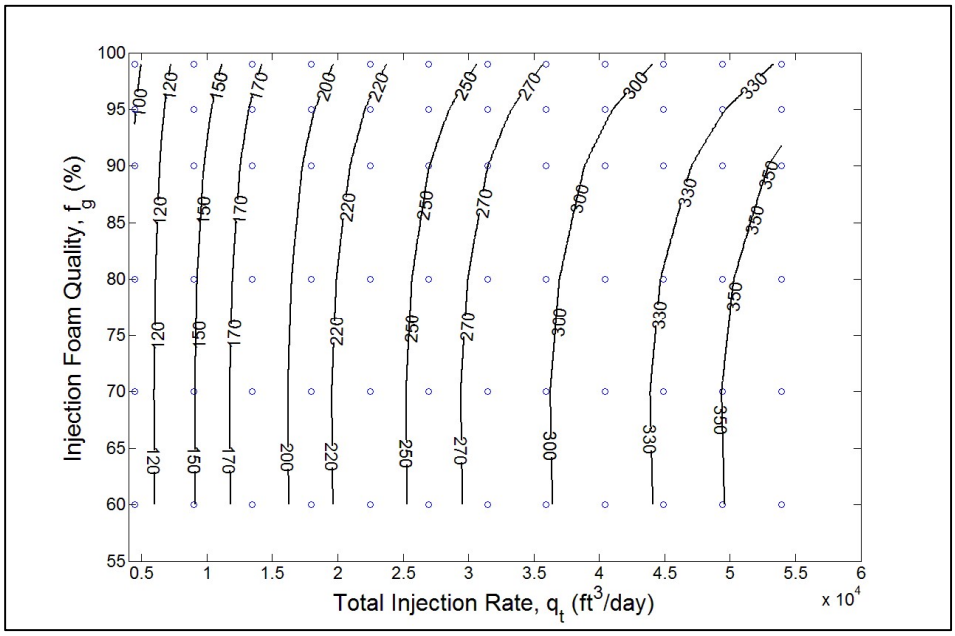

Figure 3.21. Contour plot of foam propagation distance (ft) before gravity segregation (R_{gs}) based on Stone and Jenkins model (MRF taken from mechanistic foam model at the mobilization pressure gradient (∇P_o) of 1.0 psi/ft (cut-off based on MRF = 10).

3.4.3. Combined results and discussions

The two mechanisms that limit foam propagation in the field-scale foam EOR can be analyzed together based on the results given in the previous sections. Figures 3.22 and 3.23 show such results at the injection foam qualities (f_g^{in}) of 70% and 90%, respectively, for ∇P_o = 30.0, 5.0, and 1.0 as well as ∇P_o = 0.1 psi/ft. Note that when ∇P_o is low (1.0 and 0.1 psi/ft), both results from the cut-off line based on maximum MRF as well as MRF = 10 are used. Note in such cases that the results at MRF = 10 overpredicts R_{csw} compared to maximum MRF (see Figure 3.6), while the results at MRF = 10 underpredicts R_{gs} compared to maximum MRF because of lower lateral pressure gradient (see Figures 3.20 and 3.21). Both figures show that there is a threshold value

(or, range) of ∇P_o, below which foam propagation is limited by gravity segregation (R_{gs}) and above which foam propagation is limited by the conversion of strong foam to weak foam (R_{csw}). Because of relatively steep slope in R_{csw} curve, foam injection conditions at lower ∇P_o (i.e., left-hand side of the figure) have advantages in placing foams deep into the reservoir. Foam propagation distance is less sensitive to ∇P_o at lower ∇P_o, while foam propagation distance can still be improved significantly by making ∇P_o lower at higher ∇P_o. Comparing Figures 3.22 and 3.23, it also shows foams in the high-quality regime is more difficult to be placed deep in the reservoir than foams in the low-quality regime. Note from Equation 3.1 that lower ∇P_o translates lower interfacial tension and higher pore throat size, which can be achieved more easily at higher pressure, with better foamer, and at higher absolute permeability.

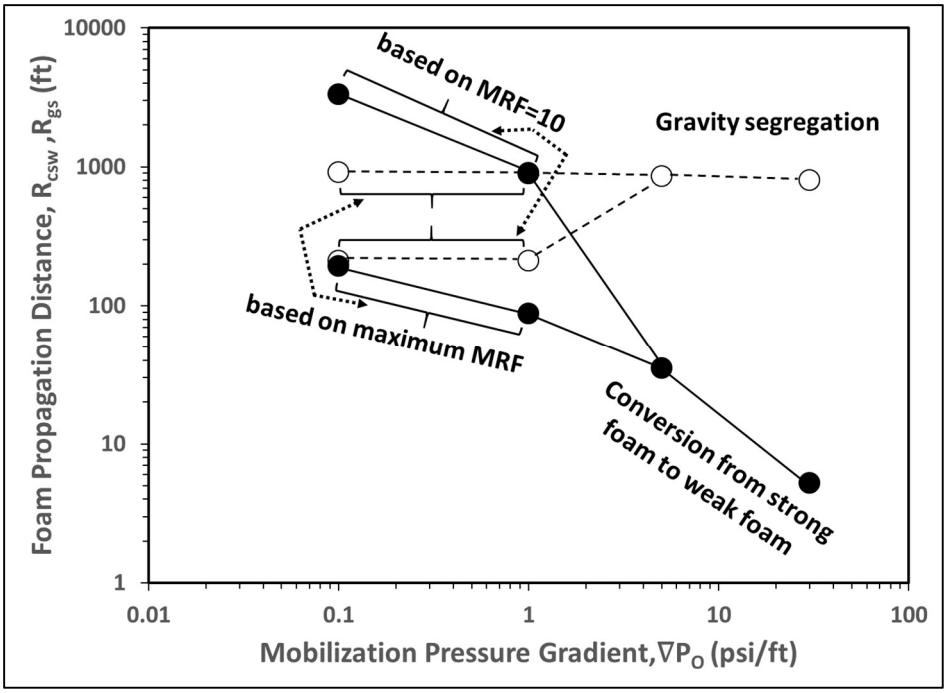

Figure 3.22. Prediction of propagation distance (ft) of 70% quality foams by combining both mechanisms (conversion to weak foam vs. gravity segregation).

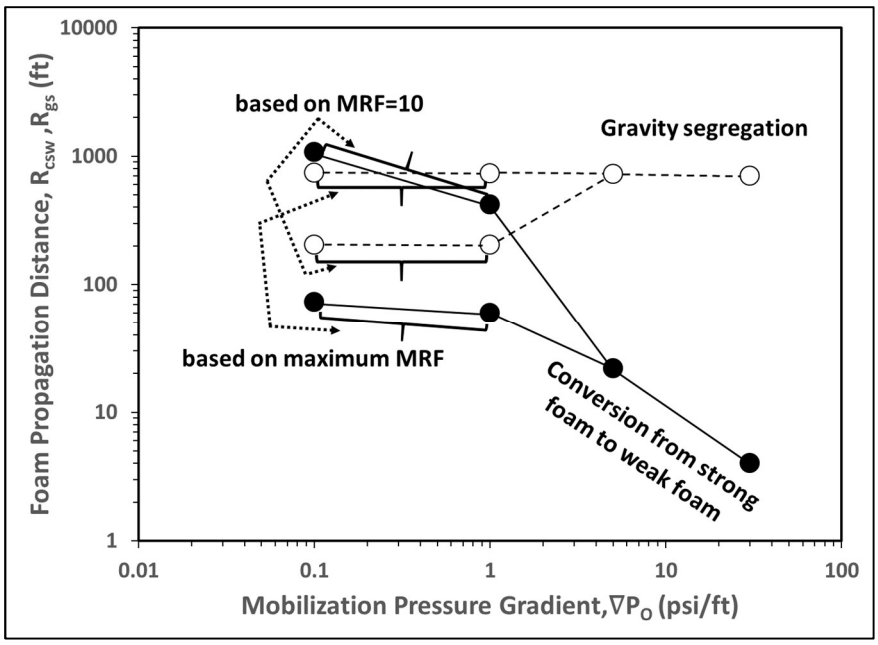

Figure 3.23. Prediction of propagation distance (ft) of 90% quality foams by combining both mechanisms (conversion to weak foam vs. gravity segregation).

This study greatly improves the prediction of R_{gs}, by using representative MRF values from mechanistic foam model. At the same time, it should be pointed out that, there still is room to improve the prediction further, because both Stone and Jenkins model and CMG simulation assume constant values of MRF as an input parameter (see Equations 3.3 and 3.4). When it comes to possible errors associated with a constant-MRF assumption, the case with lower ∇P_o (Figure 3.6) would show more errors than the case with higher ∇P_o (Figures 3.4 or 3.5), because it presents a continuous and progressive change from strong-foam to weak-foam state without showing hysteretic behaviors (i.e., multi-valued foam rheology surface that folds back and forth). A three-dimensional reservoir simulation with mechanistic modeling capability is believed to reduce the gap

essentially. Even though this study shows how foam propagates in a large system, the results are limited to homogeneous cylindrical reservoirs at the moment. In order to take the results to the real-world field cases, there are challenges to overcome, including (but not limited to) heterogeneity of the system and interaction between foams and reservoir oils. The major finding of this study, however, still holds true – foams with lower ∇P_o (e.g. supercritical CO_2 foams) are more advantageous over other gaseous foams with higher ∇P_o (e.g. foams with gas CO_2, gas N_2, hydrocarbon gas, flue gas, etc.). It should be noted that the importance of small lab-scale coreflood experiments based on the field rock and fluid samples and selected foaming agents cannot be underestimated, because they allow mechanistic model fits to recommend appropriate MRF values at different injection scenarios.

3.5. Conclusions

Foam propagation is limited in field EOR processes by two main mechanisms as investigated in this study – the first, conversion from strong-foam to weak-foam state, and the second, gravity segregation of foam into gas and liquid. Dealing with an ideal (large homogeneous cylindrical) reservoir, the results of this study can be summarized as follows:

- The population-balance foam model shows that the propagation distance before strong foam converts to weak foam (R_{csw}) primarily depends on the mobilization pressure gradient (∇P_o). This explains why foams with lower ∇P_o (e.g. supercritical CO_2 foams) can propagate much further than other gaseous foams with higher ∇P_o. The results also show theoretically why wetter foams can propagate further than drier foams, and why higher injection rates help longer propagation distance.

- CMG STARS simulation and the Stone and Jenkins model confirm that gravity segregation also limits foam propagation distance. Foam propagation distance before gravity segregation (R_{gs}) primarily depends on the mobility reduction factor (MRF) that is calibrated by mechanistic model based on fundamental foam physics in this study.

- Combining both mechanisms together, the results show that foams with lower ∇P_o tends to have gravity segregation more dominating factor for foam propagation. On the contrary, foams with higher ∇P_o tends to have the conversion to weak foam more dominating factor.

CHAPTER 4. A FIELD CASE STUDY ON THE OPTIMIZATION OF SUPERCRITICAL CO_2 FOAM EOR PROCESSES

4.1. Introduction

Enhanced oil recovery (EOR) is defined as a series of processes in which a fluid is injected into the reservoir to change either rock or fluid properties to eventually produce more oil and gas from the reservoir that otherwise would not have been produced any longer with primary depletion mechanisms (van Poollen 1980). EOR methods are considered as a useful and efficient means to produce more hydrocarbons from depleted reservoirs worldwide, by using gas injection, thermal process, and chemical flooding typically. In addition to secondary water injection, gas injection (such as N_2, CO_2, produced hydrocarbon gas, flue gas, etc., either at miscible or immiscible condition) is a common EOR method because of abundance and easy operation in the field. Water and gas injections, however, share similar limitations, that is, relatively low sweep efficiency caused by gravity segregation (either underride or override) as well as unfavorable mobility compared to reservoir oil. Such limitations result in relatively high remaining oil saturation after the treatments.

Literature review shows that significant efforts have been made to overcome poor sweep efficiency associated with water and gas injection. For example, an early study of Caudle and Dyes (1957) proposed a method that is, injecting water along with gas as a miscible slug. They found that the sweep was improved by the reduced mobility of gas phase in the presence of relatively high water saturation. Field tests of gas and water co-injection by Stone (1983) proved that injecting water alternatively with gas (or, water-

alternating gas, “WAG”) is more feasible if gas-to-water ratio and interval of each injection period are selected carefully. If achieved, the suitable injection ratio that is primarily a function of mobilities of existing fluids is shown to keep the gas zone at a constant volume between water and miscible front zones. There exist numerous WAG field tests reported in the literature (Sanchez 1999; Christensen et al. 2001; Barati Ghahfarokhi et al. 2016). Following Caudle and Dyes (1957), Blackwell et al. (1959) reported that gravity causes gas and water injected together to segregate rapidly within the reservoir. Therefore, the mobility of water or gas zone is not significantly improved. One way to mitigate gravity segregation is foaming the injected gas phase with surfactant solutions. Foam, which is a colloidal system in which gas phase is dispersed in surfactant-laden liquid phase, has liquid films (or, lamellae) that block the gas phase and thus reduce gas mobility. The mobility reduction factor (MRF) defines how much gas mobility is reduced when foam is present. Similar to water and gas injection, foam can be injected by introducing gas and surfactant solutions together (so called, “coinjection”) or surfactant solutions alternating with gas (so called “SAG”). There are numerous foam pilot tests available in the literature: CO_2/N_2 foam project consisting of eight cycles of SAG performed in Wilmington field, California (Holm and Garrison 1988); CO_2 foam field test in Rangely Weber Sand Unit in northwestern Colorado (Jonas et al. 1990) to block high permeability thief zones and keep gas production low; CO_2 foam field test conducted in Salt Creek, WY (Mukherjee et al. 2016); and SAG treatment for conformance control in Lower Mirador formation, Cusiana Field, Columbia (Ocampo et al. 2013; Rossen et al. 2017), among many. For a given foam type (CO_2, N_2, etc. together with a certain surfactant formulation and concentration),

the effects of injection pressure or total injection rate, foam quality, pattern spacing, and injection interval length are typically investigated in the design stage.

4.2. Objectives of this study

The objective of this chapter is to show how to determine the optimum injection conditions for gas-water EOR at various injection gas fraction (or foam qualities (f_g), equivalently) and total injection rates (Q_t, that is, a sum of gas and liquid rate, i.e., $Q_t = Q_g + Q_w$) with or without foams, in order to guide field development planning by using reservoir simulations performed by CMG-STARS. In addition, how such optimum conditions can shift depending on foam quality (f_g) and mobility reduction factor (MRF) is examined by using a graphical method. The field of interest is a sector in Lisama field, Colombia, with an inverted 5-spot well pattern (i.e., one injection well near the center surrounded by four production wells). A mechanistic foam model in the literature (Izadi and Kam 2018) is extended to define foam flow characteristics. It should be noted that the optimum conditions found in this study is field-specific; the systematic approaches and procedures to reach the optimum conditions are universal to any field developments, however.

4.3. Methodology

4.3.1. Field of Interest

Lisama field is located in the eastern part of the Middle Magdalena Valley Basin in Colombia (Rodriguez 2009) (Figure 4.1). It was discovered in 1935, and estimated to hold approximately 0.25 billion STB of oil in place (Jaimes et al. 2014). Lisama reservoir mainly consists of two main sandstone formations, Mugrosa and Colorado interbedded with shale streaks (Gomez et al. 2009). The fluvial system of Meandric Rivers is the environmental deposition of Lisama formations, and therefore it possesses complex channels of changing sandstone thickness and lateral and vertical changes of rock types (Sandoval et al. 2009). Production from Lisama field moves gradually from the primary to the secondary and tertiary recovery processes. Water and gas flooding techniques are expected to follow in the near future.

The sector of interest in this study has an inverted 5-spot pattern with approximately 22 acres drainage area and reservoir gross thickness of 335 ft with similar structural, and petrophysical characteristics to those of the Mugrosa formation in Lisama field. As shown in Figure 4.2, four producers (L-8, L-44, L-52, and L-56) are located at the edge of the modeled sector with an injection well located approximately in the middle (slightly closer to L-8 and L-56 by about 130 ft, compared with L-44 and L-52). The injection well is located down-dip from L-8 and up-dip from L-44, L-52, and L-56. Table 4.1 summarizes reservoir rock and fluid properties used in this study following Naranjo (2010). The pattern consists of four heterogeneous sandstone layers, each separated by thin impermeable shale streaks - the top layer (A) is 55 ft thick with a permeability

distribution ranging from 20 to 200 mD; the second layer (B), 60 ft thick from 20 to 30 md; the third layer (C), 35 ft thick from 80 to 100 md, and the fourth layer (D), 90 ft thick from 20 to 100 md.

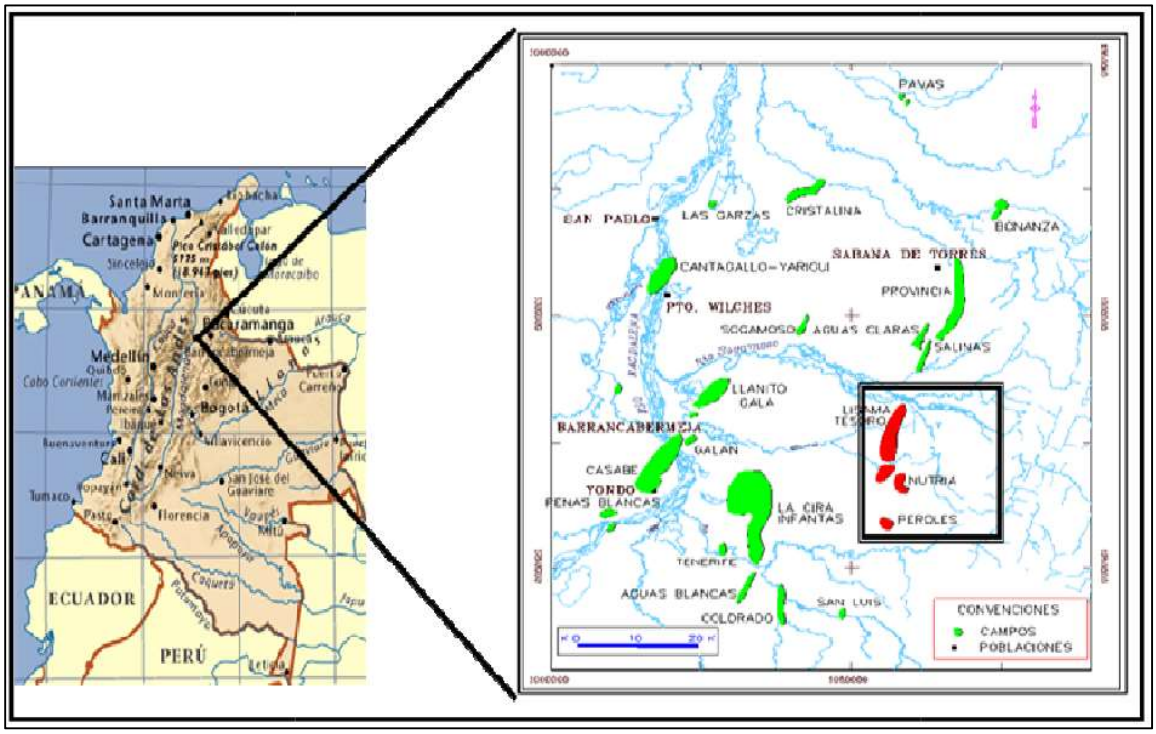

Figure 4.1. Field map of Lisama field, Colombia, investigated in this study (Rodriguez 2009).

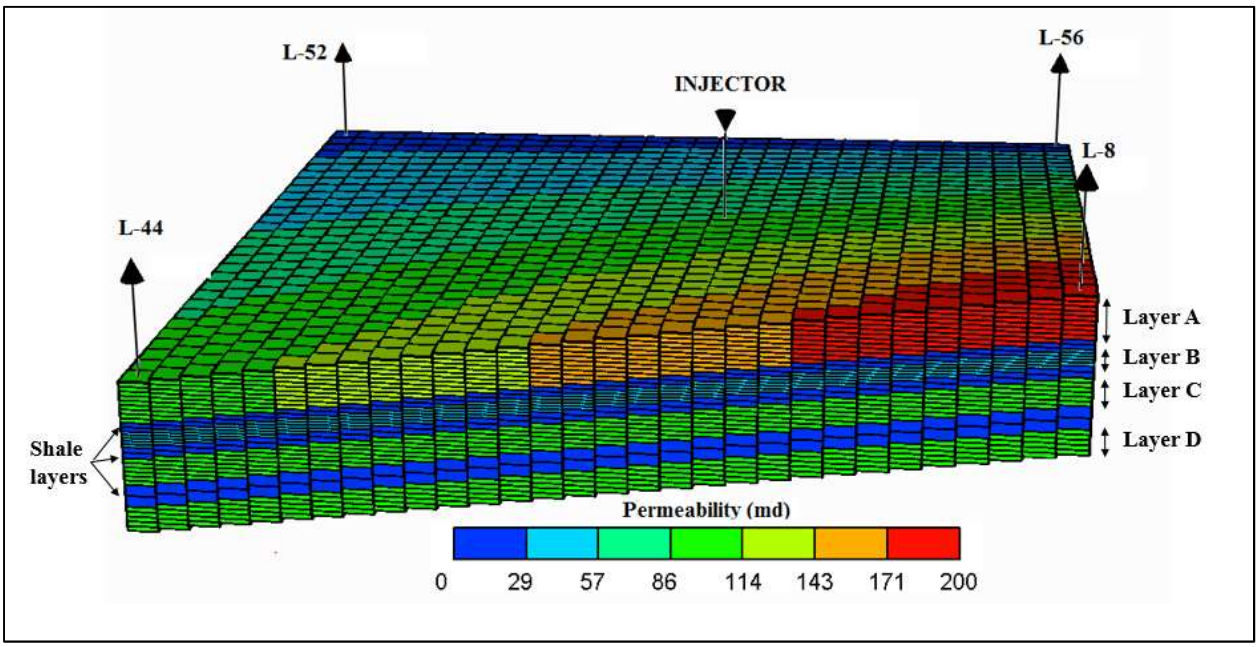

Figure 4.2. Three-dimensional grid system of a sector to be investigated in this study (Mugrosa formation in Lisama field) with permeability distribution in sandstone layers A, B, C and D isolated by impermeable shale layers.

Table 4.1. Reservoir rock and fluid properties of Mugrosa formation in Lisama field used in this study.

Reservoir pressure (psia)	2500
Reservoir temperature (°F)	140-160
Bubble point pressure (psia)	2500
Oil viscosity (cp) @ 2500 psia	1.7
Water viscosity (cp) @ 2500 psia	0.43
Average initial oil saturation (%) right before gas-liquid injection	45
Connate water saturation (%)	25
Average porosity (%)	18.5
Permeability range (md)	20-200

4.3.2. Simulation Methods

There are two main simulation approaches for foam-associated EOR processes in the literature. The first is a mechanistic modeling approach that keeps track of the change in bubble population through bubble creation, bubble coalescence, trapped gas saturation and so on, often called bubble population balance modeling (Falls et al. 1988; Kovscek and Radke 1994; Kam and Rossen 2003), while the second is based on local steady-state, or local equilibrium, foam behavior, typically incorporating a pre-determined level of mobility reduction for the gas phase (Cheng et al. 2000). The field-scale simulation in this study applies CMG STARS module by incorporating MRF (the second approach), while the selection of MRF at different f_g and Q_t is based on the mechanistic modelling (the first approach).

Reservoir simulations are based on the conservation of mass and heat. The equation of continuity for a multi-component system takes the transport for each component in each phase into account. For an isothermal three-component system of oil, water, and gas, the equation of continuity is defined as follows for component i (Klins 1984), if chemical reactions, dispersion, and adsorption on the rock surface are negligible:

$$-\vec{\nabla}.\sum_{i=1}^{N_c}\left(\rho_o\omega_{io}\vec{u}_o+\rho_g\omega_{ig}\vec{u}_g+\rho_w\omega_{iw}\vec{u}_w\right)=\frac{\partial}{\partial t}\left(\emptyset S_o\rho_o\omega_{io}+\emptyset S_g\rho_g\omega_{ig}+\emptyset S_w\rho_w\omega_{iw}\right) \quad (4.1)$$

Note that ρ_j is the density of phase j (j = o, w, and g for oil, water and gas phases respectively), ω_{ij} the mass fraction of component i in phase j, $\vec{u}_j$ the velocity of phase j, $\emptyset$

the porosity of the medium, and S_j the saturation of phase j. For fluid flow in porous media, the transport equation is represented by Darcy's equation, i.e.

$$\vec{u}_j = -\frac{kk_{rj}}{\mu_j}\left(\nabla p_j - \gamma_j \nabla z\right) \tag{4.2}$$

where, k is the absolute permeability of medium, k_{rj} the relative permeability to phase j, μ_j the viscosity of phase j, ∇p_j the pressure gradient of phase j, and $\gamma_j \nabla z$ the gravity potential for dipping strata for phase j. CMG STARS foam model modifies gas phase mobility by reducing gas relative permeability (k_{rg}), the degree of which is specified by MRF (CMG 2016; CMG STARS uses the term FM to represent MRF). Therefore, the gas relative permeability in presence of foam (k_{rg}^f) is defined as

$$k_{rg}^f = k_{rg}(S_w) \times MRF^{-1} \tag{4.3}$$

The 5-spot sector model of this study for Lisama field is discretized using Cartesian center-point variable-depth/variable-thickness gridding system (Figure 4.2). There are 30 grid blocks in each of x and y directions, and 31 blocks in z direction. As a result, each grid block is about 66.7 ft wide in x and y directions and 7 to 11 ft thick in z direction. All wells are fully penetrating the sandstone layers, and shale streaks are not perforated, unless otherwise noted.This study considers three total injection rates (Q_t) (Q_t = 23,358, 46,717, and 70,075 ft^3/day for low, intermediate, and high Q_t values, respectively), at various f_g values (from f_g = 100 % (meaning only gas injection) to f_g = 0 % (meaning only

liquid injection)). The values of MRF=1, 10,100, and 1000 represent the cases with no foam (simply gas and water coinjection), low-strength, intermediate-strength and high-strength foam, respectively.

4.4. Results

A total of 132 scenarios (i.e., $3Q_t$, $11f_g$, and 4 MRF values) are simulated at first assuming completely impermeable shales between layers, while additional follow-up scenarios are evaluated allowing a limited level of transmissibility through shales. The results are evaluated in terms of cumulative oil recovery and sweep efficiency after 20 years of injection. Each scenario has the same initial condition, that is, the remaining oil saturation (S_o) of 0.45 at the end of the primary depletion, the detailed condition of which is shown in Table 4.1. Simulation details are in the following sections categorized in terms of total injection rate (Q_t).

4.4.1. Intermediate injection rate (Q_t = 46,717 ft^3/day; base case)

The simulation results are summarized in Tables 4.2 for MRF = 1, 10,100, and 1000 respectively, showing the 20-year cumulative oil recovery and sweep efficiency in a wide range of injection gas fractions.

Table 4.2. Summary of simulation results for the base case (intermediate) injection rate (Q_t = 46,717 ft^3/day) after 20 years.

f_g (%)	Cumulative recovery (Mstb)				Sweep efficiency* (%)			
	MRF=1	MRF=10	MRF=100	MRF=1000	MRF=1	MRF=10	MRF=100	MRF=1000
100	3,263	3,263	3,263	3,263	22.4	22.4	22.4	22.4
90	4,277	4,323	4,783	4,961	29.3	29.6	32.7	33.9
80	4,773	4,867	5,518	6,067	32.7	33.3	37.8	41.5
70	5,015	5,125	5,789	6,767	34.4	35.1	39.6	46.3
60	5,169	5,260	5,902	7,382	35.4	36.0	40.4	50.5
50	5,287	5,359	5,970	7,811	36.2	36.7	40.9	53.5
40	5,393	5,451	6,005	7,994	36.9	37.3	41.1	54.7
30	54,95	5,536	5,994	7,851	37.6	37.9	41.0	53.7
20	5,666	5,624	5,937	7,350	38.8	38.5	40.6	50.3
10	5,697	5,711	5,837	6,627	39.0	39.1	39.9	45.4
0	5,745	5,745	5,745	5,745	39.3	39.3	39.3	39.3

(*Sweep efficiency is defined as ([the change in average oil saturation during gas and liquid injection (ΔS_o)] / [the average oil saturation at the beginning of gas-liquid injection (S_o)]) x 100

When MRF =1 and 1000, for example, Figures 4.3 and 4.4 show the distribution of oil saturation along multiple cross-sectional areas of the sector after 20-year injection at the injection gas fraction (f_g) of 90% and 50%, respectively, which represent relatively dry and wet injection conditions. Figures 4.5 and 4.6 show the daily oil, gas, and water production rates at f_g = 90% and 50% respectively.

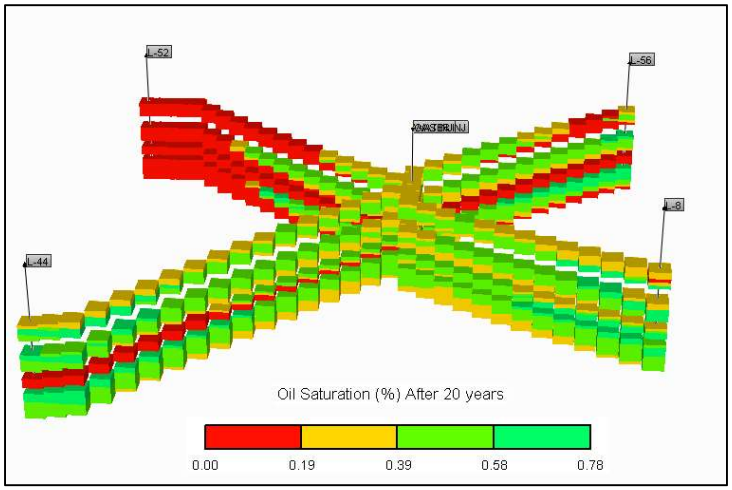

(a)

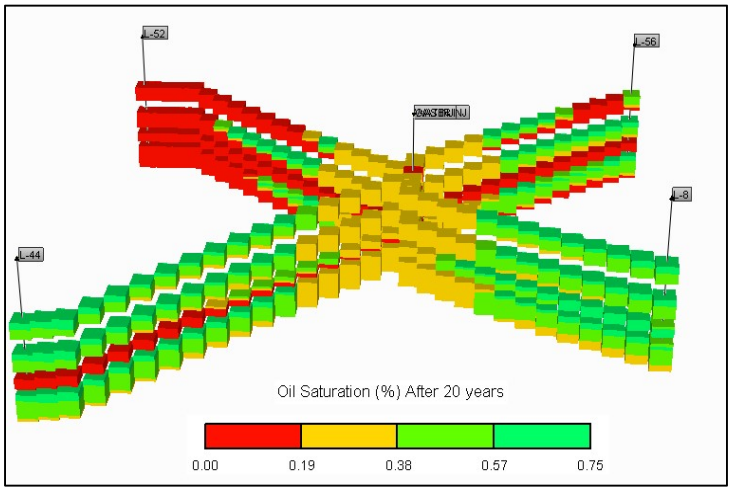

(b)

Figure 4.3. Cross-sectional map showing oil saturation distribution after 20 years for base case (intermediate) total rate (Q_t = 46,717 ft^3/day) at dry injection condition (f_g =90%): (a) no foam (MRF=1) and (b) high-strength foam (MRF=1000).

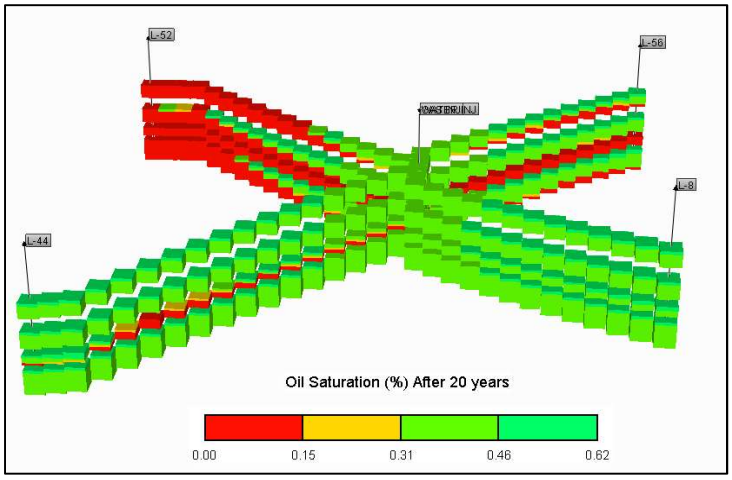

(a)

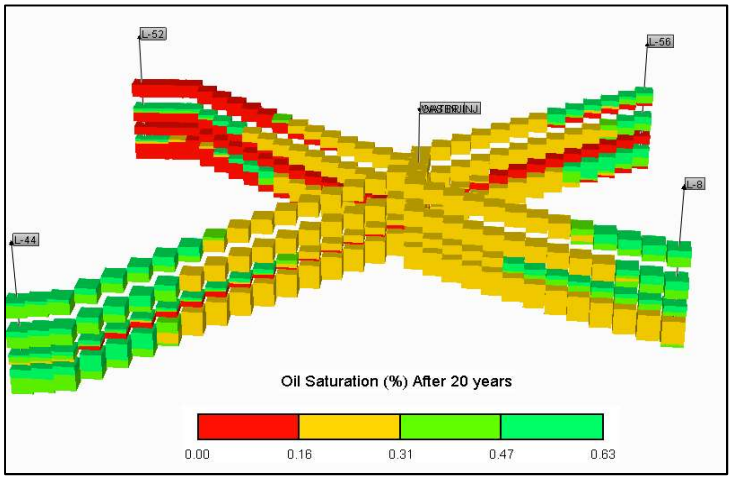

(b)

Figure 4.4. Cross-sectional map showing oil saturation distribution after 20 years for base case (intermediate) total rate (Q_t = 46,717 ft^3/day) at wet injection condition (f_g =50%): (a) no foam (MRF=1) and (b) high-strength foam (MRF=1000).

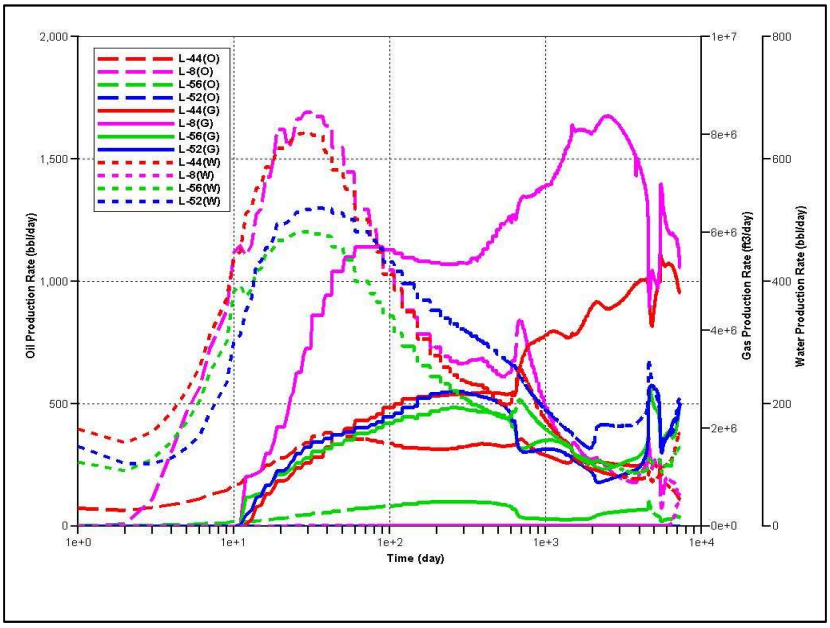

(a)

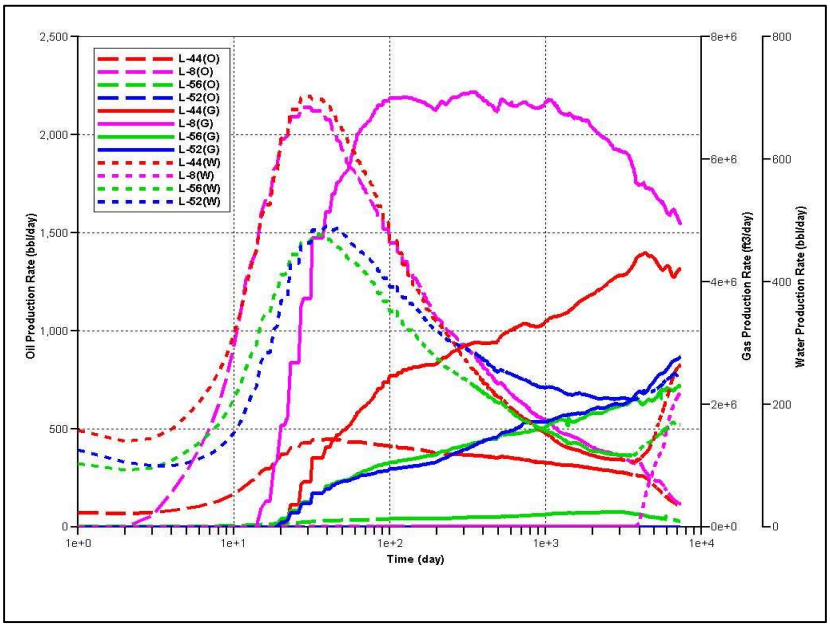

(b)

Figure 4.5. Daily oil, gas, and water production rates at 4 producers ($Q_t = 46{,}717$ ft^3/day (base case), f_g =90%): (a) MRF=1 and (b) MRF=1000.

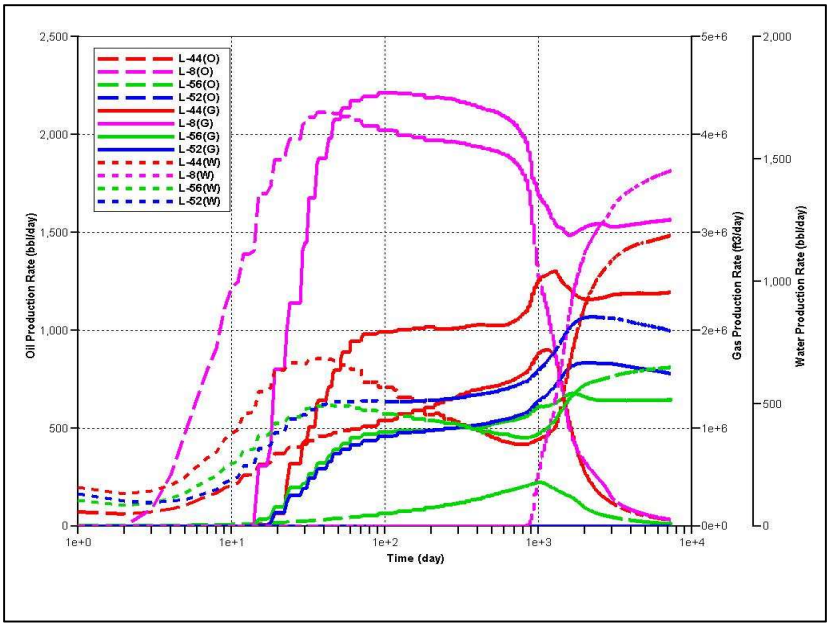

(a)

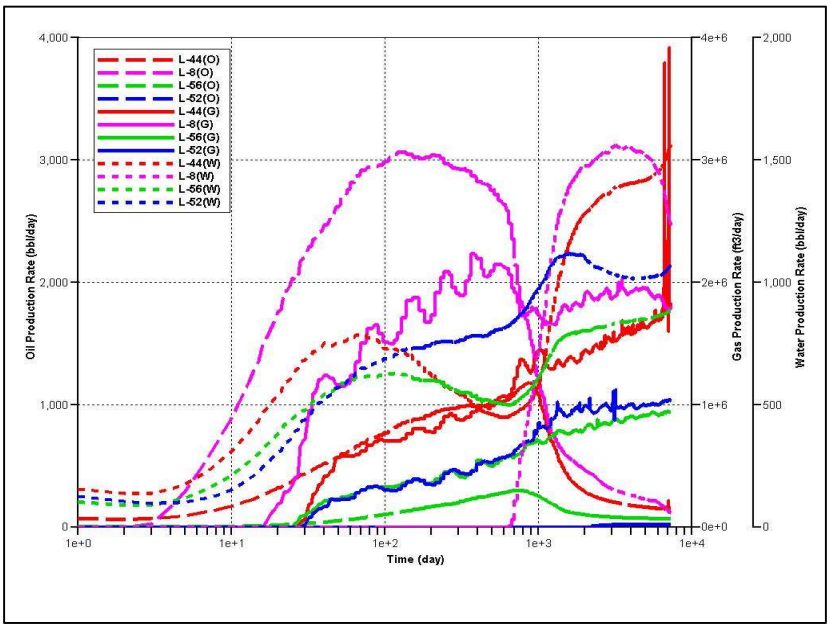

(b)

Figure 4.6. Daily oil, gas, and water production rates at 4 producers (Q_t = 46,717 ft^3/day (base case), f_g =50%): (a) MRF=1 and (b) MRF=1000.

In the case of dry injection condition (f_g = 90%) with MRF=1, the injected gas predominantly follows either up-dip direction towards well L-8 or high-permeability direction towards well L-44 to show an early breakthrough (cf. Figure 4.2). Such an effect is reflected by the map of oil saturation (Figure 4.3(a)) as well as production history (Figure 4.5(a)). In the case with MRF=1000, however, the injected gas sweeps almost in a piston-like manner, especially around the injection well. As a result, the average oil production rate for well L-8 is around 298 bbl/day when MRF=1, while the average oil production rates for this well goes up to 374 bbl/day when MRF=1000. In addition, the gas breakthrough occurs after 10 days in well L-44 when MRF=1, while the breakthrough is delayed until 18 days when MRF=1000. In the case of wet injection condition (f_g = 50%), the dip angle plays an important role showing more variation in terms of oil saturation along the vertical direction (Figure 4.4). Because gravity is helping the process (i.e., water supporting from the bottom), the oil production is improved compared to f_g = 90% (Figure 4.6). As a result, the average oil production rate for well L-44 is around 239 bbl/day when MRF=1, while the average production for this well increases to 340 bbl/day when MRF=1000. In addition, the gas production is retarded and the water production is accelerated. Figure 4.7 shows how cumulative oil recovery changes with time for MRF = 1, 10,100, and 1000, respectively. There are two distinct features that can be learned from this example: (i) the cumulative oil production increases with MRF, and (ii) wetter injection condition (or, lower f_g equivalently) generally improves the cumulative oil production when MRF is relatively low (meaning the bottom-support mechanism is more pronounced when MRF is low). As MRF increases, however, the maximum recovery occurs at an intermediate f_g, implying the mobility control plays more important roles. The

first is what is expected because of more efficient mobility control at higher MRF, while the second is more field-specific indicating that the role of gravity in this sector of interest is not negligible.

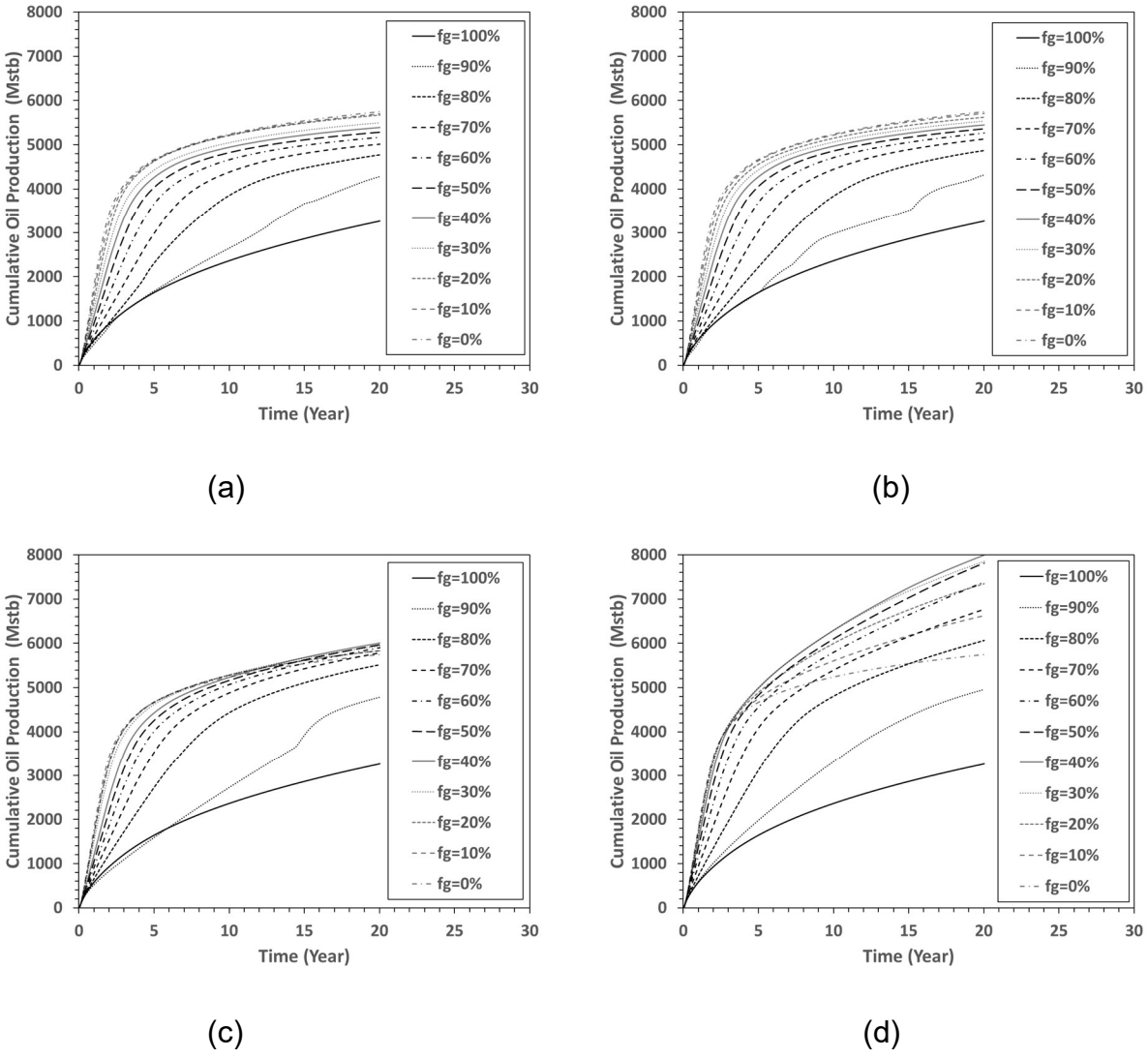

Figure 4.7. Comparison of cumulative oil production at base case (intermediate) injection rate (Q_t =46,717 ft^3/day): (a) MRF=1, (b) MRF=10, (c) MRF=100, and (d) MRF=1000.

4.4.2. Low injection rate (Q_t = 23,358 ft^3/day)

The same simulations are repeated at the lower injection rate (Q_t = 23,358 ft^3/day), as shown in Figures 4.8, 4.9, and 4.10. The results are also summarized in Table 4.3. In all cases, the average daily oil production rates for all 4 producing wells are reduced compared to those from the intermediate injection rate (Figures 4.3, 4.4, and 4.7). As a result, when f_g = 90%, the average production rate for well L-44 is down from 239 bbl/day to 202 bbl/day when MRF =1, from 240 to 197 bbl/day when MRF = 10, from 252 to 207 bbl/day when MRF = 100, and from 248 to 214 bbl/day when MRF = 1000. Such a result is primarily caused by the fact that a smaller pore volume is injected by moving from the intermediate Q_t to low Q_t. The cumulative oil recovery trend observed at low Q_t is also consistent with intermediate rate – more oil produced with higher MRF. The injection f_g at which the maximum oil recovery occurs slightly decreases at low Q_t.

Table 4.3. Summary of simulation results for the case of low injection rate (Q_t = 23,358 ft^3/day) after 20 years.

f_g (%)	Cumulative recovery (Mstb)				Sweep efficiency (%)			
	MRF=1	MRF=10	MRF=100	MRF=1000	MRF=1	MRF=10	MRF=100	MRF=1000
100	2,307	2,307	2,307	2,307	15.8	15.8	15.8	15.8
90	2,549	2,744	2,896	3,111	17.4	18.8	19.8	21.3
80	3,835	3,927	4,308	4,916	26.2	26.9	29.5	33.6
70	4,518	4,589	4,954	5,596	30.9	31.4	33.9	38.3
60	4,858	4,910	5,220	6,029	33.2	33.6	35.7	41.3
50	5,049	5,087	5,371	6,309	34.6	34.8	36.8	43.2
40	5,179	5,208	5,475	6,456	35.4	35.6	37.5	44.2
30	5,286	5,308	5,542	6,444	36.2	36.3	37.9	44.1
20	5,381	5,396	5,573	6,254	36.8	36.9	38.1	42.8
10	5,425	5,444	5,526	5,928	37.1	37.3	37.8	40.6
0	5,511	5,511	5,511	5,511	37.7	37.7	37.7	37.7

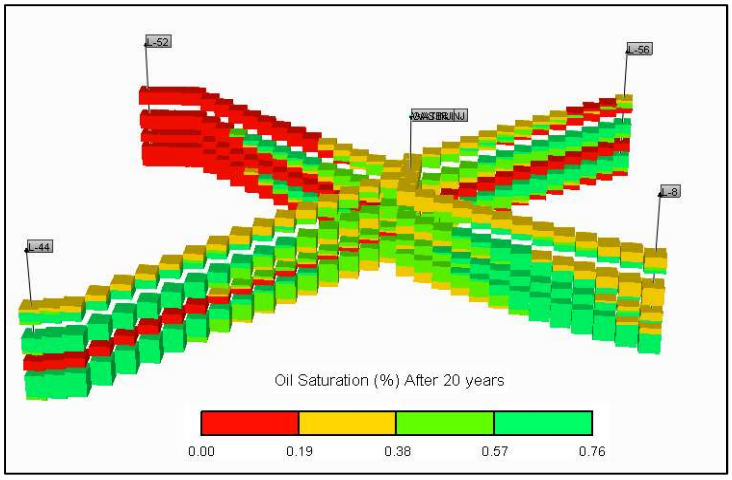

(a)

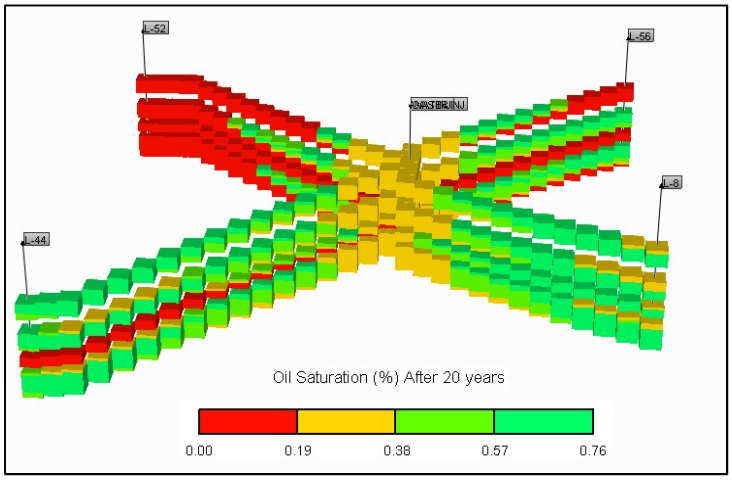

(b)

Figure 4.8. Cross-sectional map showing oil saturation distribution after 20 years for low total rate (Q_t = 23,358 ft3/day) at dry injection condition (f_g = 90%): (a) no foam (MRF = 1) and (b) high-strength foam (MRF = 1000).

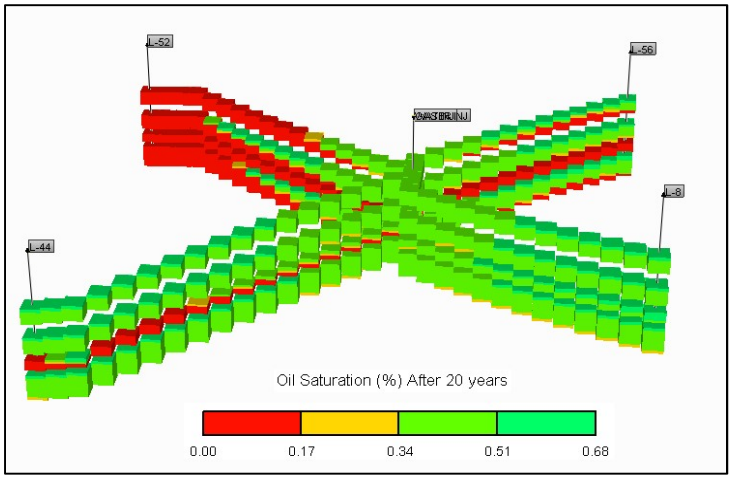

(a)

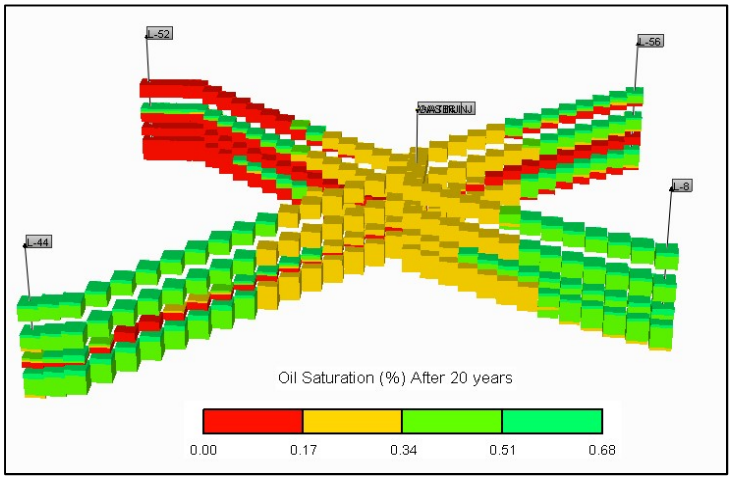

(b)

Figure 4.9. Cross-sectional map showing oil saturation distribution after 20 years for low total rate (Q_t = 23,358 ft^3/day) at wet injection condition (f_g = 50%): (a) no foam (MRF = 1) and (b) high-strength foam (MRF = 1000).

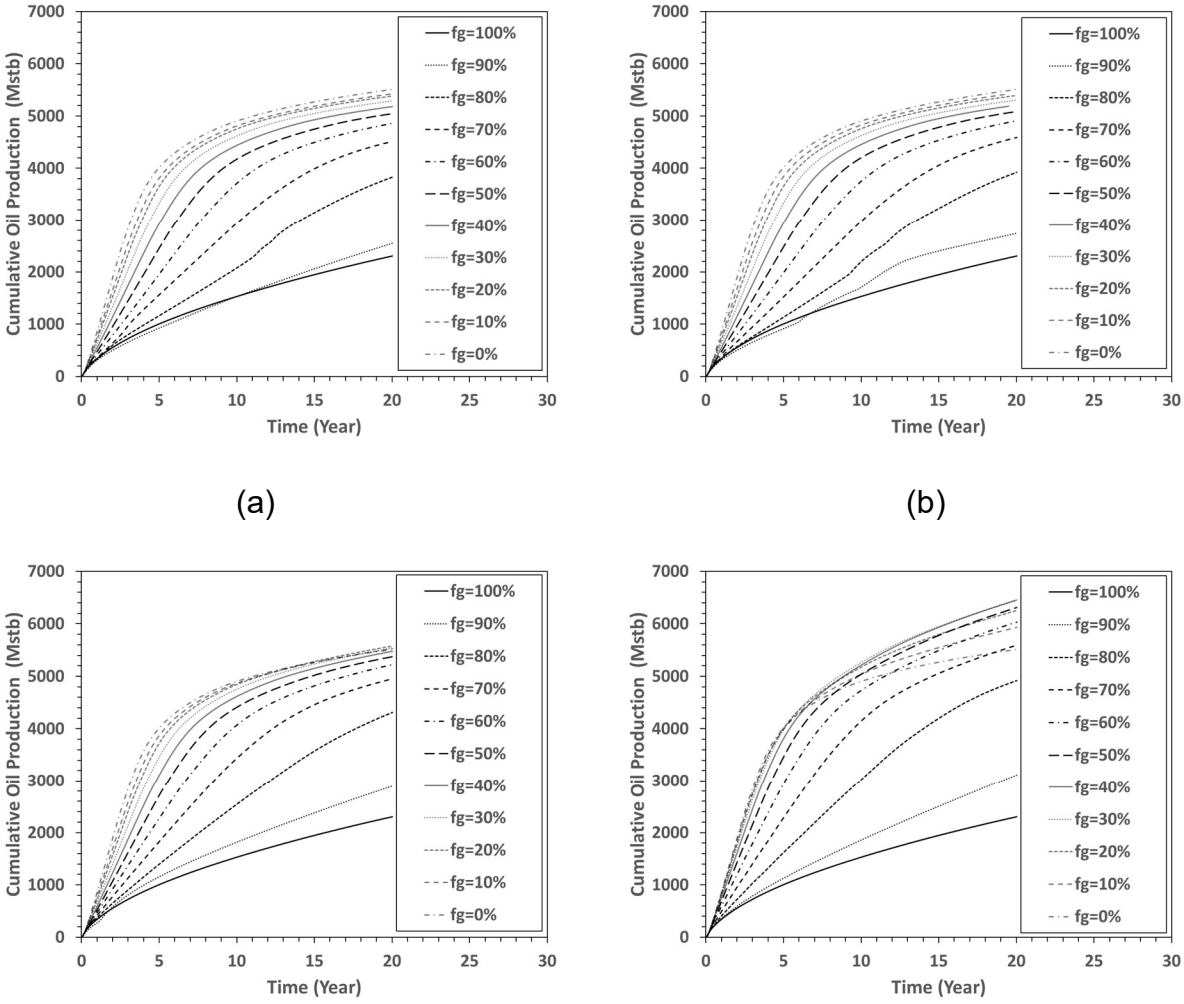

Figure 4.10. Comparison of cumulative oil production at low injection rate ($Q_t = 23{,}358$ ft^3/day): (a) MRF = 1, (b) MRF = 10, (c) MRF = 100, and (d) MRF = 1000.

4.4.3. High injection rate (Q_t = 70,075 ft^3/day)

The same simulations are repeated at the higher injection rate (Q_t = 70,075 ft^3/day), as shown in Figures 4.11, 4.12, and 4.13. The results are also summarized in Table 4.4. In all cases, the average daily oil production rates for all 4 producing wells are improved compared to those from the low and intermediate Q_t values. As a result, for f_g = 90%, the

average production rate for well L-8 is 352 bbl/day when MRF =1, 365 bbl/day when MRF =10, 415 bbl/day when MRF = 100, and 446 bbl/day when MRF = 1000. Such a result is caused by the fact that a larger pore volume is injected by moving from the low to high Q_t values.

Table 4.4. Summary of simulation results for the case of high injection rate (Q_t = 70,075 ft^3/day) after 20 years.

f_g (%)	Cumulative recovery (Mstb)				Sweep efficiency (%)			
	MRF=1	MRF=10	MRF=100	MRF=1000	MRF=1	MRF=10	MRF=100	MRF=1000
100	3,991	3,991	3,991	3,991	27.3	27.3	27.3	27.3
90	4,691	4,798	5,380	5,587	32.1	32.8	36.8	38.2
80	4,929	5,067	6,040	6,745	33.7	34.7	41.3	46.2
70	5,091	5,249	6,284	7,716	34.8	35.9	43.0	52.8
60	5,216	5,341	6,333	8,408	35.7	36.5	43.4	57.6
50	5,322	5,417	6,321	8,819	36.4	37.1	43.3	60.4
40	5,423	5,497	6,259	8,826	37.1	37.6	42.8	60.5
30	5,537	5,582	6,137	8,498	37.9	38.2	42.0	58.2
20	5,652	5,679	5,990	7,753	38.7	38.9	41.0	53.1
10	5,781	5,792	5,885	7,008	39.6	39.6	40.3	48.0
0	5,848	5,848	5,848	5,848	40.0	40.0	40.0	40.0

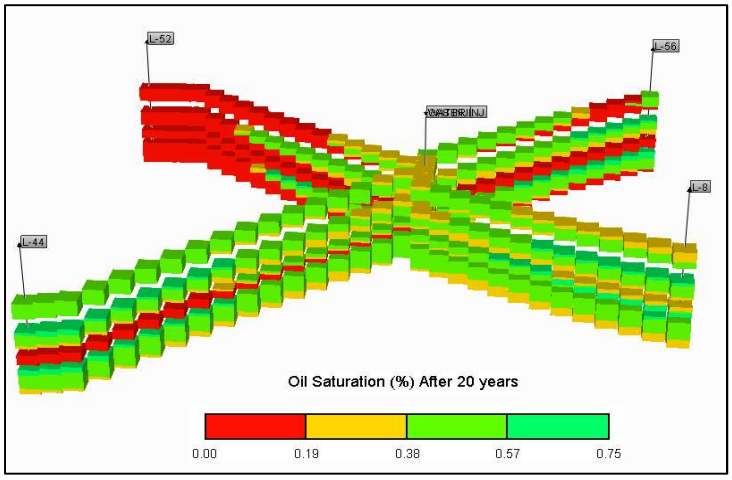

(a)

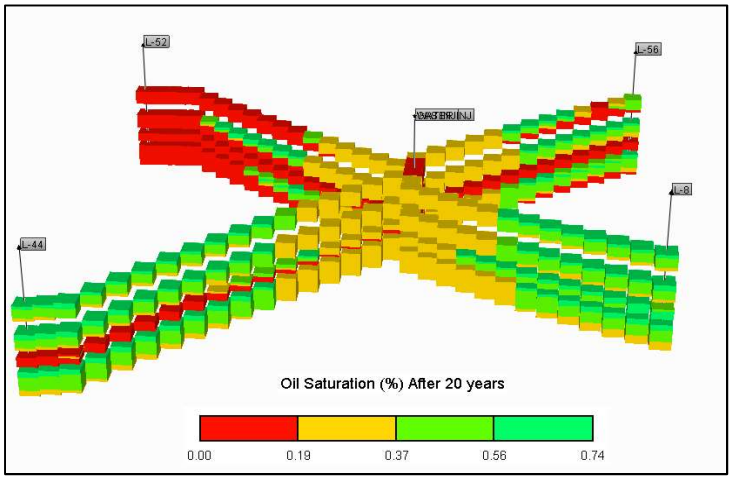

(b)

Figure 4.11. Cross-sectional map showing oil saturation distribution after 20 years for high total rate (Q_t = 70,075 ft^3/day) at dry injection condition ($\mathbf{f_g}$ = 90%): (a) no foam (MRF=1) and (b) high-strength foam (MRF = 1000).

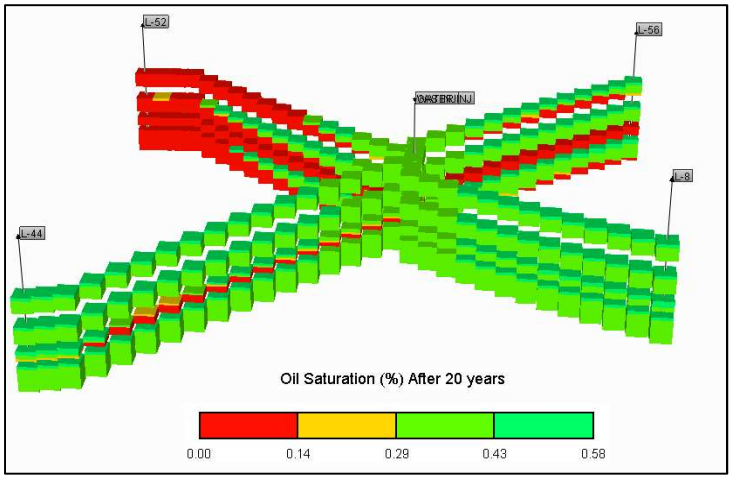

(a)

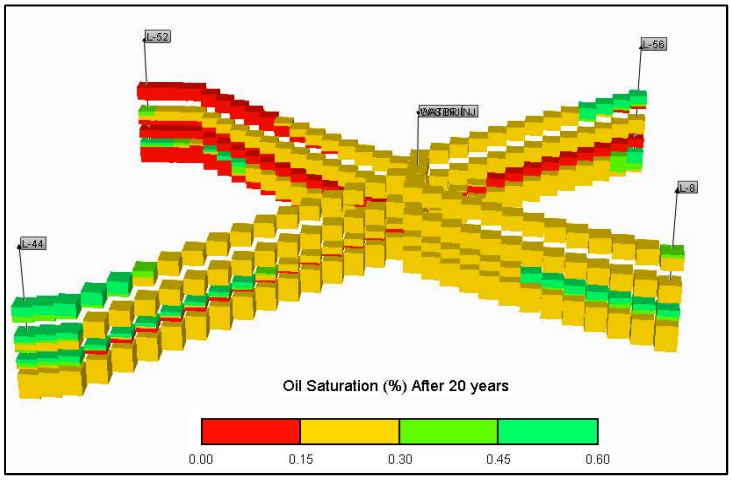

(b)

Figure 4.12. Cross-sectional map showing oil saturation distribution after 20 years for high total rate (Q_t = 70,075 ft^3/day) at wet injection condition (f_g = 50%): (a) no foam (MRF = 1) and (b) high-strength foam (MRF = 1000).

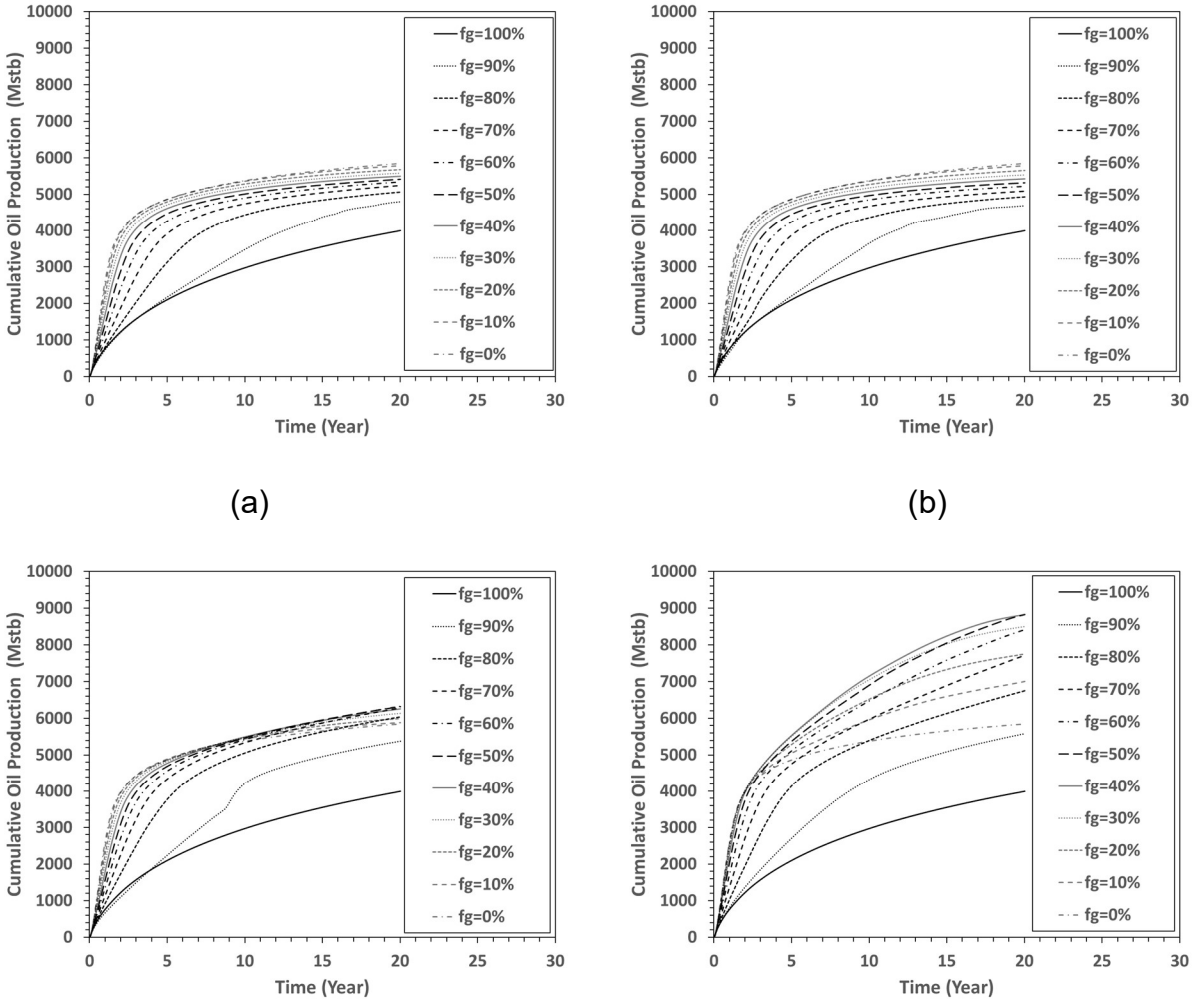

Figure 4.13. Comparison of cumulative oil production at high injection rate (Q_t = 70,075 ft^3/day): (a) MRF = 1, (b) MRF = 10, (c) MRF = 100, and (d) MRF = 1000.

4.4.4. Determination of optimum injection condition

Determination of the optimum injection condition requires lab coreflood experimental data on how MRF changes at different Q_t and f_g values, which of course depends on many field-specific conditions. To name a few, they include rock and fluid

properties, chemical formulations and concentrations (such as surfactants and additives), and interactions between foam films with reservoir fluids (especially reservoir oils) within the pores with certain surface properties. Because there are no coreflood experimental studies available from Lisama field, this study borrows the mobilities of gas and liquid, with and without foams, from Yin (2007). The mechanistic modeling technique from Izadi and Kam (2018) can be used to fit the coreflood data and further calculate the MRF values at different injection conditions.

Figure 4.14 shows the steady-state two flow-regime map of strong foams at the three Q_t values which correspond to the total injection velocity (u_t) of 1.89, 3.78, and 5.67 ft/day. The map clearly shows a regime with almost vertical pressure contours (called the high-quality regime) and the other with almost horizontal pressure contours (called the low-quality regime) separated by a threshold foam quality, f_g*. The population balance model of Izadi and Kam (2018) allows MRF values to be determined and plotted as a function of f_g for each of u_t values, as shown in Figure 4.15. Figure 4.15 demonstrates the behavior of two strong-foam flow regimes well: (i) in the low-quality regime (LQR) where foams are relatively wet and MRF is maintained within a narrow range due to bubble size staying near its minimum (around the average pore size), and (ii) in the high-quality regime (HQR) where foam are relatively dry and MRF sharply decreases with f_g due to bubble instability near the limiting capillary pressure. Such behaviors are consistent with existing studies (Kam and Rossen 2003; Lee et al. 2016).

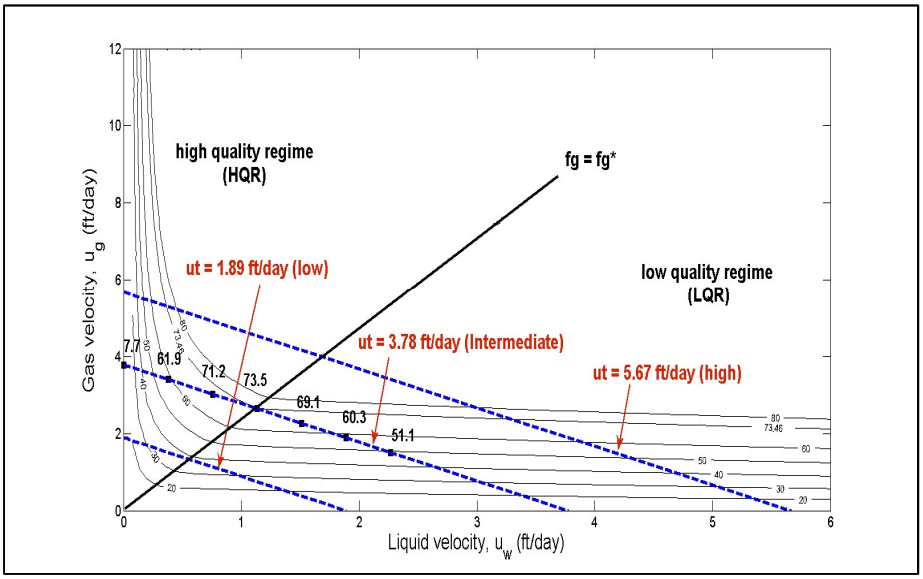

Figure 4.14. Two flow regimes of strong foams constructed in this study by using the model of Izadi and Kam (2018): low, intermediate, and high superficial velocities (u_t) correspond to total injection rates (Q_t) of 23,358, 46,717, and 70,075 ft^3/day.

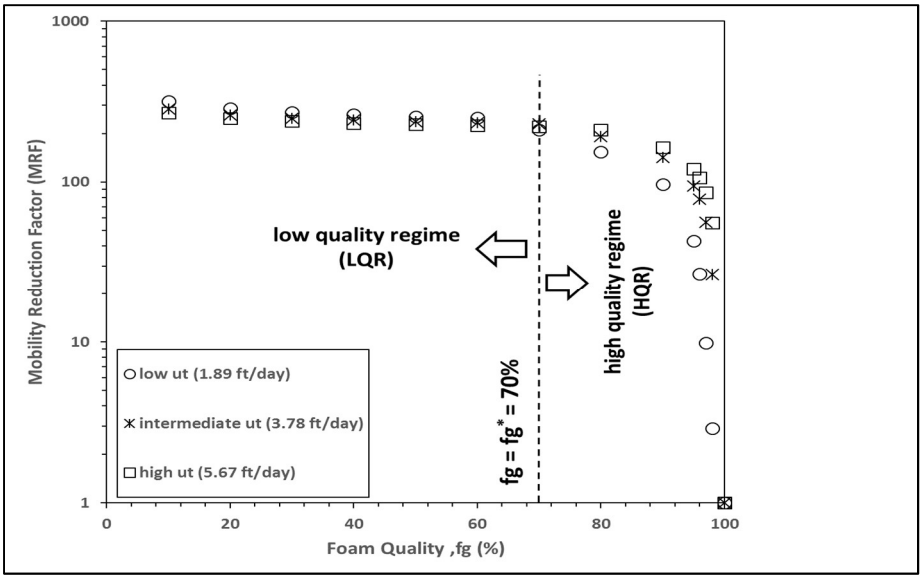

Figure 4.15. Results from mechanistic foam model (Izadi and Kam 2018) for Lisama field application showing how mobility reduction factor (MRF) changes with injection foam quality (f_g): the corresponding paths shown in Figure 4.14.

The sweep efficiency from the simulations (as summarized in Tables 4.2, 4.3, and 4.4) at various MRF and f_g values can be used to construct sweep-efficiency contours. In addition, MRF as a function of f_g from mechanistic model can be imposed on the top of contours. These results are shown in Figures 4.16 through 4.18 for Q_t = 46,717, 23,358, and 70,075 ft^3/day, respectively. Figure 4.16 shows the results of sweep efficiency (which is, in fact, equivalent to the cumulative oil production) at the intermediate Q_t as a function of MRF and f_g values. The MRF calculated in Figure 4.15 (i.e., the dashed curve in Figure 4.16) is mapped out on the sweep-efficiency contours. The same can be performed for low and high Q_t values, as shown in Figures 4.17 and 4.18.

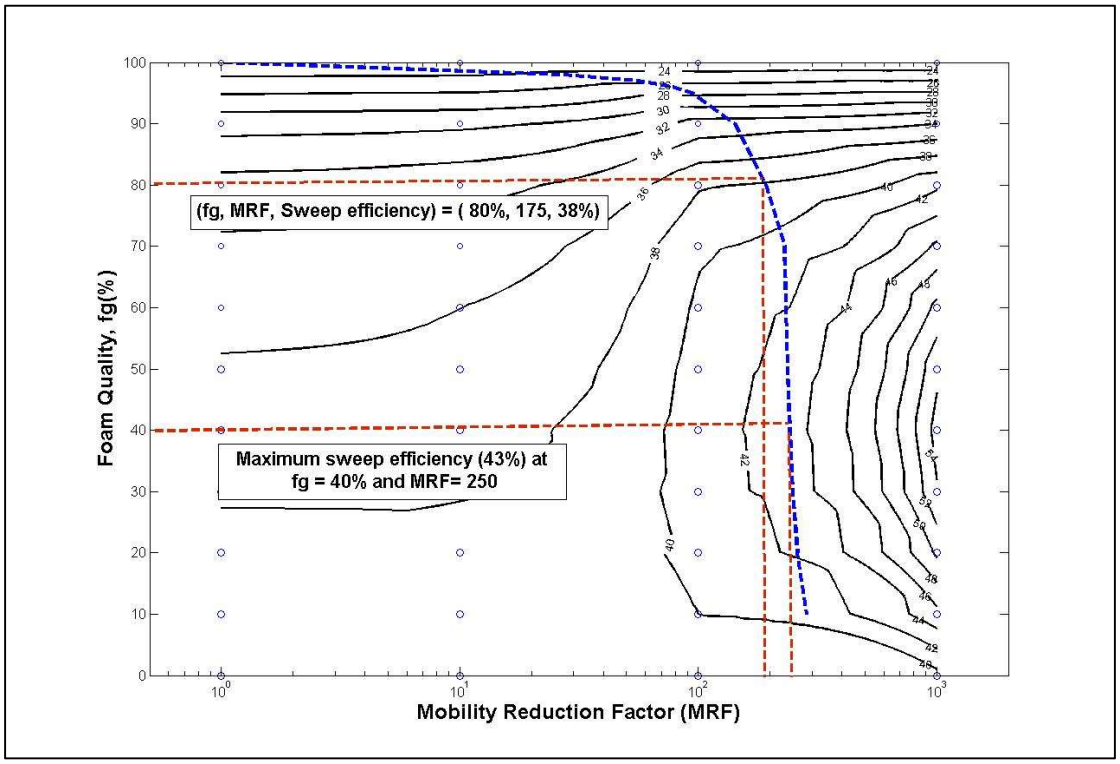

Figure 4.16. Mapping of MRF-f_g path from mechanistic model on the sweep-efficiency contour map: base case (intermediate) injection rate (Q_t = 46,717 ft^3/day).

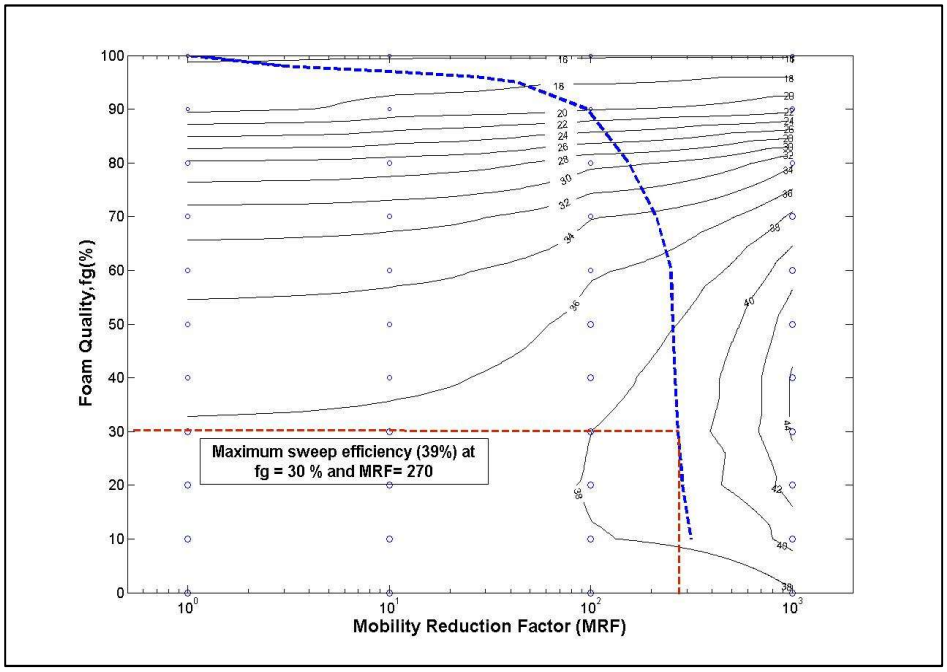

Figure 4.17. Mapping of MRF-f_g path from mechanistic model on the sweep-efficiency contour map: low injection rate (Q_t =23,358 ft^3/day).

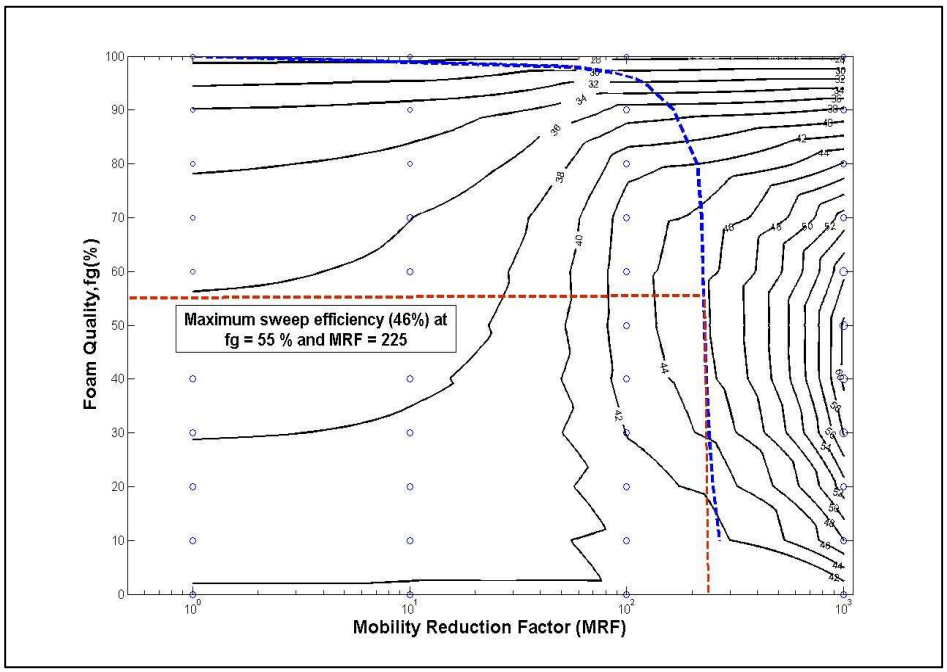

Figure 4.18. Mapping of MRF-f_g path from mechanistic model on the sweep-efficiency contour map: high injection rate (Q_t = 70,075 ft^3/day).

One may then notice from Figures 4.16 through 4.18 that any intersection point between a particular sweep-efficiency contour and the MRF-f_g path allows a data set of (f_g, MRF, sweep efficiency) to be determined. For example, in the base case (Figure 4.16), an intersection point of the two near f_g = 80% provides (f_g, MRF, sweep efficiency) = (80%, 175, 38%) approximately, meaning that 38% of sweep efficiency can be obtained from f_g = 80% that has an MRF value of 175 from mechanistic foam modeling (or, core flood experiments). Because the sweep-efficiency contours in Figure 4.16 are curved to the right, this implies that the sweep efficiency increases with decreasing f_g (when fg > 40%), down to about f_g = 40% where the sweep efficiency is about 43%, beyond which the sweep efficiency decreases with decreasing f_g (when f_g < 40%). That particular point providing the maximum sweep efficiency is defined as the optimum condition in this study, that is, (f_g, MRF, sweep efficiency) = (40%, 250, 43%) approximately in Figure 4.16. Figures 4.17 and 4.18 also show similar behaviors. Figure 4.19 shows a summary of such an analysis, plotting the sweep efficiency as a function of f_g for all three Q_t values. The trend is consistent as expected from Figure 4.15 that there is a particular value of f_g at which the sweep efficiency reaches the maximum, and those f_g values change with Q_t values. In general, higher Q_t leads to higher sweep efficiency that occurs at higher optimum f_g.

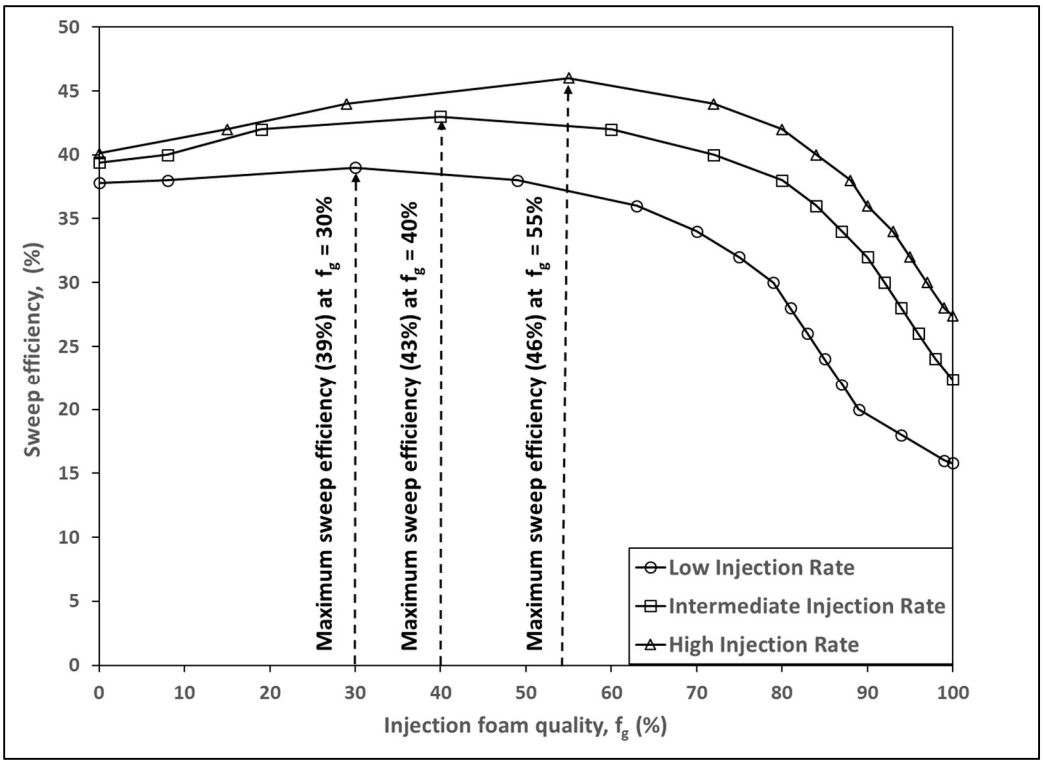

Figure 4.19. Summary of Figures 4.16 through 4.18 showing the effect of total injection rate on the sweep efficiency as well as optimum injection foam quality.

4.5. Discussions

This new technique and resulting plots presented in Figures 4.16 through 4.19 are believed to be a simple but robust tool to help making technical and business decisions – not only showing how sweep efficiency changes at different foam qualities and strengths, but also how such an optimum condition may shift depending on different operation conditions (see Figures 4.16 through 4.19 as an example to demonstrate the use of this technique to predict the impact of total injection rates). This section shares a few more examples showing how this new technique can be applied.

The first example is to evaluate the effect of transmissibility through shales, slightly permeable (i.e., shale permeability = 5 md, 0.1 md, 0.01 md, and 0.001 md in Figures 4.20(a) through 4.20(d)) rather than impermeable. When the shale layers are allowed to communicate vertically with surrounding layers at the higher injection rate (Q_t = 70,075 ft^3/day), the results construct contours as shown in Figure 4.20 (this can be compared with Figure 4.18 at the same Q_t but zero shale permeability). Two main observations are made. First, the presence of shale permeability (Figures 4.20(a) through 4.20(d)) changes the optimum injection foam quality to around f_g = 70% (from 55% when no shale permeability (Figure 4.18)), which is caused by more severe gravity segregation for a thicker reservoir. Second, the maximum sweep efficiency is about 37.5%, 40%, 41% and 41% at the shale permeability = 5 md, 0.1 md, 0.01 md, and 0.001 md, respectively, which again shows difficulties in dealing with a thicker reservoir due to gravity segregation. These values are considerably lower than the maximum sweep efficiency (46%) when there is no shale permeability (Figure 4.18). This example emphasizes the importance of detailed and reliable reservoir description for better EOR design and implementation.

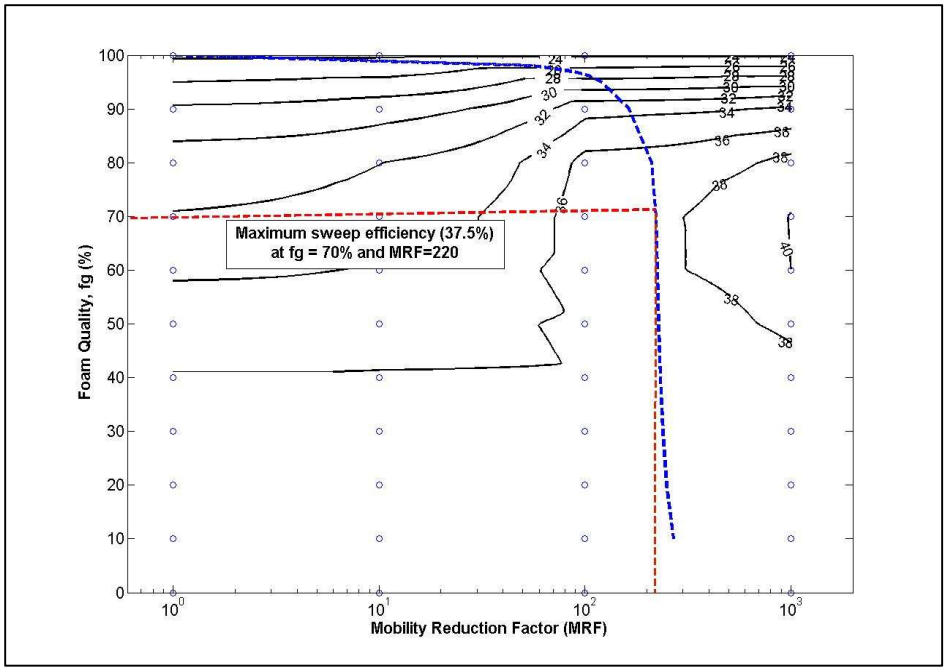

(a)

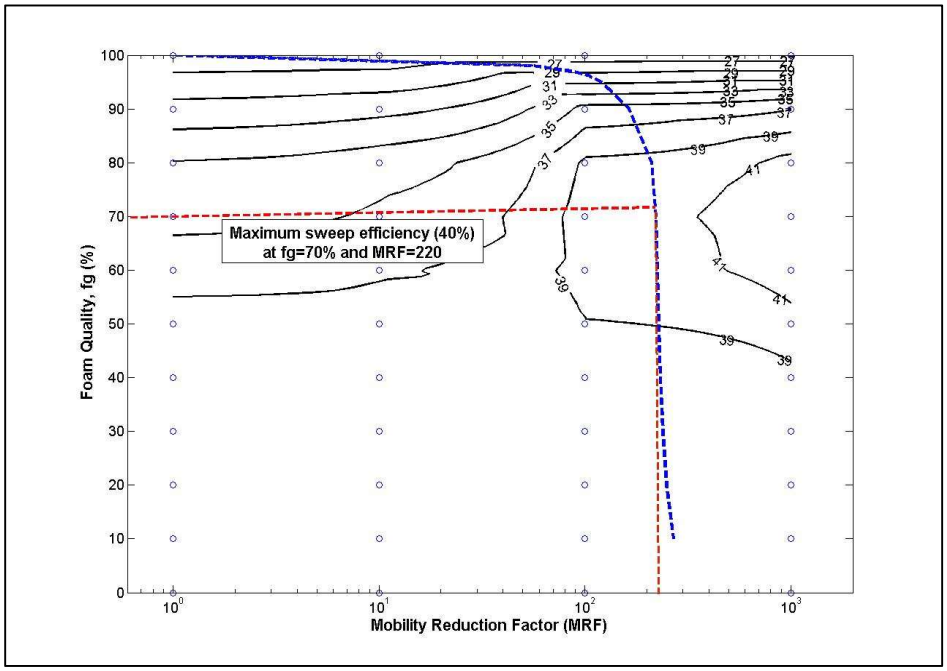

(b)

Figure 4.20. Contours showing the effect of shale permeability (Q_t = 70,075 ft^3/day) in comparison with no shale permeability (Figure 4.18): (a) shale permeability = 5 md; (b) 0.1 md; (c) 0.01 md; and (d) 0.001 md.

(figure cont'd.)

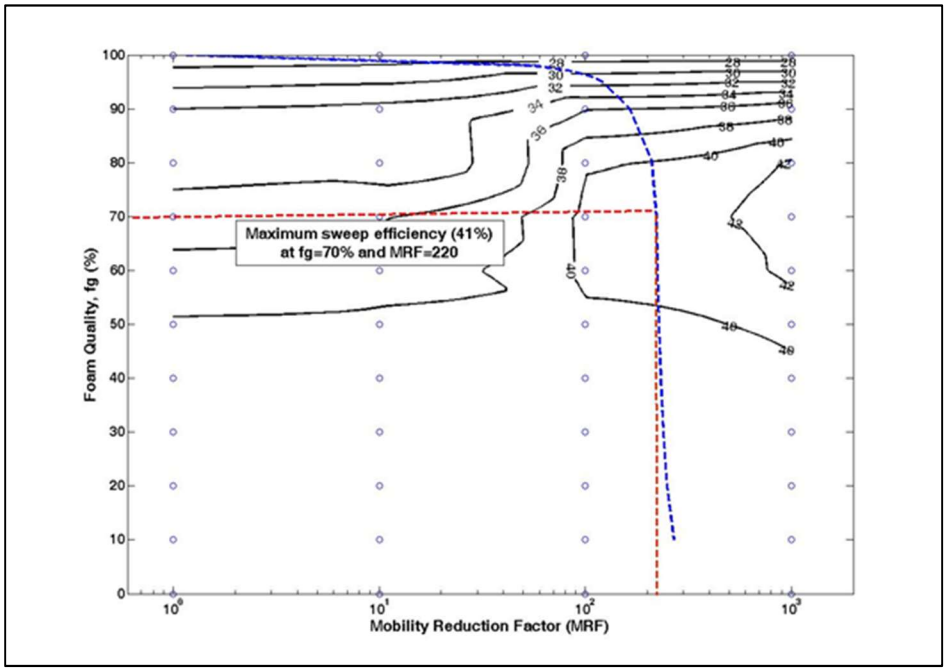

(c)

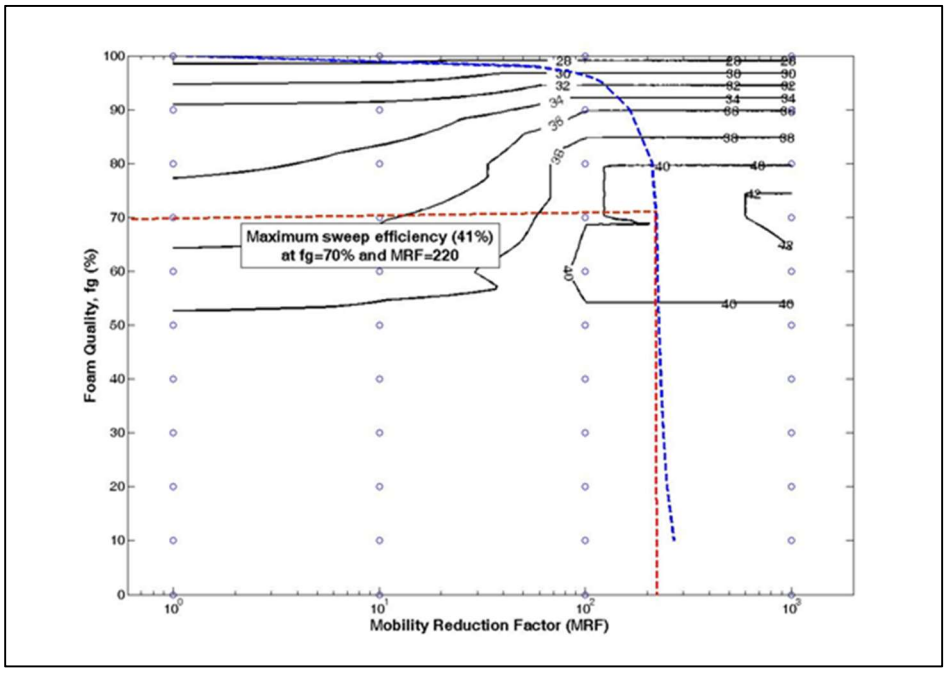

(d)

The second example is to take the effect of CO_2 and surfactant costs into accounts. Suppose one barrel of oil produced from this process makes a net profit of \$30. The sweep efficiency at Q_t = 70,075 ft^3/day (Figure 4.18) and the corresponding cumulative oil recovery (Table 4.4) allow the total profit contours (in million \$) to be determined as shown in Figure 4.21(a). Note that these contours in Figure 4.21(a) are the same as those in Figure 4.18, but with total profits rather than sweep efficiency values, assuming that CO_2 and surfactant chemicals do not make any price or economic advantages as raw materials to be injected. Using f_g = 50% as a basis, suppose CO_2 is advantaged over surfactant chemicals, economically, such that 10% increase in f_g (meaning 10% reduction in f_w) helps the net profit by \$1.00 per barrel of oil produced at the same Q_t. This means that one barrel of oil has \$30 net profit when f_g = 50%, but \$35 and \$25 net profits when f_g = 100% and f_g = 0%, respectively. This economic advantage of CO_2 over surfactant, as shown in Figure 4.21(b), causes the change in contours, making drier injection condition more favored, shifting the optimum injection f_g value for maximum net profit (from \$200 million at f_g = 50% to \$210 million at f_g = 70%). It should be noted that there is no change in sweep efficiency in Figures 4.21(a) and 4.21(b), but the market and economic situations can distort such an analysis outcome. In addition to CO_2 and surfactant costs, other factors can be incorporated similarly such as oil price, transportation cost, equipment cost, operation cost, and so on.

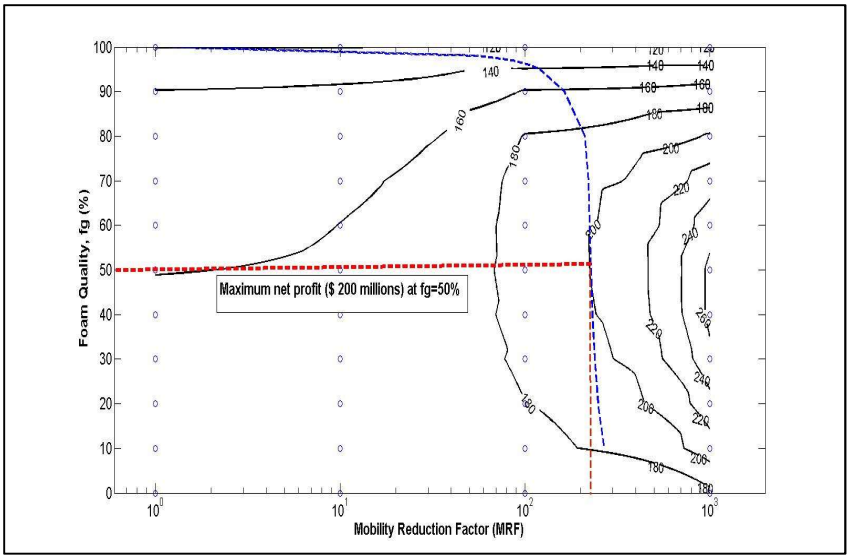

(a)

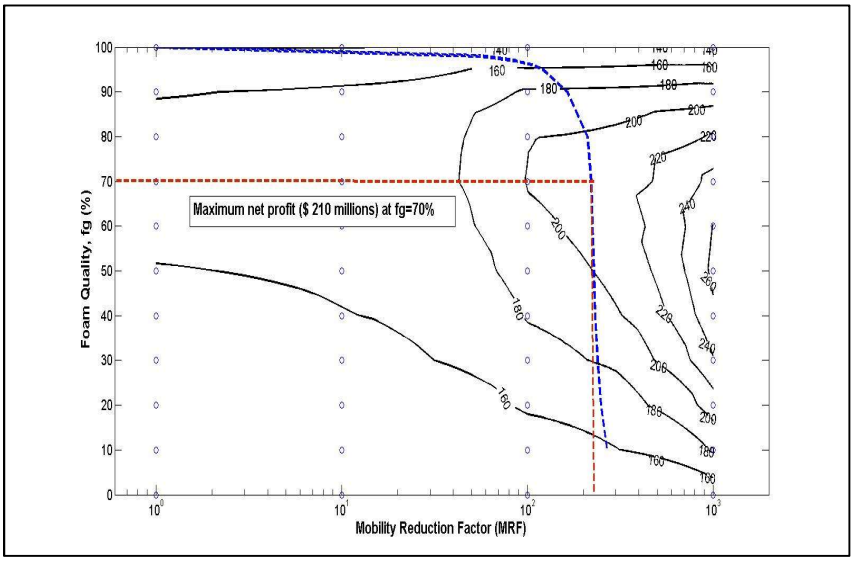

(b)

Figure 4.21. Contours showing total profits (million $) to find the optimum condition for business decision (Q_t = 70,075 ft^3/day, Figure 4.18) when the net profit is $30/bbl: (a) when CO_2 and surfactant, as raw materials to be injected, make no economic advantages compared each other and (b) when CO_2 makes economic advantages over surfactant.

The third example is to consider the case when there is a limited supply of CO_2 that may happen, for example, due to geographical and geopolitical aspects. If Q_t = 70,075 ft^3/day (Figure 4.18) is used as an example, Figures 4.22(a) and 4.22(b) show illustrations with horizontal lines when Q_g is limited to 49,053 ft^3/day (f_g = 70%) and 28,030 ft^3/day (f_g = 40%), respectively. Such a limitation does not affect the optimum condition if the injection f_g is greater than the optimum f_g (Figure 4.22(a)), while it reduces the maximum sweep efficiency if the injection f_g is less than the optimum f_g as much as the shift in f_g due to the limited supply (Figure 4.22(b)). This example can also be used in the field when the quantity of overall CO_2 supply is fixed but needs to be distributed into multiple sectors where each of which has its own optimum condition. Similar approaches can be used when additional constraints exist for other chemicals (e.g., limitation in terms of surfactant chemicals, water supply, etc.)

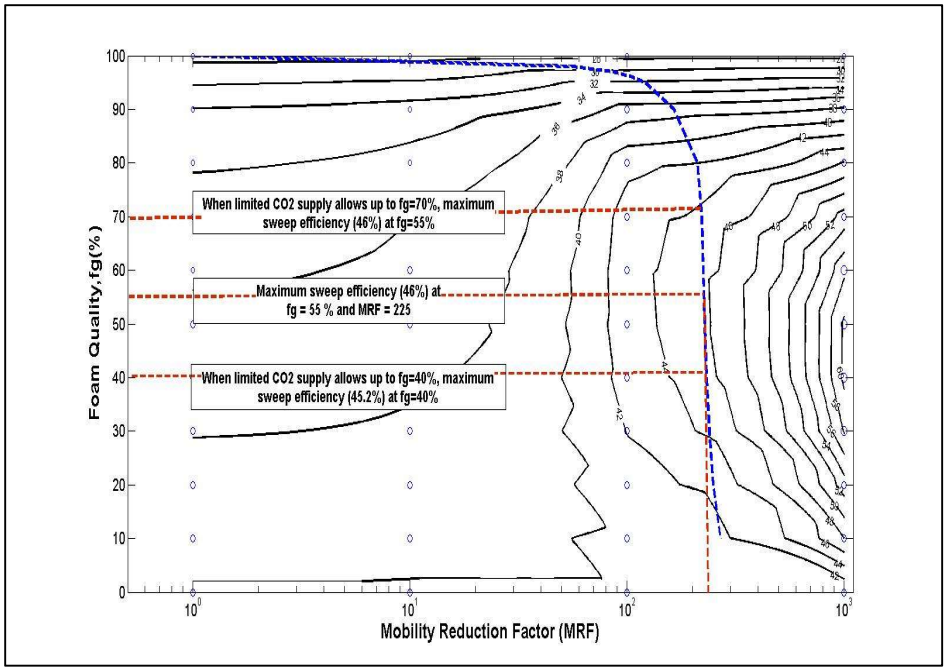

(a)

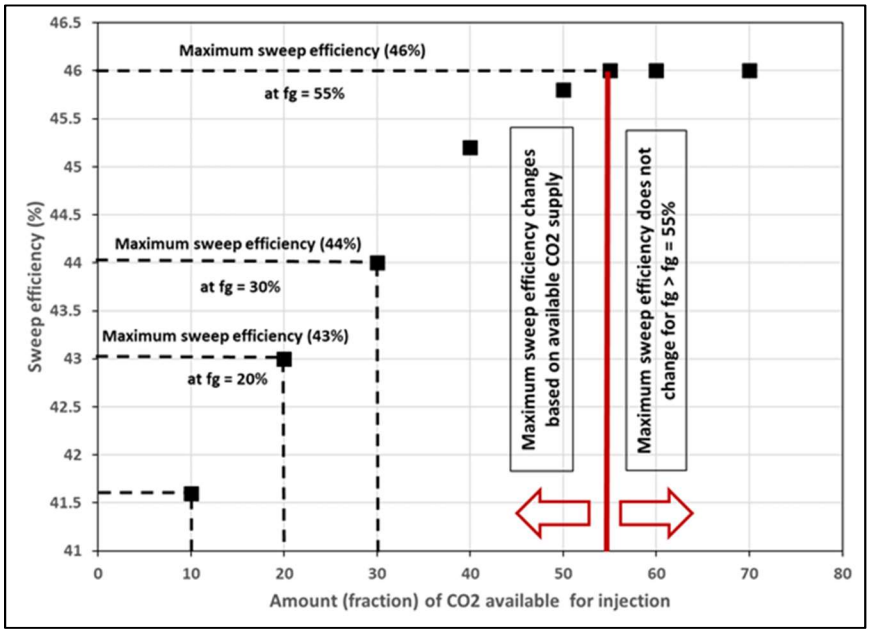

(b)

Figure 4.22. Effect of a limited CO_2 supply on the optimum condition (Q_t = 70,075 ft^3/day, Figure 4.18): (a) sweep efficiency contour lines with such constraints (b) Implication to determine the optimum f_g.

4.6. Conclusions

This study performs reservoir simulations for a sector with one injection well and four production wells in Lisama field, Columbia, in order to determine the optimum injection strategies for gas-water coinjection as well as foam treatments. A wide range of scenarios are evaluated including low, intermediate, and high injection rates (Q_t = 23,358, 46,717 and 70,075 ft^3/day), various injection gas fractions (f_g = 100 to 0%), and different foam strengths (no foam, low-strength foam, intermediate-strength foam and high-strength foam with mobility reduction factor (MRF) of 1, 10, 100, 1000). Mechanistic foam model from Izadi and Kam (2018) is applied and calculates MRF values to reflect complex foam rheological properties with two strong-foam flow regimes. The following conclusions can be drawn from this study:

- In all cases investigated at given Q_t values, the sweep efficiency (or the cumulative oil production) increases with increasing MRF. This indicates the use of mobility-control foam can be a promising solution to improve oil recovery from the field.

- The optimum condition changes with Q_t values such that the injection f_g that provides the maximum sweep efficiency increases with increasing Q_t. This means that at low Q_t, gravity helps oil recovery for water to support from the bottom, while at high Q_t, high MRF takes over and becomes a dominating factor making more piston-like displacement front.

- This study shows how the contours of sweep efficiency as a function of injection foam quality and MRF can be used together to come up with the optimum injection strategy graphically, resulting in the maximum oil recovery. How certain constraints present in the field can be applied to determine the optimum injection strategy (i.e., total injection rates and foam quality) is also demonstrated graphically by using examples. These examples also prove the versatility and robustness of this technique of combining sweep-efficiency contours and MRF-f_g path.

CHAPTER 5. CONCLUSIONS AND RECOMMENDATIONS

The conclusions related to each topic are provided at the end of each chapter. After putting all results together, the followings summarize the findings of this study:

- Model fit to laboratory experimental data is necessary to calibrate mechanistic foam models. Supercritical CO_2 foam has very low mobilization pressure gradient (∇P_o), and therefore it has unique advantages compared to other gaseous foams (gas CO_2, N_2, hydrocarbon, flue gas etc.) to create stable foams at low pressure-gradient environment and place foams deep into the reservoir.
- Mechanistic foam modeling can help designing field foam EOR processes including reservoir-scale simulations. Such an example is shown with CMG STARS foam simulations (with gas mobility taken from mechanistic modeling) is demonstrating how to select optimum injection conditions in terms of injection foam quality and injection rate.

The following recommendations can be made based on this study:

- When coreflood experiments are conducted, additional experiments to capture the transition from weak foam to strong foam are highly recommended. This onset of strong foam generation can greatly improve the quality of mechanistic foam modeling. At a minimal level, a series of coreflood data is needed for model fit, such as steady-state pressure measurements varying total velocity at the same foam quality, varying gas velocity at the same liquid velocity, or varying liquid velocity at the same gas velocity, as shown in this study.

- Not many coreflood experimental studies in radial geometry are available in the literature. Such experimental data would be very valuable to calibrate foam model, filling the gap between small lab-scale linear flow experiments and large-scale radial flow field EOR processes.

- This study only focuses on the steady-state responses. Dynamic transient simulations are required to investigate how the system changes with time. The presence of oil in the reservoir should be accounted for in realistic EOR applications to calculate oil recovery.

REFERENCES

Aarra, M.G., Skauge, A., Solbakken, J., Ormehaug, P.A. 2014. Properties of N_2 and CO_2 foams as a function of pressure. *Journal of Petroleum Science and Engineering*, 116: 72-80. https://doi.org/10.1016/j.petrol.2014.02.017.

Afsharpoor, A., Lee, G.S., Kam, S.I. 2010. Mechanistic simulation of continuous gas injection period during surfactant-alternating-gas (SAG) processes using foam catastrophe theory. *Chemical Engineering Science*, 65(11), 3615-3631. https://doi.org/10.1016/j.ces.2010.03.001.

Alvarez, J.M., Rivas, H., Rossen, W.R. 2001. A unified model for steady-state foam behavior at high and low foam qualities. SPE-74141-PA. *SPE Journal,* 6(03), 325-333.

Ashoori, E., van der Heijden, T.L.M., Rossen, W.R. 2010. Fractional-flow theory of foam displacements with oil. *SPE Journal*, 15, 260-273.

Attanucci, V., Aslesen, K. S., Hejl, K. A., Wright, C.A. 1993. WAG Process Optimization in the Rangely CO_2 Miscible Flood. SPE Annual Technical Conference and Exhibition, 3-6 Oct, Houston, Texas. https://doi.org/10.2118/26622-MS.

Beard, D.C., Weyl, P.K. 1973. Influence of texture on porosity and permeability of unconsolidated sand. *American Association of Petroleum Geologists (AAPG) Bulletin*, 57(2), 349-369.

Bernard, G.G., Holm, L.W., Jacobs, L.W. 1965. Effect of Foam on Trapped Gas Saturation and on Permeability of Porous Media to Gas. *SPE Journal*, 5(4), 295-300.

Blackwell, R.J., Terry, W.M., Rayne, J.R., Lindley, D.C., Henderson, J.R.1959. Recovery of Oil by Displacements with Water-Solvent Mixtures. *Petrol Trans AIME* (219): 293-300.

Bond, D.C., Holbrook, C. 1958. Gas drive oil recovery process. US Patent # 2,866,507.1958

Buckley, S.E., Leverett, M.C.1942. Mechanism of Fluid Displacement in Sands. *Trans AIME* 01(146): 107-116. https://doi.org/10.2118/942107-G.

Caudle, B.H., Dyes, A.B.1957. Improving Miscible Displacement by Gas-water Injection. *Petrol Trans AIME* (213): 281-284.

Chambers, K. T., Radke, C. J. 1991. Capillary phenomena in foam flow through porous media. In: N. R. Morrow (Ed.), Interfacial Phenomena in Petroleum Recovery. Marcel Dekker Inc., New York, N.Y., 191-255.

Chen, Q., Gerritsen, M.G., Kovscek, A.R. 2010. Modeling Foam Displacement with the Local-Equilibrium Approximation: Theory and Experimental Verification. *SPE Journal*, 15(1): 171-183.

Cheng, L., Kam, S. I., Delshad, M., Rossen, W.R. 2001. Simulation of Dynamic Foam-Acid Diversion Processes. Presented at the SPE European Formation Damage Conference, Hague, Netherlands. 21-22 May, SPE 68916-MS. https://doi.org/10.2118/68916-MS.

Christensen, J. R., Stenby, E. H., Skauge, A. 2001. Review of WAG Field Experience. *SPE Reservoir Evaluation & Engineering* 02 (4): 97-106. https://doi.org/10.2118/71203-PA.

Computer Modeling Group (CMG): User's Guide: STARS Advanced Process and Thermal Reservoir Simulator. Calgary, Alberta, Canada (2016).

Conn, C.A., Ma, K., Hirasaki, G.J., Biswal, S.L. 2014. Visualizing oil displacement with foam in a microfluidic device with permeability contrast. *Royal Society of Chemistry*, 14, 3968-3977.

Dietz, D.N.1953. A Theoretical Approach to the Problem of Encroaching and By-passing Edge Water. *Proc Acad Scie* (56): 83. Akad. Van Wetenschappen, Amsterdam, Netherlands.

Djabbarah, N. F., Weber, S. L., Freeman, D. C., Muscatello, J. A., Ashbaugh, J. P., Covington, T. E. 1990. Laboratory Design and Field Demonstration of Steam Diversion with Foam. Presented at the SPE California Regional Meeting, 4-6 April, Ventura, CA, USA. https://doi.org/10.2118/20067-MS.

Dyes, A. B., Caudle, B. H., Erickson, R. A. 1954. Oil Production after Breakthrough as Influenced by Mobility Ratio. *J Pet Technol* 04 (6): 27-32. https://doi.org/10.2118/309-G.

Falls, A. H., Hirasaki, G. J., Patzek, T. W., Gauglitz, D. A., Miller, D. D., Ratulowski, T. 1988. Development of a Mechanistic Foam Simulator: The Population Balance and Generation by Snap-Off. *SPE Res Eng* **03** (3): 884-892. SPE 14961-PA. https://doi.org/10.2118/14961-PA.

Farajzadeh, R., Lotfollahi, M., Eftekhari, A.A., Rossen, W.R., Hirasaki, J.H. 2015. Effect of permeability on implicit-texture foam model parameters and the limiting capillary pressure. *Energy Fuels*, 29(5): 3011-3018.

Fenghour, A., Wakeham, W.A.1998. The viscosity of Carbon Dioxide. *Journal of Physical and Chemical Reference Data*, 27(1), 31-44.

Fernø, M. A., Gauteplass, J., Pancharoen, M., Haugen, A., Graue, A., Kovscek, A. R., Hirasaki, G. 2016. Experimental Study of Foam Generation, Sweep Efficiency, and

Flow in a Fracture Network. *SPE Journal* (21) 04: 1140-1150. https://doi.org/10.2118/170840-PA.

Friedmann, F., Chen, W.H., Gauglitz, P.A. 1991. Experimental and simulation study of high-temperature foam displacement in porous media. *SPE Reservoir Engineering*, 37-45.

Friedmann, F., Jensen, J. A. 1986. Some Parameters Influencing the Formation and Propagation of Foams in Porous Media. Presented at the SPE California Regional Meeting, 2-4 April, Oakland, CA, USA. https://doi.org/10.2118/15087-MS.

Gauglitz, P.A., Friedmann, F., Kam, S.I., Rossen, W.R. 2002. Foam generation in homogeneous porous media. *Chemical Engineering Science* 57(19), 4037-4052.

Gauteplass, J., Chaudary, K., Kovscek, A. R., Fernø, M. A. 2015. Pore-level foam generation and flow for mobility control in fractured systems. *Colloids and Surfaces A: Physicochemical and Engineering Aspects* (486) 184-192. https://doi.org/10.1016/j.colsurfa.2014.12.043.

Georgiadis, A., Maitland, G., Martin Trusler, J. et al. 2010. Interfacial Tension Measurements of the (H2O + CO2) System at Elevated Pressures and Temperatures. *J Chem Eng Data* (55) 10: 4168-4175 (2010). https://doi.org/10.1021/je100198g.

Ghahfarokhi, R. B., Pennell, S., Matson, M., Linroth, M. 2016. Overview of CO2 Injection and WAG Sensitivity in SACROC. Presented at the SPE Improved Oil Recovery Conference, Tulsa, Oklahoma. 11-13 April, SPE 179569-MS. https://doi.org/10.2118/179569-MS.

Gomez Moncada, R. A., Morales Rojas, J., Perez Vega, H. H., Sandoval Munoz, J.E.E.S., Jaimes Bohorquez, M. A. 2009. Impact Analysis and Interpretation of the Sand Thickness Obtained from Electric Logs and Outcrops in the Geostatistical Modeling of Stratigraphic Complex. Presented at the SPE Latin American and Caribbean Petroleum Engineering Conference, Cartagena de Indias, Colombia. 31 May-3 June, SPE 122234-MS. https://doi.org/10.2118/122234-MS.

Haugen, A., Fernø, M. A., Graue, A., Bertin, H. J. 2012. Experimental Study of Foam Flow in Fractured Oil-Wet Limestone for Enhanced Oil Recovery. *SPE Reservoir Evaluation and Engineering* 02 (15): 218-228. https://doi.org/10.2118/129763-PA.

Hill, M.A., Inst, P.F.S.S.1952. Channeling in Packed Columns. *Chem Eng Sci* 06 (1) 247-253. https://doi.org/10.1016/0009-2509(52)87017-4.

Hirasaki, G. J. 1989.The Steam-Foam Process. J Petrol Tech (41) 05: 449-456. SPE 19505-PA. https://doi.org/10.2118/19505-PA.

Hirasaki, G. J., Miller, C. A., Szafranski, R., Tanzil, D., Lawson, J. B., Meinardus, H., Wade, W. H. 1997. Field Demonstration of the Surfactant/Foam Process for Aquifer Remediation. Presented at the SPE Annual Technical Conference and Exhibition, 5-8 October, San Antonio, Texas, USA. https://doi.org/10.2118/39292-MS.

Hirasaki, G.J., Lawson, J.B., 1985. Mechanisms of foam flow through porous Media-apparent viscosity in smooth capillaries. *SPE Journal* 25(02*)*, 176-190.

Hirasaki, G.J., Miller, C.A., Lawson, J.B., Akiya, N., and Szafranski, R., 1997. Surfactant/foam process for Aquifer remediation. SPE 37257. Presented at the International Symposium on Oilfield Chemistry, 18-21 February, Houston, Texas, USA.

Holm, L.W. 1968. The Mechanism of Gas and Liquid Flow Through Porous Media in the Presence of Foam. *SPE J*, 8(4), 359-369.

Holm, L.W., Garrison, W.H.1988. CO2 Diversion with Foam in an Immiscible CO2 Field Project. *SPE Res Eng* ***01***(3) 112-118, SPE 14963. https://doi.org/10.2118/14963-PA.

Holt, T., Vassenden, T.1997. Reduced Gas - Water Segregation by Use of Foam. European Symposium on Improved Oil Recovery, 20-22 Oct, Hague, Netherlands. https://doi.org/10.3997/2214-4609.201406791.

Izadi, M., Kam, S. I. 2018. Bubble Population Balance Modeling to Predict Propagation Distance of CO2 Foams in Field-Scale Enhanced Oil Recovery Processes. SPE Trinidad and Tobago Energy Resources Conference, 25-26 June, Port of Spain, Trinidad and Tobago. https://doi.org/10.2118/191202-MS.

Jaimes, M. G., Quintero, Y. A., Contreras, G. Y. 2014. Drawdown Management: A Technical and Economic Alternative for Sand Control in Wells: A Colombian Field Application. Presented at the SPE Latin American and Caribbean Petroleum Engineering Conference, Maracaibo, Venezuela. 21-23 May, SPE 169376-MS. https://doi.org/10.2118/169376-MS.

Jenkins, M. K.1984. An Analytical Model for Water/Gas Miscible Displacements. Presented at the SPE Enhanced Oil Recovery Symposium, 15-18 April, Tulsa, Oklahoma. https://doi.org/10.2118/12632-MS

Jimenez, A. I., Radke, C. J. 1989. Dynamic stability of foam lamellae flowing through a periodically constricted pore. In Oil-Field Chemistry: Enhanced Recovery and Production Stimulation, Borchardt, J. K., Yen, T. F., ed(s), American Chemical Society, Washington, D.C., 460-479.

Johansen, S. A. 2016. An experimental study of foam flow in fractured systems of increasing size. Master Thesis. University of Bergen.

Jonas, T.M., Chou, S.I., Vasicek, S.I.1990. Evaluation of CO_2 foam field trial: Rangely Weber Sand Unit. SPE 20468-MS. Presented at the SPE Annual Technical Conference and Exhibition, 23-26 September, New Orleans, Louisiana, USA.

Kam, S. I., Rossen, W. R. 2003. A Model for Foam Generation in Homogeneous Media. *SPE J* 04 (8): 417- 425, SPE 87334. https://doi.org/10.2118/87334-PA.

Kam, S.I., 2008. Improved mechanistic foam simulation with foam catastrophe theory. *Colloids and Surfaces A: Physicochemical Engineering Aspects* 318(1-3), 62-77.

Kam, S.I. 2008. Improved Mechanistic Foam Simulation with Foam Catastrophe Theory. *Colloids Surf A: Physicochemical Engineering Aspects* (318) 1-3: 62-77(2008). https://doi.org/10.1016/j.colsurfa.2007.12.017.

Khatib, Z.I., Hirasaki, G.J., Falls, A.H. 1988. Effects of capillary pressure on coalescence and phase mobilities in foams flowing through porous media. *SPE Reservoir Engineering*, 919-926.

Klins, M. A.1984. Carbon Dioxide Flooding: Basic Mechanisms and Project Design. International Human Resources Development Corporation.

Kovscek, A. R. 1994. Foam displacement in porous media: experiment and mechanistic prediction by the population balance method. PhD Dissertation. University of California at Berkeley.

Kovscek, A. R., Tretheway, D. C., Persoff, P., Radke, C. J. 1995. Foam flow through a transparent rough-walled rock fracture. *Journal of Petroleum Science and Engineering* 2(13): 75-86. https://doi.org/10.1016/0920-4105(95)00005-3.

Kovscek, A.R., Bertin, H.J. 2002. Estimation of foam mobility in heterogeneous porous media. SPE 75181. Presented at the SPE/DOE Improved Oil Recovery Symposium, 13-17 April, Tulsa, Oklahoma, USA.

Kovscek, A.R., Patzek, T.W., Radke, C.J. 1995. A mechanistic population balance model for transient and steady-state foam flow in Boise sandstone. *Chemical Engineering Science* 50(23): 3783-3799.

Kovscek, A.R., Radke, C. J.1994. Foams: Fundamentals and Applications in the Petroleum Industry. In Fundamentals of Foam Transport in Porous Media. *Advance in Chemistry* 3(242): 115-163. Washington, DC: American Chemical Society. https://doi.org/10.1021/ba-1994-0242.

Kovscek, A.R., Patzek, T.W., Radke, C.J. 1997. Mechanistic Foam Flow Simulation in Heterogeneous and Multidimensional Porous Media. *SPE Journal* 2 (4). SPE-39102-PA.

Lacey, J.W., Draper, A.L., Binder, G.G.1958. Miscible Fluid Displacement in Porous Media. *Petrol Trans AIME* (213): 76-79.

Lawson, J. B., Reisberg, J. 1980. Alternate Slugs Of Gas And Dilute Surfactant For Mobility Control During Chemical Flooding. Presented at the SPE/DOE Enhanced Oil Recovery Symposium, 20-23 April, Tulsa, OK, USA. https://doi.org/10.2118/8839-MS.

Lee, S. and Kam, S.I. 2014. Three-Phase Fractional Flow Analysis for Foam-Assisted Non-Aqueous Phase Liquid (NAPL) Remediation. *Transport in Porous Media* 101 (3), 373-400.

Lee, S., Kam, S.I. 2013. Enhanced Oil Recovery by using CO_2 foams: fundamentals and field applications. *Gulf Professional Publishing, Elsevier*, 23-34.

Lee, W., Lee, S., Izadi, M., Kam, S.I. 2016. Dimensionality-Dependent Foam Rheological Properties: How to Go from Linear to Radial Geometry for Foam Modeling and Simulation. *SPE Journal* 21 (05), 1669 -1687.

Li, B., Hirasaki, G. J., Miller, C. A. 2006. Upscaling of Foam Mobility Control to Three Dimensions. SPE-99719-PA. Presented at SPE/DOE Symposium on Improved Oil Recovery, 22-26 April, Tulsa, Oklahoma, USA.

Liu, N., Ghorpade, S., Harris, L., Li, L., Grigg, R., Lee, R. 2010. The effect of Pressure and Temperature on Brine-CO_2 Relative Permeability and IFT at Reservoir Conditions. SPE 139029. Presented at SPE Eastern Regional Meeting, 13-15 October, Morgantown, West Virginia, USA.

Lotfollahi, M., Farajzadeh, R., Delshad, M., Varavei, A., Rossen, W.R. 2016. Comparison of implicit-texture and Population-balance foam models. *Journal of Natural Gas Science and Engineering*, 31, 184-197.

McCain, W.D., 1991. Reservoir-Fluid Property Correlations- State of the Art. *SPE Reservoir Engineering*, 266-272.

Mukherjee, J., Nguyen, Q.P., Scherlin, J., Vanderwal, P., Rozowski, P.2016. CO2 Foam Pilot in Salt Creek Field, Natrona County, WY: Phase III: Analysis of Pilot Performance. Presented at the SPE Improved Oil Recovery Conference, Tulsa, OK. 11-13 April, SPE 179635. https://doi.org/10.2118/179635-MS

Myers, T.J., Radke, C.J. 2000. Transient foam displacement in the presence of residual oil: Experiment and Simulation Using a Population-Balance Model. *Industrial & Engineering Chemistry Research* 39 (8), 2725-2741.

Ocampo, A., Restrepo, A., Cifuentes, H., Hester, J., Orozco, N., Gil, C., Gonzalez, C. 2013. Successful Foam EOR Pilot in a Mature Volatile Oil Reservoir under Miscible Gas Injection. Presented at the International Petroleum Technology Conference, Beijing, China.26-28 March, IPTC-16984-MS. https://doi.org/10.2523/IPTC-16984-MS.

Offeringa, J., van der Poel, C.1954. Displacement of Oil from Porous Media by Miscible Liquids. J Pet Technol (5) 12: 37-43. https://doi.org/10.2118/416-G.

Ortiz Maestre, D. 2017. Mechanistic Modeling of Nanoparticle-stabilized Supercritical CO_2 Foams and its Implication in Field-scale EOR Applications. Master's Thesis, Louisiana State University, Baton Rouge, Louisiana.

Osterloh, W.T., Jante, M.J. 1992. Effects of gas and liquid velocity on steady-state foam flow at high temperature. SPE 24179. Presented at the SPE/DOE Symposium on Enhanced Oil Recovery, 22-24 April, Tulsa, Oklahoma, USA.

Owete, O. S., Brigham, W. E. 1987. Flow Behavior of Foam: A Porous Micromodel Study. *SPE Reservoir Engineering* **03**(2): 315-323. SPE 11349-PA. https://doi.org/10.2118/11349-PA.

Pancharoen, M., Fernø, M. A., Kovscek, A. R. 2012. Modeling foam displacement in fractures. *Journal of Petroleum Science and Engineering* (100): 50-58. https://doi.org/10.1016/j.petrol.2012.11.018.

Patzek, T.W. 1988. Description of Foam Flow in Porous Media by the Population Balance Approach, in Surfactant-Based Mobility Control: Progress in Miscible Flood Enhanced Oil Recovery, Smith, D.H., ed(s), American Chemical Society, Washington, D.C., 326-341.

Polden, A. G. 2017. Foam generation and flow in fractures with different aperture. Master Thesis. University of Bergen.

Ransohoff, T. C., Radke, C. J. 1988. Mechanisms of Foam Generation in Glass-Bead Packs. *SPE Res Eng* 02 (3): 573-585. SPE 15441-PA. https://doi.org/10.2118/15441-PA.

Rodriguez, E. 2009. Evaluación Técnica de la Implementación de un Proceso de Inyección de Agua en el Campo Lisama Mediante Simulación Numérica de Yacimientos. Universidad Industrial de Santander (MSc), Colombia (Spanish).

Roof, J. G. 1970. Snap-Off of Oil Droplets in Water-Wet Pores. *SPE J* 01 (10): 85-90. SPE 2504. https://doi.org/10.2118/2504-PA.

Rossen, W. R. 1999. Foam Generation at Layer Boundaries in Porous Media. *SPE J* 04 (4): 409-412. SPE 59395-PA. https://doi.org/10.2118/59395-PA.

Rossen, W. R. 2000. Snap-off in Constricted Tubes and Porous Media. *Colloids Surfaces A: Physicochem Eng. Aspects* (166) 101-107.

Rossen, W. R., Gauglitz, P. A. 1990. Percolation theory of creation and mobilization of foams in porous media. *AICHE J* 8 (36): 1176-1188. https://doi.org/10.1002/aic.690360807.

Rossen, W. R., Shen, C. 2007. Gravity Segregation in Gas-Injection IOR. EUROPEC/EAGE Conference and Exhibition, 11-14 June, London, UK. https://doi.org/10.2118/107262-MS.

Rossen, W.R. 1996. Foams in enhanced oil recovery. In Foams: Theory Measurements and Applications. *R.K. Prud'homme and S. Khan (eds.).* New York: Marcel Dekker.

Rossen, W.R., Ocampo, A., Restrepo, A., Cifuentes, H.D., Marin, J. 2017. Long-time Diversion in Surfactant-Alternating-Gas Foam Enhanced Oil Recovery from a Field Test. *SPE Res Eval & Eng* 01 (20): 1-7, SPE 170809-PA. https://doi.org/10.2118/170809-PA.

Rossen, W.R., van Duijn, C.J. 2004. Gravity Segregation in Steady-State Horizontal Flow in Homogeneous Reservoirs. *J Petr Sci Eng* 1-2 (43): 99-111. https://doi.org/10.1016/j.petrol.2004.01.004.

Sanchez, N.L.1999. Management of Water Alternating Gas (WAG) Injection Projects. Presented at the SPE Latin American and Caribbean Petroleum Engineering Conference, Caracas, Venezuela, 21-23 April, SPE 53714. https://doi.org/10.2118/53714-MS.

Sandoval, J. R., Sandoval, J., Soto, C. P., Perez, H. H.,Trujillo Portillo, M. L., Cardenas, F. A., Castro, R. H., Gomez Ramirez, V., Rodriguez, E. 2009. New Approach to Integrate Reservoir and Geological Information in Complex Fluvial-Stratigraphic Environments to Determine Potential Areas for Water Injection Processes. Presented at the SPE Latin American and Caribbean Petroleum Engineering Conference, Cartagena de Indias, Colombia. 31 May – 3 June, SPE 122108-MS. https://doi.org/10.2118/122108-MS.

Shi, J.-X., Rossen, W. R.1998. Simulation and Dimensional Analysis of Foam Processes in Porous Media. *SPE Res Eval & Eng* 02(1):148-154. https://doi.org/10.2118/35166-PA.

Stone, H. L.1983. Vertical Conformance in an Alternating Water-miscible Gas Flood. Presented at the SPE Annual Fall Technical Conference and Exhibition, New Orleans, LA, 26-29 September, SPE 11130. https://doi.org/10.2118/11130-MS.

Tanzil, D. 2001. Foam Generation and Propagation in Heterogeneous Porous Media. PhD Dissertation, Rice University.

van Poollen, H. K.1980. Fundamentals of Enhanced Oil Recovery. PenWell Publishing Company, Tulsa, Oklahoma.

Vasshus, S. S. 2016. Experimental study of foam generation and flow in carbonate fracture systems. Master Thesis. University of Bergen.

Yin, G. 2007. Experimental Study of CO_2 Foam Flooding in Berea Sandstone at Reservoir Conditions. Master Thesis, New Mexico Institute of Mining and Technology, Socorro, NM (March 2007).

Yu, G., Rossen, W.R., Vincent-Bonnieu, S. 2018. Coreflood Study of Effect of Surfactant Concentration on Foam Generation in Porous Media. Ind. Eng. Chem. Res. In press.

VITA

Mohammad Izadi was born in 1983 in Isfahan, Iran. He pursued his undergraduate degree in petroleum engineering at the Petroleum University of Technology. Then, he moved to the United States to continue his education and he received a master's degree in petroleum engineering from University of Louisiana at Lafayette. After graduation, he worked as a consultant reservoir engineer in Texas and California. His passion for research convinced him to return to Louisiana State University for doctoral degree. Upon PhD graduation, he intends to join an organization where he could apply his expertise and knowledge and to learn new skills.